Dissertation

submitted to the

Combined Faculty of Mathematics, Engineering and Natural Sciences

of Heidelberg University, Germany

for the degree of

Doctor of Natural Sciences

Put forward by

Benjamin Brauneis

born in: Heidelberg, Germany

Oral examination: February 5th, 2025

Measuring smallest magnetic field gradients using hyperpolarized ^{129}Xenon

Referees:

Prof. Dr. Ulrich Schmidt

Prof. Dr. Selim Jochim

והוא מחלל מפשענו מדכא מעונתינו
מוסר שלומנו עליו ובחברתו נרפא-לנו
ישעיהו נג,ה

Doch er war durchbohrt um unserer Vergehen willen, zerschlagen
um unserer Sünden willen. Die Strafe lag auf ihm zu unserem
Frieden, und durch seine Striemen ist uns Heilung geworden.
Jesaja 53,5

Kurzzusammenfassung

Die Erklärung der beobachteten Baryonen-Asymmetrie in unserem Universum ist eines der ungelösten Probleme der Physik. Dieses mit dem etablierten Standardmodell zu lösen, ist aufgrund fehlender Quellen von CP-Verletzung nicht möglich. Daher wird ein allgemeineres Modell benötigt, in welches das Standardmodell eingebettet ist. Mit dem ^{3}He/^{129}Xe-Comagnetometer ist es möglich, das permanente elektrische Dipolmoment (EDM) von ^{129}Xe-Atomen zu messen, das ein experimentell zugängliches Signal für zusätzliche Quellen von CP-Verletzung liefern könnte. Um solche Messungen durchführen zu können, werden homogene Magnetfelder mit Feldgradienten im Bereich von pT/cm benötigt. Daher wurde im Jahr 2021 am Physikalischen Institut in Heidelberg ein magnetisch abgeschirmter Raum (MSR) errichtet. Im Rahmen dieser Arbeit konnte dieser neue MSR charakterisiert und eine neuartige Entmagnetisierungsroutine motiviert und getestet werden, die zu einem gemessenen Restmagnetfeld von (1,2 ± 0,2) nT im Zentrum führt. Außerdem wurde ein bestehender Aufbau zur Erzeugung von hyperpolarisiertem (HP) ^{129}Xe in Betrieb genommen und optimiert. Eine dezidierte Kalibrierung des NMR-Signals von HP Xenon ergab eine absolute Polarisation von bis zu (37 ± 3) % im Flussmodus und (18,8 ± 0,5) % nach der Akkumulation, die reproduzierbar erreicht werden konnte. HP Xenon-Gas konnte erfolgreich in den MSR transferiert werden, um erste systematische Tests durchzuführen. Es konnten Speicherzeiten von bis zu $T_1 = (8521 \pm 254)$ s und eine kohärente Präzessionszeit von $T_2^* = (4137 \pm 17)$ s erreicht werden. Diese Eigenschaften ermöglichten präzise Messungen von Magnetfeldgradienten innerhalb des MSR mit einer Genauigkeit von unter einem pT/cm. Somit liefert diese Arbeit eine wichtige Grundlage für zukünftige ^{129}Xe-EDM Messungen.

Abstract

Explaining the observed baryon asymmetry in our universe is one of the unsolved problems in physics. Solving it with the well-known Standard Model is not possible, due to missing sources of CP violation. Therefore, a more general model is needed in which the Standard Model is embedded. Using the ^{3}He/^{129}Xe comagnetometer, it is possible to measure the permanent electric dipole moment (EDM) of ^{129}Xe atoms which may provide an experimentally accessible signal for additional sources of CP violation. To be able to perform such measurements, homogeneous magnetic fields with gradients at the level of pT/cm are required. Therefore, an MSR (magnetically shielded room) was constructed in the year 2021 at the Physikalisches Institut in Heidelberg. In the scope of this thesis, this new MSR was characterized and a novel degaussing routine could be motivated and tested yielding to a measured residual magnetic field of (1.2 ± 0.2) nT at the center. Furthermore, an existing setup producing HP (hyperpolarized) ^{129}Xe was commissioned and optimized. A dedicated calibration of the NMR signal of HP xenon revealed an absolute polarization of up to (37 ± 3) % in flow mode and (18.8 ± 0.5) % after accumulation which could be reproducibly achieved. HP xenon gas could be successfully transferred into the MSR in order to perform first systematic tests. Storage times of up to $T_1 = (8521 \pm 254)$ s and a coherent precession time of $T_2^* = (4137 \pm 17)$ s could be reached. These characteristics allowed for precise measurements of magnetic field gradients within the MSR with a sensitivity below 1 pT/cm. Thus, this work laid an important foundation for future ^{129}Xe-EDM measurements.

Contents

Chapter 1

Introduction to the Helium-Xenon Experiment

One of the unsolved problems in physics is the question why there is more matter than antimatter in our universe. The matter which can be observed and everything is made of, consists mainly of baryons like the proton and the neutron. In order to quantify the problem above, the so-called baryon asymmetry is defined as

$$\eta = \frac{n_b - n_{\bar{b}}}{n_\gamma} \tag{1.0.1}$$

where n_i describes the densities of baryons, antibaryons and photons. According to Cosmology (Big-Bang Theory) in combination with the Standard Model, it is assumed that baryons and antibaryons were formed in a symmetric way such that $\eta = 0$. But nowadays it is observed that matter dominates over the antimatter in the universe. By analyzing the Cosmic Microwave Background (CMB) radiation, η can be estimated to $(6.1 \pm 0.3) \times 10^{-10}$ [1]. This transition from baryon symmetry to baryon asymmetry was first explained by Andrei Sakharov by formulating three conditions [2] which have to be fulfilled:

- violation of baryon number
- violation of C- and CP-symmetry
- the universe is out of thermal equilibrium

With these conditions, it is possible to estimate η by the use of the Standard Model. It is the most successful model so far which describes three of the four fundamental interactions, namely the strong, electromagnetic and the weak interaction. In context of this thesis, especially the violation of CP-symmetry is of big interest. Within the Standard Model, CP violation (shortly CPV) is implemented as a complex phase in the CKM-Matrix for the weak interaction involving quark transitions. Furthermore, the strong interaction contains one parameter which would also allow for CPV. Experimentally, however, this parameter was determined to be consistent with zero to high level of precision. Therefore, this observation is often called the strong CP-Problem. The CPV within the Standard Model is far too small in order to explain the baryon asymmetry observed in our universe using the Sacharov conditions. Calculations of η using the Standard Model are yielding to values which are many orders of magnitudes smaller than value observed [3]. For this reason, huge efforts are made identifying missing sources of CPV which are not contained in the Standard Model.

1.1 Electric dipole moments of fundamental particles

One approach to observe CPV is to measure the permanent electric dipole moment (EDM) $\vec{d}$ of fundamental particles. It is defined by a volume integral:

$$\vec{d} = \int_V \vec{x}\rho(\vec{x})d^3x \tag{1.1.1}$$

where $\rho(\vec{x})$ is the charge distribution of that particle. When the particle is neutral but has a non-vanishing EDM, this can be described by a spatial separation of opposite charges. In the same way as the EDM, the magnetic moment $\vec{\mu}$ can be defined:

$$\vec{\mu} = \int_V \vec{x} \times \vec{j}(\vec{x})d^3x \quad . \tag{1.1.2}$$

Here, $\vec{j}(\vec{x})$ is the current-density distribution of the particle. The orientation of the magnetic moment of a particle is given by the direction of its spin $\vec{S}$. Both quantities are related by the gyromagnetic ratio γ:

$$\vec{\mu} = \gamma \cdot \vec{S} \quad . \tag{1.1.3}$$

For such a particle, the spin is the only preferred direction. Thus, it is assumed that the EDM is oriented in the same direction like the spin. Otherwise, according to Pauli's principle, additional quantum numbers would exist labeling additional eigenstates of the particle which have never been observed.

$$\vec{d} = \frac{d}{|S|}\vec{S} \tag{1.1.4}$$

As shown in Fig. (1.1.1), the existence of a permanent EDM would be T violating. Assuming that CPT symmetry is preserved, an EDM must also be CP violating. Therefore, it is an excellent signal for CPV which is experimentally accessible.

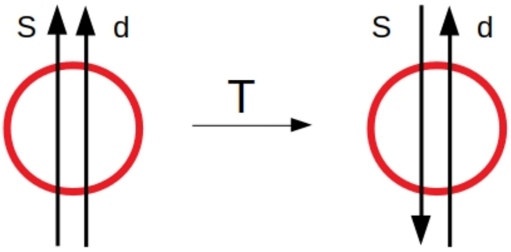

Figure 1.1.1: Effect of a T transformation on EDM and spin. By CPT conservation, a T violation implies a CP violation. Source: [4].

1.2 EDM in SM and BSM

In this section, a short overview of the theoretical setup used to describe EDM measurements will be provided. In the Standard Model, only two terms are relevant for this discussion. As argued in the section above, these terms need to violate the CP symmetry. This is the case for the weak quark mixing, when an up-type quark is coupled to a down-type quark via the CKM matrix:

$$\mathcal{L}_{CKM} = -\frac{ig_2}{\sqrt{2}}\, V^{pq}_{CKM}\, \bar{U}^p_L \not{W}^+ D^q_L + h.c. \tag{1.2.1}$$

V^{pq}_{CKM} is the CKM matrix containing a complex phase which is responsible for CPV. $\not{W}^\pm = \gamma^\mu\ W^\pm_\mu$ are the gauge fields for the flavour changing charged current interactions. Using this Lagrangian, EDMs of several particles can be predicted. As an example, in Fig. (1.2.1), the lowest order Feynman diagrams contributing to the electron EDM (eEDM) are shown. Due to their high loop order, they are extremely suppressed yielding to very small values for the eEDM of order 10^{-44} ecm [5].

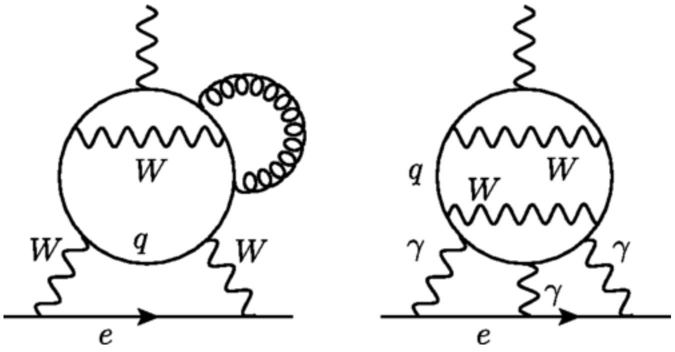

Figure 1.2.1: Lowest order CKM contributions to electron EDMs. Source: [5].

Same considerations can also be done for other particles. This includes neutrons, nuclei, atoms and molecules. The complexity of the particle's structure also scales with the complexity of their theoretical description. This may include hadronic corrections and/or atomic- and molecular-physics considerations. However, it can be summarized, that EDM predictions from the Standard Model for any fundamental particle are stating values which are extremely small and far of reach for any experiment so far.

However, the weak interaction is not the only potential source of CPV within the Standard Model. For the strong interaction, the following CP violating term in the Standard-Model Lagrangian would be allowed:

$$\mathcal{L}_{\bar{\theta}} = -\frac{g_3^2}{16\pi^2}\bar{\theta}\ \mathrm{Tr}(G^{\mu\nu}\tilde{G}_{\mu\nu}) \tag{1.2.2}$$

where $G^{\mu\nu}$ is the gluon field strength tensor and $\tilde{G}_{\mu\nu} = 1/2\ \varepsilon_{\mu\nu\alpha\beta}G^{\alpha\beta}$ is its dual. g_3 is the coupling constant for strong interaction and $\bar{\theta}$ is a dimensionless free parameter. This parameter directly contributes to an EDM of the neutron (nEDM) [6]:

$$d_n = 5.2 \times 10^{-16}\ \bar{\theta}\ \text{ecm} \quad . \tag{1.2.3}$$

Experimental searches of the nEDM, however, yielded to tight limits of $\bar{\theta}$. Already in 1957 an upper bound of the nEDM of 5×10^{-20} ecm was published by Smith, Purcell and Ramsey [7]. Over the years, this limit was improved by several orders of magnitude. The current limit for the nEDM was measured by the PSI collaboration [8] yielding:

$$|d_n| < 1.8 \times 10^{-26}\ \text{ecm (90\% C.L.)}. \tag{1.2.4}$$

With such a low value for the nEDM, $\bar{\theta}$ can be restricted to orders of 10^{-10}. At this point, it seems very unnatural that a free parameter should have such a small value. This observation is often called strong CP problem. The most famous approach to resolve this issue is to introduce an additional U(1) symmetry, the so called Peccei-Quinn symmetry [9]. The consequence is that the $\bar{\theta}$ term is exactly zero and a new pseudoscalar particle, known as axion, is introduced. Experimentally, the existence of axions could never be verified or excluded.

Up to now, the discussion so far may suggest that the Standard Model is not fully complete due to the missing CPV. It is believed to be a low energy limit of a more general theory. A lot of effort is made to search for new theories resolving all issues and still remaining consistent with the Standard Model. Examples are supersymmetric theories, string theory, multi-higgs theory, etc. All these theories have in common, that they contain new fields representing particles which can only be produced at high energies, far of reach for present colliders. The search for permanent EDMs is one example of how such so-called "new-physics" models can be made experimentally accessible.

The framework which is used in context of EDM measurements is called Effective Field Theory. Starting with an arbitrary theory $\mathcal{L}_{\text{new}}$ which generalizes the Standard Model at high energies, an energy scale Λ is chosen such that for energies $E \ll \Lambda$ the Standard Model is still valid and for $E \gg \Lambda$ the Standard Model may not be valid anymore and new degrees of freedom, i.e. new fields ϕ_k occur. These fields can be also divided into high-energy and low-energy parts: $\phi = \phi_L + \phi_H$. In Fourier space, ϕ_L covers the region where $\omega < \Lambda$ and ϕ_H the region where $\omega > \Lambda$. By removing the contributions of ϕ_H, the Lagrangian $\mathcal{L}_{\text{new}}$ can be written as a series with infinitely many terms:

$$\mathcal{L}_{\text{new}}^{\text{eff}} = \sum_{d>4} \sum_{i} \frac{\alpha_i^{(d)}}{\Lambda^{d-4}} \hat{O}_i^{(d)} \quad . \tag{1.2.5}$$

This step is often referred to as "integrating out" the high-energy fields. In $\mathcal{L}_{\text{new}}^{\text{eff}}$, the individual terms have the same structure: $\hat{O}_i^{(d)}$ is a new effective operator with dimension d in units of energy. These operators contain only the Standard-Model fields, but now combinations are possible which are forbidden within the Standard Model. $\alpha_i^{(d)}$ is a dimensionless parameter which is called Wilson coefficient. Due to the fact that the Lagrangian must have dimension 4, all terms are normalized by the cut-off scale Λ. The summation is arranged such that the dimensions are counted and various operators with same dimension are grouped together. Trying to relate the Wilson coefficients of these terms to experimental measurements, the terms with low d have the largest contribution. Therefore, higher dimensions are often ignored.

In order to describe for example a permanent EDM of a particle, Effective Field Theory can be used the other way round. It is left unspecified which theory is believed to be the correct generalization of the Standard Model. One can start directly with an effective Lagrangian asking which terms may occur with a certain dimension. In general, such terms must be Lorentz invariant and obey the Standard Model gauge symmetry $\mathrm{SU}(3)_C \times \mathrm{SU}(2)_L \times \mathrm{U}(1)_Y$. In the special case of EDM measurements, only terms which violate CP symmetry are relevant. Due to this criteria, 12 effective operators with dimension 6 can be found. These terms are combined with the known Standard Model CPV contributions:

$$\mathcal{L}^{eff}_{CVP} = \mathcal{L}_{CKM} + \mathcal{L}_{\bar{\theta}} + \mathcal{L}_{BSM} \quad . \tag{1.2.6}$$

The main advantage of this approach is its model independence. It provides a framework which allows to compare several experimental results of EDM measurements performed with different particles. In Tab. (1.2.1) all relevant Wilson coefficients are listed. Their special meaning and further information about their operators can be found in [10].

There are several classes of EDM measurements, starting with fundamental particles such as electrons or muons, hadrons like neutrons and protons and charged nuclei or whole atoms and molecules that are examined. The EDM of different systems is sensitive to different combinations of Wilson coefficients. By complementary measurements, it is possible to extract values, or at least upper bounds, for the Wilson coefficients. Comparing these to the Wilson coefficients originating from a specific generalizing theory, it can be concluded whether it is consistent with EDM measurements or not.

Wilson coefficient	Operator(dimension)	Number	Systems
$\bar{\theta}$	theta term (4)	1	diamagnetic atoms & hadronic
δ_e	electron EDM (6)	1	paramagnetic atoms & molecules
Im $C^{(1,3)}_{lequ}$, Im C_{leqd}	semi-leptonic (6)	3	
δ_q	quark EDM (6)	2	diamagnetic atoms & hadronic
$\tilde{\delta}_q$	quark chromo EDM (6)	2	
$C_{\tilde{G}}$	three-gluon (6)	1	
Im $C^{(1,8)}_{quqd}$	four-quark (6)	2	
Im $C_{\varphi qd}$	induced four-quark (6)	2	
Total		13	

Table 1.2.1: Table of all relevant Wilson coefficients describing EDM measurements. Table extracted from [10]

In reality, it is a complex task to relate the Wilson coefficients to experimental results. It turns out, that a single (precise) measurement cannot constrain certain coefficients very stringently. With a global fit of several different experimental results however, the uncertainties can be substantially reduced [11]. Therefore, it is important to increase the sensitivities of many experiments simultaneously.

1.3 Experimental efforts to measure the ^{129}Xe EDM

In all experiments performing EDM measurements, it is used that an EDM in an electric field yields to an additional splitting of the energy levels and therefore to a shift in the transition frequency. Starting point is the accurate measurement of the precession frequency of a certain species of particles within a magnetic holding field. When applying strong electric fields parallel or antiparallel to the magnetic field, it is observed how much the frequency changes. If a measurable EDM exists, the precession frequency will be correlated with the applied electric field. Up to now, no EDM could be experimentally measured this way. Therefore, the combined error (systematic and statistical error) can be used to extract an upper bound for an EDM measurement which is consistent with zero.

The most recent measurements of the ^{129}Xe-EDM were independently performed in 2019 by two working groups in Jülich [12] and Munich [13]. In both experiments a similar upper bound of 1.5×10^{-27} ecm could be found. In this experiment, the spin precession of HP (hyperpolarized) noble gases which are ^{3}He and ^{129}Xe were measured. This gas mixture is confined within a spherical glass cell which is located within a homogeneous magnetic holding field B_0. In order to achieve the desired homogeneity, the experiment has to be performed within an MSR (magnetically shielded room). When a spin is oriented perpendicular to B_0, a precession frequency

$$\omega_i = \gamma_i B_0 \tag{1.3.1}$$

is observed. γ_{i} is the gyromagnetic ratio and depends on the nucleus which carries the spin. The goal of this experiment is to measure ω_{Xe} to highest precision by maximizing the measuring time which depends on the transverse relaxation time T_2^*. As it will be discussed in the next chapters, relaxation times of several hours are achievable. During that time, drifts of B_0 and therefore of ω_{i} cannot be prevented. Experimentally, B_0 can be kept stable to a level of 10^{-6}. This will set a limit to the maximum precision that can be reached for frequency measurements. To overcome this limit, the trick of comagnetometry is used. As mentioned above, the spin precession of two noble gases is measured in one sample cell. Due to different gyromagnetic ratios of helium and xenon, two different precession frequencies are measured. By dividing the two frequencies by each other, the dependency of the magnetic field is canceled out and the magnetic field drift does not affect the precision of that quantity. This is used when the weighted frequency difference and the weighted phase difference are defined:

$$\Delta\omega = \omega_{\mathrm{Xe}} - \frac{\gamma_{\mathrm{Xe}}}{\gamma_{\mathrm{He}}}\omega_{\mathrm{He}} \tag{1.3.2}$$

$$\Delta\Phi = \Phi_{\mathrm{Xe}} - \frac{\gamma_{\mathrm{Xe}}}{\gamma_{\mathrm{He}}}\Phi_{\mathrm{He}} \quad . \tag{1.3.3}$$

Assuming only a magnetic coupling to the spin, $\Delta\omega$ is always zero. Any deviation from zero would imply a non-magnetic interaction with the spins. Applying an additional electric field which couples to the EDM of a xenon atom, will yield to a shift in energy and therefore also in ω_{Xe}. The weighted frequency difference changes as

$$\Delta\omega = \pm\frac{2}{\hbar} d_{\mathrm{Xe}} |E_z| \tag{1.3.4}$$

where the plus sign applies when $\vec{B}$ and $\vec{E}$ are parallel and the minus sign is valid for the antiparallel case. If a correlation between $\Delta\omega$ and the electric field $\vec{E}$ was measured, this would be a direct sign for a non-vanishing permanent ^{129}Xe-EDM. Of course, many other systematic effects may occur which have to be excluded. A nice overview is given in [12].

A few words should be said about a potential EDM of ^{3}He. The quantity $\Delta\omega$ is sensitive to the ^{129}Xe-EDM only. The reason for that is Schiff's theorem [14]. It states that an EDM of the nucleus of an atom is completely shielded by its valence electrons when the following assumptions are fulfilled: The composite system consists of point-like particles which are non-relativistic. Both conditions are perfectly met for the ^{3}He atom. For this reason, the EDM of helium is not accessible in this experiment. For ^{129}Xe, however, the statements above are not valid. As a consequence, the shielding is suppressed by orders of magnitudes following a Z^2 dependency [15] where Z represents the atomic number. For this reason, it can be justified that ^{3}He is used as a comagnetometer and ^{129}Xe as the actual probe.

The signal of interest which is a sum over all spins is measured by a SQUID magnetometer (Superconducting QUantum Interference Device). It is by now the most accurate magnetic field sensor with the largest resolution which relies, as the name may suggest, on quantum effects. The intrinsic noise level of 0.7 $\mathrm{fT}/\sqrt{\mathrm{Hz}}$ allows for precise magnetic-field measurements of the precessing spins. In chapter 2, some basic concepts regarding its working principle will be discussed. In order to achieve the best resolution for $\Delta\omega$, the time T during the precession is measured coherently should be maximized. T depends on the T_2^* relaxation time which will be introduced within the next chapter. The statistical uncertainty for a frequency measurement can be estimated by the Cramer-Rao Lower Bound [16]:

$$\sigma_\omega = \sqrt{12} \cdot \frac{\rho}{A} \cdot T^{-\frac{3}{2}} \cdot \sqrt{C(T, T_2^*)} \quad . \tag{1.3.5}$$

A is the signal amplitude and depends on the amount of spins and the polarization. ρ is the noise level of the SQUID sensor and is obtained by integrating the power spectral density over the relevant bandwidth. Both quantities, A and ρ are determining the SNR (signal-to-noise ratio) measured by the SQUID which enters linearly in σ_ω. The factor $C(T, T_2^*)$ is a correction term for an exponentially damped signal. It changes only with $r = \frac{T}{T_2^*}$. When the signal is decayed ($T_2^* \ll T$) then no information but additional noise is acquired. Therefore, there must exist an optimal ratio r which is $r \approx 3$ [17]. From the equation above, it can be deduced for fixed r, when T_2^* is slightly increased, σ_ω may change significantly. Applying this equation to the EDM of xenon, an additional factor occurs which is the electric field E_z. Increasing E_z will also improve the statistical uncertainty of the final EDM d_{Xe}.

1.4 Outline of this thesis

The idea of the Helium-Xenon Experiment, as presented above, is very clear and straight forward. The implementation of these ideas, however, certainly is not. Due to the complexity of all individual components, the installation of the whole Helium-Xenon Experiment, or even measurements of the ^{129}Xe EDM during this thesis within the last three years were far of reach. Therefore, this thesis should be regarded as a starting point for future works.

After this short introduction to the Helium-Xenon Experiment, all important theoretical concepts are introduced in the next chapter. During the beginning of this thesis (fall, 2021) a new MSR was constructed in Heidelberg University. In chapter 3, the new MSR is characterized and a new degaussing routine is motivated and tested. In chapter 4, the setup is described which was commissioned and adapted to reproducibly hyperpolarize ^{129}Xe. Subsequently, it is shown, how the NMR signal for the obtained xenon polarization can be calibrated using the well-known value of thermally polarized water. As highlight and final conclusion of this thesis, first measurements of HP ^{129}Xe within the MSR are presented.

Chapter 2

Theory of spin precession

This chapter provides an overview of theoretical concepts used in this thesis. Firstly, the macroscopic magnetization is defined and the Bloch equations are introduced. As the resolution of the Helium-Xenon Experiment is limited by T_2^*, the mechanisms of relaxation are regarded in full detail. Then, it is explained how to manipulate spins by resonant Pi/2-flips and non-adiabatic flips. After that, the process of hyperpolarization of ^{129}Xe is described and will be roughly sketched for ^{3}He. Finally, the measurement of HP gases using a SQUID system is covered.

2.1 Bloch equations

Starting with a nuclear spin $\vec{I}$ of an atom, the (nuclear) magnetic moment $\vec{\mu}$ is defined by

$$\vec{\mu} = g\mu_N\vec{I} = \gamma\hbar\vec{I} \tag{2.1.1}$$

where g is the so-called nuclear g-factor and $\mu_N = \frac{e\hbar}{2m_p}$. m_p is the proton mass, e the elementary charge and γ the gyromagnetic ratio. Both, γ and g depend on the atom which is considered. For this thesis, the gyromagnetic ratios of ^{129}Xe, ^{3}He and the proton will become relevant. They have in common, that their nuclear spin is one half. Therefore, it is assumed, that $I = 1/2$. The values of γ are given below [18], [19], [20]. It is important to distinguish between the units MHz/T and $T^{-1}s^{-1}$. When calculating with the second units, the values given below have to be multiplied by 2π. The prime for γ_p' indicates that the value is given for shielded protons in a water molecule.

$$\gamma_{^3\mathrm{He}}/(2\pi) = -32.434\ 100\ 033(28)\ \mathrm{MHz/T} \tag{2.1.2}$$

$$\gamma_{^{129}\mathrm{Xe}}/(2\pi) = -11.7767338(3)\ \mathrm{MHz/T} \tag{2.1.3}$$

$$\gamma_p'/(2\pi) = 42.576\ 385\ 43(17)\ \mathrm{MHz/T} \tag{2.1.4}$$

Instead of examining a single spin, in the scope of the Helium-Xenon Experiment, more than 10^{19} spins are measured. The macroscopic quantity of interest is the magnetization which is defined by the sum over all spins:

$$\vec{M} = \frac{1}{V}\sum_i \vec{\mu}_i \quad . \tag{2.1.5}$$

When all spins are randomly oriented, the magnetization is very small and not measurable. This changes when an external magnetic field $\vec{B}_0$ is present. The magnetic moments are coupled to $\vec{B}_0$ by

$$H = -\vec{\mu} \cdot \vec{B}_0 = -\gamma \hbar \vec{I} \cdot \vec{B}_0 = -\frac{\gamma \hbar}{2} \vec{\sigma} \cdot \vec{B}_0 \tag{2.1.6}$$

yielding to an energy splitting where spins are parallel and antiparallel to $\vec{B}_0$. Here, the spin vector $\vec{I}$ is defined by Pauli's matrices $\vec{\sigma} = (\sigma_x, \sigma_y, \sigma_z)^T$ which are given by

$$\sigma_x = \begin{pmatrix} 0 & 1 \\ 1 & 0 \end{pmatrix}, \sigma_y = \begin{pmatrix} 0 & -i \\ i & 0 \end{pmatrix}, \sigma_z = \begin{pmatrix} 1 & 0 \\ 0 & -1 \end{pmatrix} \quad . \tag{2.1.7}$$

The energy difference between these states is given by

$$\Delta E = E_{+1/2} - E_{-1/2} = -\hbar \gamma B_0 \quad . \tag{2.1.8}$$

The population of these states is governed by thermal excitations and can be therefore described by Boltzmann's distribution:

$$\frac{N_-}{N_+} = e^{-\frac{\Delta E}{kT}} \quad . \tag{2.1.9}$$

In order to quantify the magnetization in a different way, the polarization can be defined as

$$P = \frac{N_+ - N_-}{N_+ + N_-} = \frac{e^{\frac{\Delta E}{kT}} - 1}{e^{\frac{\Delta E}{kT}} + 1} = \tanh\left(\frac{\Delta E}{2kT}\right) = \tanh\left(-\frac{\hbar \gamma B_0}{2kT}\right) \quad . \tag{2.1.10}$$

A typical value for thermal polarizations for ^{129}Xe spins at room temperature and a magnetic field of 1 Tesla is around 10^{-6}. This is very low compared to polarizations achieved by optical pumping methods which are $> 10^{-1}$. However, the small signal of thermal polarization can be used in magnetic resonance imaging applications. The overall magnetization is given by:

$$\vec{M} = \frac{1}{V} \cdot N \cdot P \cdot \vec{\mu} \quad . \tag{2.1.11}$$

The time evolution of the magnetization was first described by Felix Bloch in 1946 [21]. The well-known Bloch equations are:

$$\frac{d}{dt}\vec{M}(t) = \gamma \vec{M}(t) \times \vec{B}(t) + \begin{pmatrix} -M_x/T_2^* \\ -M_y/T_2^* \\ (M_{z,th-M_z})/T_1 \end{pmatrix} \quad . \tag{2.1.12}$$

The consequence of this equation is that the magnetization will always reach an equilibrium state when the magnetic field $\vec{B}$ is constant. This state is the thermal polarization parallel to $\vec{B}$. If the magnetization starts perpendicular to $\vec{B}$, it will relax back into parallel orientation. The first term on the right-hand side results in a precession behavior of the magnetization, whereas the second term describes the relaxation. The phenomenological time constants T_1 and T_2^* are called spin-lattice relaxation time and spin-spin relaxation time, respectively. The relaxation times are of significant importance for the Helium-Xenon Experiment as they limit the overall measuring time and therefore the resolution of the final result. So, it is crucial to understand the processes affecting the spin relaxation in order to optimize them. But before the relaxation mechanisms are presented, it should be explained how the magnetization can be manipulated such that precession can be observed.

2.2 Spin-flips

Starting in thermal equilibrium, the magnetization is oriented in parallel to the magnetic holding field $\vec{B}$. The signal which is measured in the Helium-Xenon Experiment - and in general for all NMR applications - is the spin precession. Therefore, the magnetization needs to be flipped into the transversal plane. In the scope of this thesis, two methods were used which should be presented in the following.

The first way to achieve a spin-flip is called non-adiabatic flip. The basic idea is to slowly rotate the magnetic holding field by 90° such that the spins can follow adiabatically. This is the case when the rotation speed Ω_r of the guiding field is much smaller than the Larmor frequency ω_L. At this point, both, $\vec{M}$ and $\vec{B}$ are rotated by 90°. Now $\vec{B}$ is quickly rotated back into the original orientation. In Fig. (2.2.1), the sequence used is shown in step 2 and 3. In step 2, the field is quickly ramped down to zero and thereafter, quickly ramped up again in z direction. The spins are too slow to follow. When steps 2 and 3 are performed fast enough the spins are still pointing in x direction while the magnetic field shows in z direction. After this cycle, the spins start to precess and the measurement can start. In principle, other flip angles are also possible to achieve which will be used within this work. It is important to always ramp $\vec{B}$ down to zero. Otherwise, when $\vec{B}$ is just rotated backwards by reverting step 1, it is not clear whether the angle still remains 90°.

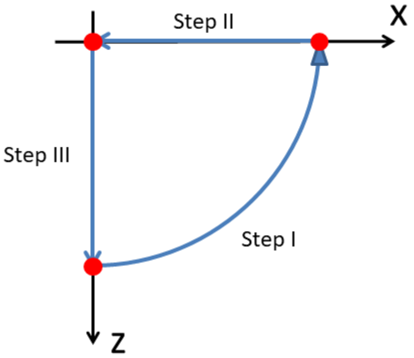

Figure 2.2.1: Sequence to flip the spins non-adiabatically by 90°.

Another way to achieve a spin-flip is commonly used in NMR. The spins are again in thermal equilibrium, oriented in parallel to the magnetic holding field $\vec{B}$. By applying a circularly polarized magnetic field in transversal direction for a time duration Δt, the orientation of the spins can also be changed. In this case, the magnetic field can be represented as

$$\vec{B}(t) = \begin{pmatrix} B_1 \cos(\omega t - \phi) \\ B_1 \sin(\omega t - \phi) \\ B_0 \end{pmatrix} \quad . \tag{2.2.1}$$

If $\omega \approx \omega_L$, the flip angle α will depend on the amplitude B_1 and Δt:

$$\alpha = \gamma B_1 \Delta t \quad . \tag{2.2.2}$$

To achieve a specific angle, both, B_1 and Δt can be adjusted. In the following, the general case for an arbitrary ω should be regarded. This can be calculated by plugging an arbitrary magnetic field $\vec{B}(t)$ into the Hamiltonian (2.1.6). The strategy is to solve the Schrödinger equation for the time evolution operator $U(t)$:

$$i\hbar \partial_t U(t) = HU(t) \tag{2.2.3}$$

with the initial condition U(t=0)=1. This calculation was performed in [22] and therefore the solution is just presented as:

$$U(t) = \begin{pmatrix} \left(\cos\left(\frac{\omega_2}{2}t\right) - ig\sin\left(\frac{\omega_2}{2}t\right)\right)\exp\left(-i\frac{\omega}{2}t\right) & -ic\sin\left(\frac{\omega_2}{2}t\right)\exp\left(-i(\frac{\omega}{2}t - \phi)\right) \\ -ic\sin\left(\frac{\omega_2}{2}t\right)\exp\left(i(\frac{\omega}{2} - \phi)\right) & \left(\cos\left(\frac{\omega_2}{2}t\right) + ig\sin\left(\frac{\omega_2}{2}t\right)\right)\exp\left(i\frac{\omega}{2}t\right) \end{pmatrix} \tag{2.2.4}$$

where $d = \gamma B_0 - \omega$ which is called detuning, $\omega_2 = \sqrt{d^2 + (\gamma B_1)^2}$, $g = d/\omega_2$ and $c = \gamma B_1/\omega_2$. In order to calculate how the spins are affected by a flip sequence with arbitrary ω, the time evolution operator $U(t)$ can be applied to the initial state $\Psi_0 = (1,0)^T \equiv |\uparrow\rangle$:

$$|\Psi(t)\rangle = U(t)\,|\Psi_0\rangle \quad . \tag{2.2.5}$$

To observe the spatial orientation of the spin, the expectation values of the Pauli matrices are calculated:

$$I_{x,y,z} = \langle\Psi(t)|\,\sigma_{x,y,z}\,|\Psi(t)\rangle \quad . \tag{2.2.6}$$

In Fig. (2.2.2), the situation is shown when the nuclear spin of xenon atoms is flipped. Here, the z component of the spins is regarded after a flip sequence is applied. A flip sequence is a sine/cosine wave modulated by a rectangular function with duration Δt. Throughout this thesis, Δt was chosen to 1ms. Furthermore, it was assumed, that $B_0 =$ 2 mT and $\phi = 0$. When the z component is zero, the spins have been flipped by an angle of 90°. In Fig. (2.2.3), slices of constant frequencies with and without detuning are shown.

Without detuning (d=0) the flip angle is proportional to the B_1 amplitude as stated in equation(2.2.2). For a significant detuning however, this dependence does not hold

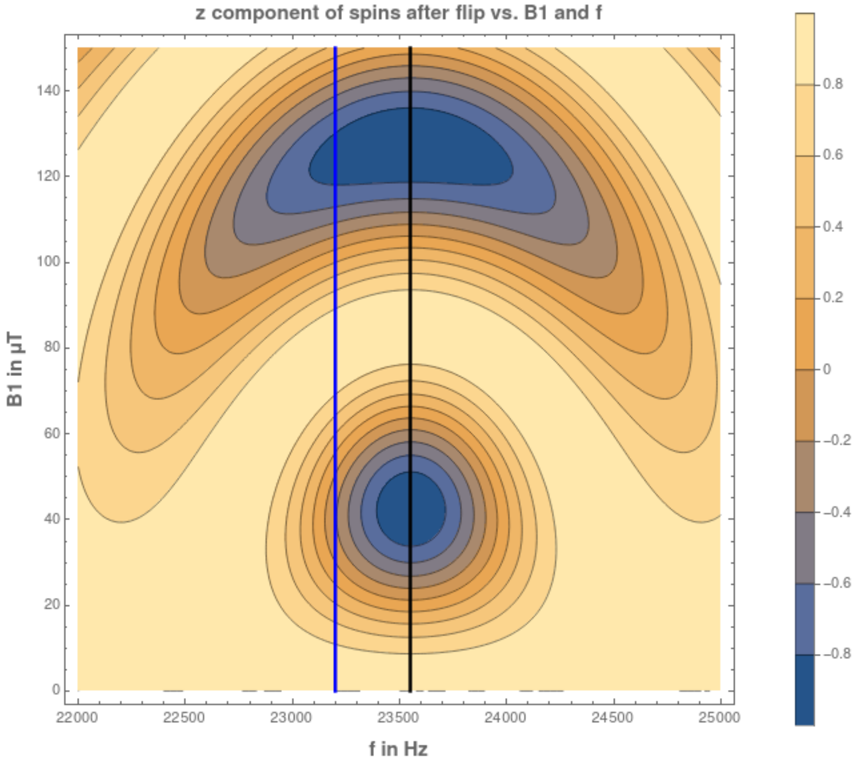

Figure 2.2.2: Z component of a spin after a flip sequence with arbitrary ω (or f) and different B_1 amplitude.

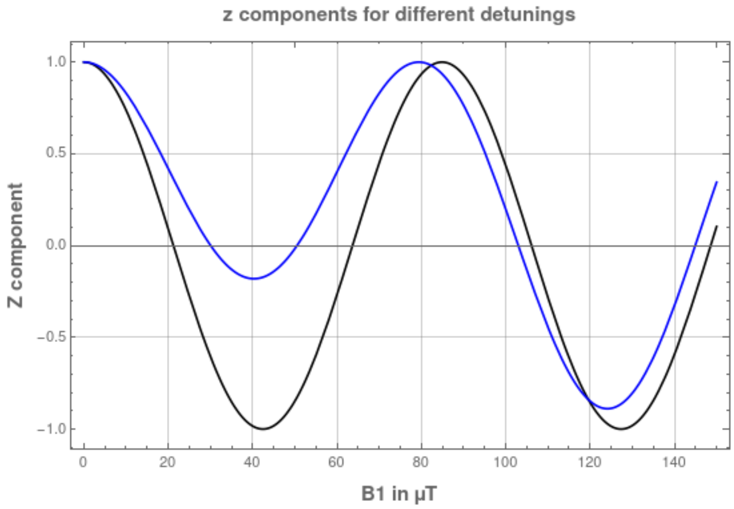

Figure 2.2.3: Different slices of Fig. (2.2.2). Black: $f \approx \omega_L/(2\pi)$ or d=0, Blue: $f \approx$ 23.2 kHz or d $\approx$ 350 Hz.

anymore. It might be possible to flip the spins by 90° but for a flip by 180° this is not the case. As it will become apparent in the next sections of this thesis, measurements with water and ^{129}Xe are performed using a detuning on purpose.

Finally, a short remark is made: in the case above, a rotating B_1 field was assumed. This requires two transversal coils which are fed by a sine and a cosine signal. In reality, only one transversal coil is used for simplicity generating a linear B_1 field. However, this linear B_1 field can be regarded as superposition of two waves rotating in opposite direction. One rotating wave couples much better to the spins than the other one which is neglected. It is important to mention that the B_1 amplitude is now reduced by a factor of two. The calculation above is referred to as rotating-wave approximation. Including both rotating waves would yield to a small correction which is known as Ramsay-Bloch-Siegert shift.

2.3 Mechanisms of relaxation

As it was stated above, a single spin has two energy eigenstates which are spin up (parallel to B) or spin down (antiparallel to B). During spin precession, a coherent sum of both states is yielding to perpendicular orientation. The spin-spin relaxation time T_2 gives the lifetime of this coherent sum. This transverse relaxation is an independent process from the longitudinal relaxation. The spin-lattice relaxation time T_1 quantifies the time scale needed to achieve thermal equilibrium between the spin-up and the spin-down state. It is important to mention that the relaxation is a collective phenomenon which consists of many different contributions.

2.3.1 Longitudinal relaxation

In the following, these contributions for T_1 should be introduced in more detail. At the end, these contributions are added inversely:

$$\frac{1}{T_1} = \frac{1}{T_{1,\mathrm{grad}}} + \frac{1}{T_{1,\mathrm{wall}}} + \frac{1}{T_{1,\mathrm{bin}}} + \frac{1}{T_{1,\mathrm{vdW}}} + \frac{1}{T_{1,O_2}} \quad . \tag{2.3.1}$$

2.3.1.1 Gradient relaxation

In order to observe and quantify polarization, a magnetic holding field $\vec{B}_0$ is necessary. Ideally, it is perfectly homogeneous with known orientation, say in z direction. Under experimental conditions, however, this is not the case. There are always small inhomogeneities $\vec{B}_1(\vec{r})$ on top of $\vec{B}_0$. Regarding a single spin confined in a measuring volume, it may diffuse along arbitrary paths within the sample cell. In the co-moved coordinate system of the spin, the magnetic field seems to be time dependent. As it was shown in the paragraph above, a time dependent magnetic field may cause a spin-flip. For a thermally polarized spin sample this is not critical but for a HP spin sample it obviously is because the polarization which is lost in this way cannot be recovered anymore. This relaxation mechanism depends on the properties of the magnetic holding field as well as the movement of the spins within the sample cell which is quantified by the diffusion constant D. D depends on pressure and temperature in the following way:

$$D = \frac{p_0}{p}\frac{T^{3/2}}{T_0^{3/2}} D_0 \quad . \tag{2.3.2}$$

For a spherical sample volume T_1 can be calculated by [23]

$$\frac{1}{T_1} = 2D\frac{|\nabla B_{1,x}|^2 + |\nabla B_{1,y}|^2}{B_0^2} \times \sum_n \frac{1}{|x_{1,n}^2 - 2| \cdot (1 + D^2 x_{1,n}^4 (\gamma B_0)^{-2}) R^{-4}} \quad . \tag{2.3.3}$$

In this expression, $\nabla B_{1,x}$ represents the gradient in x,y,z direction of the x component of B_1 (and for y correspondingly). The numbers $x_{1,n}$ are the zeros of the derivative of the spherical Bessel functions. The exact values can be found in [23]. To maximize T_1 it is obvious that inhomogeneities of the magnetic holding field should be kept low. The second parameter which can be tuned is the diffusion coefficient. In the Helium-Xenon Experiment, as the name may suggest, a mixture of ^{3}He and ^{129}Xe is used. The diffusion coefficient can be changed by adding a buffer gas like N_2 or CO_2 to that mixture which does not affect the overall magnetization. The exact optimal compositions are not easy to determine as they influence other relaxation mechanisms as well.

2.3.1.2 Wall relaxation

Another important process of relaxation is the interaction with the wall. In many applications, the spins are confined within a glass cell (cylindrical or spherical). Paramagnetic and ferromagnetic centers in the glass wall may yield to spin-flips for atoms near the surface. Therefore, T_1 depends on the ratio of the volume and the surface:

$$\frac{1}{T_1^{\text{wall}}} = \eta \frac{A}{V} \quad . \tag{2.3.4}$$

η is called the relaxivity and is assumed to be a specific constant of each cell. While wall-relaxation times for ^{3}He of more than hundred hours can be reached [24], the maximum T_1^{wall} of about 18h for xenon [25] is much smaller. Much research was done to increase T_1^{wall} for xenon relaxation. E.g. several coatings [26], [27], [28] and materials have been tested. For the purpose of the Helium-Xenon Experiment, a glass called GE-180 yielded to the best results. It is one of the aluminosilicate glasses which was fabricated by the company General Electric. A spherical cell provides the best ratio of surface and volume. By increasing its radius R, T_1^{wall} can be further improved. It should be noted that increasing R may reduce the overall T_1 due to other relaxation processes, like gradient relaxation.

2.3.1.3 Binary and Van-der-Waals relaxation

In the following relaxation processes, the interaction of the atoms is regarded. Two types of interactions are relevant. In the first type, the binary collisions, two atoms interact during a short time period with each other. The nuclear spin is coupled to the relative angular momentum of colliding atoms via the magnetic dipole-dipole interaction. In that way, nuclear-spin polarization can be transferred to the orbital angular momentum and might be therefore lost. For ^{3}He and ^{129}Xe, the relaxation rates arising from binary collisions are given by [29] and [30].

$$\frac{1}{T_{1,\text{bin}}^{\text{He}}} = \frac{1}{754\text{h}} \frac{p}{p_0} \frac{T_0}{T} \tag{2.3.5}$$

$$\frac{1}{T_{1,\text{bin}}^{\text{Xe}}} = \frac{1}{56\text{h}} \frac{p}{p_0} \frac{T_0}{T} \tag{2.3.6}$$

T_0 is the standard room temperature and p_0 is the normal pressure. The main conclusion of these formulas is that $T_{1,\mathrm{bin}}$ can be maximized by minimizing the densities of the noble gases. It is important to mention, that the gradient relaxation is also pressure dependent as the diffusion coefficient enters the equation. Furthermore, the measured overall signal is proportional to the number of spins and therefore to the pressure as well which is why the pressure should not be too small. For this reason, a very large polarization of the noble gases is desirable providing a large signal at low pressures.

The second interaction is the formation of long-lived Van-der-Waals molecules. In principle, all combinations ^{3}He-^{3}He, ^{129}Xe-^{3}He and ^{129}Xe-^{129}Xe are allowed but only the last one is relevant. The lifetime of such a molecule is much longer than the time scale of a binary collision. During this time, spin polarization can also be converted to rotational or vibrational modes of the molecule. However, the lifetime of such a Van-der-Waals molecule can be significantly reduced by adding a buffer gas like N_2 to the helium-xenon-gas mixture [31], [32]:

$$T_{1,\mathrm{vdW}}^{\mathrm{Xe}} = 4.6\mathrm{h}\left(1 + r_{\mathrm{B}}\frac{p_{\mathrm{B}}}{p_{\mathrm{Xe}}}\right) \quad . \tag{2.3.7}$$

The more buffer gas is contained in the mixture the faster the Xe-Xe molecules are broken up. r_{B} is the breakup rate depending on which buffer gas is used. Adding a buffer gas changes also the diffusion coefficient and therefore affects other relaxation mechanisms.

2.3.1.4 O_2 relaxation

Paramagnetic atoms or molecules have unpaired valence electrons like O_2. The spins of these electrons can couple to the nuclear spins of the polarized noble gases and may yield to a loss of polarization. The mechanisms for that are very similar to those occurring in binary collisions explained in the paragraph above. The relaxation rate is proportional to the density of oxygen [33], [34]:

$$T_{1,O_2}^{\mathrm{He}} = \frac{2.5\ \mathrm{s}\cdot\mathrm{bar}}{p_{O_2}} \tag{2.3.8}$$

$$T_{1,O_2}^{\mathrm{Xe}} = \frac{2.1\ \mathrm{s}\cdot\mathrm{bar}}{p_{O_2}} \quad . \tag{2.3.9}$$

Due to these results, the conclusion is very simple: get the vacuum system as clean as possible and remove any leaks. When a T_{1,O_2} of 100 h was desired the partial pressure of O_2 must not exceed a value of 5×10^{-3} mbar. At first glance, this seems to be easily implementable. However, as it will become apparent in the next chapters that other conditions have to be met as well. For instance, all gas lines transporting polarized gases have to be made of non-magnetic materials like glass and plastic. In this context, it would be much harder to establish such pressure values. For this reason, a method of standardization was introduced to ensure a sufficient quality of the vacuum. It is presented in the Appendix 8.

2.3.2 Transversal relaxation

All mechanisms presented above contribute to the longitudinal relaxation time T_1. But during the measurement cycle of the Helium-Xenon Experiment, the spins are flipped perpendicularly to the magnetic holding field. Therefore, the quantity of interest is T_2^*. It can be calculated by:

$$\frac{1}{T_2^*} = \frac{1}{T_1} + \frac{1}{T_{2,\mathrm{grad}}} \quad . \tag{2.3.10}$$

All mechanisms presented before are entering this equation and are important for T_2^* as well. The second contribution affects T_2^* directly. Assuming a magnetic field gradient across the sample cell on top of B_0, the Larmor precession frequency ω_L is changing locally. Therefore, the overall sum is decaying much faster, yielding to T_2^* which depends on magnetic field gradients. For linear gradients the exact dependency is given by [23]:

$$\frac{1}{T_{2,\mathrm{grad}}} = \frac{8R^4\gamma^2}{175D}\left(a(\lambda)\cdot\left(|\nabla B_x|^2 + |\nabla B_y|^2\right) + |\nabla B_z|^2\right) \tag{2.3.11}$$

with

$$a(\lambda) = \frac{175}{8}\lambda \cdot \sum_n \frac{1}{|x_{1,n}^2 - 2| \cdot (1 + x_{1,n}^4\lambda)} \tag{2.3.12}$$

and

$$\lambda = \frac{D^2}{\gamma^2 B_0^2 R^4} \quad . \tag{2.3.13}$$

In the high-pressure regime, the precession time $t_p = (\gamma B_0)^{-1}$ is much smaller than the diffusion time $t_d = R^2/D$. In this case, when $t_p \ll t_d$, λ goes to zero and $a(\lambda)$ vanishes. Typical values for the T_2^* relaxation time of HP xenon can be calculated with the following parameters: $B_0 = 400$ nT, $R = 5$ cm, $p = 100$ mbar yielding to a diffusion constant for xenon of $D = 0.58\ \mathrm{cm}^2/\mathrm{s}$ by using (2.3.2) and $D_0 = 0.058\ \mathrm{cm}^2\ \mathrm{bar/s}$ [35]. Assuming a longitudinal magnetic field gradient of $|\nabla B_z| = 10$ pT/cm, a T_2^* relaxation time of around 10 hours is expected. For $|\nabla B_z| = 5$ pT/cm, T_2^* exceeds already 40 hours. This numerical example shows why it is important to optimize the gradients and why the experiment has to be performed within an MSR.

2.4 HP noble gases

A very important step contained in the preparation of the Helium-Xenon Experiment is the hyperpolarization of noble gases. Only large polarizations P will yield to clean signals and therefore to precise measurements. When P is of order 10^{-2} a gas is called HP. As it was mentioned in a previous section, the thermal polarization of a xenon sample is in the regime of 10^{-6} (in magnetic holding fields of 1 T). This suggests that some effort is needed to achieve hyperpolarization. The processes of polarizing the noble gases ^{3}He and ^{129}Xe both rely on optical pumping methods in which a powerful laser (several watts) in the near infrared regime is used. Comparing the two processes there are also some differences: for the polarization of ^{3}He metastability exchange optical pumping (MEOP) is applied [36] whereas for ^{129}Xe spin exchange optical pumping (SEOP) is used [37]. The latter method will be discussed in detail within the next section.

2.4.1 SEOP of ^{129}Xe

Spin exchange optical pumping which is used to polarize ^{129}Xe consists of two steps. In the first step rubidium atoms are polarized by optical pumping. In a second step, the polarization of the rubidium atom is transferred to the xenon atom. Both steps should be carefully discussed.

2.4.1.1 Optical pumping of Rubidium

Rubidium is an alkali metal with one single valence electron in the 5th shell. Regarding the energy levels of this atom, there are several effects to account for. The Bohr model is the simplest model describing atoms and explaining the observation of electron shells. This model is manifested in Schrödinger's equation. Going to a higher resolution in energy, however, an obvious discrepancy between theory and experiment is observed. The main reason for this is the fact that the Schrödinger equation is not relativistic and does not describe fermions like electrons. This can be achieved with the Dirac equation. As a result, new effects enter which are relativistic corrections of the atomic potential and the well-known LS coupling. They are also called fine structure and resolve most of the discrepancies between theory and experiment. In Fig. (2.4.1) this effect is shown. The 5p level splits into $5\mathrm{p}_{1/2}$ and $5\mathrm{p}_{3/2}$. The ground state $5\mathrm{s}_{1/2}$ does not split. Therefore, two transitions are in principle possible: D_1 ($5\mathrm{s}_{1/2} \rightarrow 5\mathrm{p}_{1/2}$) and D_2 ($5\mathrm{s}_{1/2} \rightarrow 5\mathrm{p}_{3/2}$). For polarizing the Rb atoms the D_1 transition is used which demands for a light source with a wavelength of 794.7 nm. Going to even smaller energies, the nuclear spin of the rubidium atoms becomes more relevant because it can couple with the total electron spin J. It is important to mention that rubidium might occur in different isotopes with different nuclear spins. The only two stable isotopes are ^{85}Rb having a nuclear spin of $I = 5/2$ and ^{87}Rb with $I = 3/2$. When I couples with J than the values for the overall spin can be $|I - J| \leq F \leq |I + J|$. Depending on the regarded isotope, the energy levels shown in Fig. (2.4.1) will change. These additional energy levels are also called hyperfine structure. In order to measure a polarization, a quantization axis needs to be defined. This is done by applying a magnetic field in a specific direction. As a consequence, the F states will split into different sub states with quantum number m_F due to the Zeeman effect. The quantum numbers are integers with $-F \leq m_F \leq F$.

In the next paragraph the polarization process for ^{87}Rb will be discussed. For ^{85}Rb the following argumentation would be analogous. When polarizing rubidium, the goal is to pump all valence electrons into a specific state which is the $5\mathrm{s}_{1/2}$ state with m_F=+2 for ^{87}Rb. In the following, this state is called the target state. The more electrons are in the target state the better the polarization becomes. This can be achieved by using right-handed circularly polarized light (σ^+) with corresponding wavelength for the D_1 transition. In this case, the selection rules allow for transitions with $\Delta m_F = +1$ only. In Fig. (2.4.1) these transitions are drawn. The only sub state in $5\mathrm{s}_{1/2}$ which is not affected by the σ^+ light is the target state. After a D_1 transition a 5s electron is in the 5p state. For many rubidium atoms with different populations of the m_F sub states it comes to an equilibration by a process called collisional mixing. After a lifetime of a few nanoseconds the electrons will decay into one of the m_F sub states of $5\mathrm{s}_{1/2}$. Here, the target state is also included. Over some time periods the population of this sub state will increase whereas the populations of the other m_F states of $5\mathrm{s}_{1/2}$ will decrease. In this way, a polarization of rubidium can be achieved. When the electrons are in the target state, the total spin $\vec{F}$

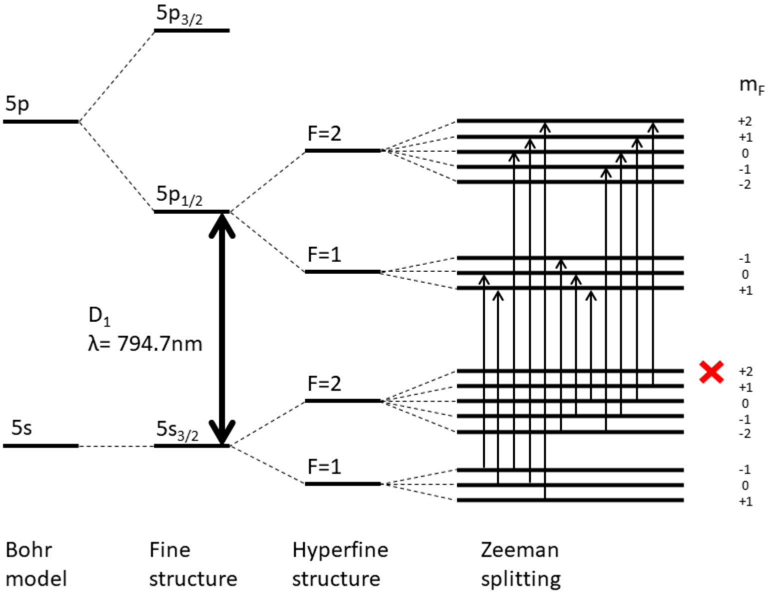

Figure 2.4.1: Energy levels of ^{87}Rb (I=3/2) showing all transitions induced by right-handed circularly polarized light. Please note: energies are not to scale. Figure inspired and adapted from [38].

is fully aligned which means that both the nuclear spin and the electron spin are oriented parallel to the magnetic field.

Starting with a laser of certain power P and a certain flux $\Phi(\vec{r},\nu)$ which has a spatial and spectral dependency, we can define an optical pumping efficiency γ_{OP}. This efficiency is a measure of how much polarization is transferred from the laser into the vapor of rubidium atoms within a given time. In order to quantify γ_{OP}, the shape of the D_1-absorption line of rubidium must be known. A Lorentzian is a suitable description:

$$\sigma(\nu) = \frac{\sigma_0}{1 + 4(\nu - \nu_0)^2/\Gamma_{\mathrm{abs}}^2} \quad . \tag{2.4.1}$$

ν_0 is the central frequency and Γ_{abs} the Full-Width-Half-Maximum (FWHM). The maximum value of absorption σ_0 was calculated to be $3.2 \cdot 10^{-13}$ cm^2 [39]. For different gas mixtures containing rubidium, both, ν_0 and Γ_{abs} may vary. It is mandatory that the photon flux $\Phi(\vec{r},\nu)$ of the laser optimally matches the absorption line of rubidium. Otherwise, the laser power is just wasted. Together with the photon flux $\Phi(\vec{r},\nu)$, the optical pumping efficiency can be defined:

$$\gamma_{\mathrm{OP}}(\vec{r}) = \int_0^\infty \Phi(\vec{r},\nu) \cdot \sigma(\nu) d\nu \quad . \tag{2.4.2}$$

In order to maximize γ_{OP} in the experiment, the width of the absorption line Γ_{abs} can be tuned by changing the pressure of the gas mixture containing the rubidium vapor. This is achieved by adding buffer gases which are ^{4}He and N_2. In [40] it is shown that Γ_{abs} depends linearly on the partial pressures:

$$\Gamma_{\mathrm{abs}} = \{(18.0 \pm 0.2)p_{\mathrm{He}} + (17.8 \pm 0.3)p_{N_2} + (19.2 \pm 2.0)p_{\mathrm{Xe}}\} \frac{T_0}{T} \text{ [GHz]} \quad . \tag{2.4.3}$$

The central frequency ν_0 can be matched by shifting the wavelength of the laser using thermo-optical effects. To write down the rubidium polarization, the spin destruction rate Γ_{SD} needs to be introduced. It absorbs all contributions from processes yielding to a loss of rubidium polarization and will be regarded in detail. At this point, it is possible to write the following rate equation:

$$\frac{dP_{\mathrm{Rb}}}{dt} = \gamma_{\mathrm{OP}}(1 - P_{\mathrm{Rb}}) - \Gamma_{\mathrm{SD}} P_{\mathrm{Rb}} \quad . \tag{2.4.4}$$

Starting from unpolarized rubidium, the solution is given by

$$P_{\mathrm{Rb}}(t) = \frac{\gamma_{\mathrm{OP}}}{\gamma_{\mathrm{OP}} + \Gamma_{\mathrm{SD}}} \left(1 - \exp(-(\gamma_{\mathrm{OP}} - \Gamma_{\mathrm{SD}})t)\right) \quad . \tag{2.4.5}$$

The equilibrium is reached very fast, typically after a few milliseconds:

$$P_{\mathrm{Rb}} = \frac{\gamma_{\mathrm{OP}}(\vec{r})}{\gamma_{\mathrm{OP}}(\vec{r}) + \Gamma_{\mathrm{SD}}} \quad . \tag{2.4.6}$$

The rubidium polarization is maximized when the spin-destruction rate Γ_{SD} is minimum. There are many different contributions to Γ_{SD}. If an electron is excited to the 5p state during the pumping process and decays back to the 5s state, then σ^+, σ^- or π photons can be emitted. When a π or a σ^- photon is absorbed by an electron in the target state it comes to a "de-pumping" and therefore a destruction of polarization. To prevent this, N_2 is added as a buffer gas acting as quencher. The re-emitted photons are absorbed and the energy is converted into rotational and translational modes of the nitrogen molecule. Other mechanisms are caused by wall collisions or magnetic field gradients. The interaction of Rb with other gas atoms is also an important contribution to spin destruction. It is closely connected to the spin exchange between Rb and Xe and will be therefore further regarded within the next section.

2.4.1.2 Spin exchange with Xenon

In a second step, the polarization of the rubidium has to be transferred to the ^{129}Xe atoms. This is achieved by mixing the xenon gas with the rubidium vapor during the optical pumping process. Furthermore, the gases ^{4}He and N_2 are added which are acting as buffer gases. The reasons for that were already mentioned above and another reason will be discussed in this section. The transfer of polarization from Rb to ^{129}Xe is guided by mainly two separate processes.

These processes of spin exchange can be described by the following spin-dependent interaction potential [42]:

$$V_1(\vec{R}) = \alpha(R)\vec{N} \cdot \vec{S} + A_b(R)\vec{I}_b \cdot \vec{S} \quad . \tag{2.4.7}$$

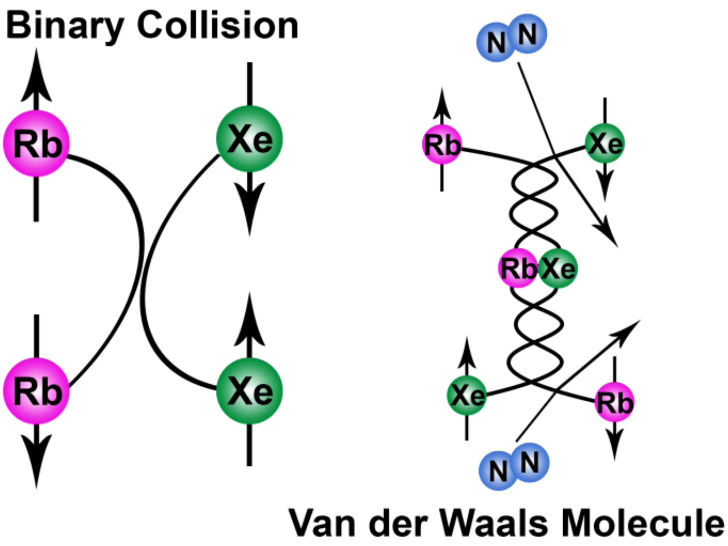

Figure 2.4.2: Two processes are relevant transferring the rubidium polarization to the xenon atoms. Left: binary collisions, right: three body interactions, source: [41].

The first term describes the so-called spin-rotation interaction. It couples the rubidium-electron spin $\vec{S}$ to the rotational angular momentum $\vec{N}$ of the interacting rubidium-xenon system. The coupling constant α depends on the inter-atomic separation $\vec{R}$. In the second term, the hyperfine interaction is denoted in which the rubidium-electron spin $\vec{S}$ is coupled to the nuclear spin $\vec{I}_b$ of the xenon atom. In summary, it can be noted that only the angular momentum of the rubidium-electron spin $\vec{S}$ and not the total angular momentum $\vec{F}$ is transferred to the xenon nucleus.

The first process is described by binary collisions between Rb and ^{129}Xe atoms. It can be simply characterized by following equation:

$$\mathrm{Rb}(\uparrow) + \mathrm{Xe}(\downarrow) \rightarrow \mathrm{Rb}(\downarrow) + \mathrm{Xe}(\uparrow) \quad . \tag{2.4.8}$$

In a gas mixture at roughly 400 K, the velocities of both, rubidium and xenon atoms, are of the order 100 m/s. A typical interaction range of the given potential above is around one Angström. Therefore, the correlation time of this interaction is roughly 10^{-12} s. In order to quantify the spin-exchange rate of binary collisions, the velocity-averaged cross section is needed:

$$\gamma_{\mathrm{SE}}^{\mathrm{bin}} = \langle \sigma_{\mathrm{bin}} v \rangle n_A \quad . \tag{2.4.9}$$

The larger the volume density n_A of rubidium atoms is, the more often binary collisions occur and the larger is the spin-exchange rate will become. However, binary collisions may also contribute to the spin-destruction rate of the polarized rubidium. These collisions may occur with all buffer gas atoms:

$$\Gamma^{\mathrm{bin}} = \sum_i [G_i] \cdot \kappa_{\text{Rb-X}} \quad . \tag{2.4.10}$$

Γ^{bin} is proportional to the number density $[G]$ of the gas G. The spin-destruction coefficients κ depend on the gas and, in general, on temperature. Their specific values and dependencies can be found in [43]. In this sense, both the desired spin-exchange rate $\gamma_{\mathrm{SE}}^{\mathrm{bin}}$ and Γ^{bin} are sub-processes contained in Γ_{SD}.

In contrast to the first process, the interaction time of the second process is several orders of magnitude longer. It is a three-body process in which rubidium and xenon forms a Van-der-Waals molecule under the influence of a third buffer-gas atom (N_2). The equation for this process is:

$$\mathrm{Rb}(\uparrow) + \mathrm{Xe}(\downarrow) + N_2 \rightarrow \mathrm{RbXe} + N_2 \rightarrow \mathrm{Rb}(\downarrow) + \mathrm{Xe}(\uparrow) + N_2 \quad . \tag{2.4.11}$$

Due to the long lifetime of this molecule, it is more likely that this molecule is broken up by another collision with a buffer-gas atom. Especially N_2 provides an efficient break-up rate. The spin-exchange rate is given by [44]

$$\gamma_{\mathrm{SE}}^{\mathrm{vdW}} = \frac{n_{\mathrm{Rb}}}{\sum_i \frac{[G_i]}{\gamma_i}} \tag{2.4.12}$$

whereas the spin-destruction rate is given by [38]

$$\Gamma^{\mathrm{vdW}} = \frac{66183}{1 + 0.92\frac{[\mathrm{N}_2]}{[\mathrm{Xe}]} + 0.31\frac{[\mathrm{He}]}{[\mathrm{Xe}]}} \cdot \left(\frac{T}{423\ \mathrm{K}}\right)^{-2.5} \quad . \tag{2.4.13}$$

To obtain $\gamma_{\mathrm{SE}}^{\mathrm{vdW}}$, the spin exchange efficiencies γ_i are added inversely weighted by the number densities of the individual gas components $[G_i]$. To keep the spin-destruction rate Γ^{vdW} caused by van-der-Waals molecules low, the partial pressure of Xe should be low compared to the pressure of the buffer gases. Increasing the fraction of N_2 will further reduce Γ^{vdW} because the van-der-Waals molecule is broken up much faster. On the other hand, reducing the lifetime of the molecule will also reduce the spin-exchange efficiency $\gamma_{\mathrm{SE}}^{\mathrm{vdW}}$. Furthermore, the amount of N_2 will affect the quenching behavior for the polarized rubidium. For this reason, an optimal fraction of N_2 exists yielding to a maximum spin transfer. The helium does not affect the pumping process significantly and can be therefore used to tune the overall pressure of the gas mixture matching the rubidium-absorption line to the spectral width of the laser light.

Applying similar considerations as in the previous section, it can be deduced that

$$P_{\mathrm{Xe}} = \frac{\gamma_{\mathrm{SE}}}{\gamma_{\mathrm{SE}} + \Gamma_{\mathrm{Xe}}} P_{\mathrm{Rb}} [1 - \exp(-t_{\mathrm{res}}/(\gamma_{\mathrm{SE}} + \Gamma_{\mathrm{Xe}}))] \tag{2.4.14}$$

where the overall spin-exchange rate γ_{SE} is the sum of $\gamma_{\mathrm{SE}}^{\mathrm{bin}}$ and $\gamma_{\mathrm{SE}}^{\mathrm{vdW}}$. Thus, the xenon polarization is directly proportional to the rubidium polarization. Γ_{Xe} is the relaxation rate of xenon caused by effects like wall relaxation, magnetic field gradients, etc. The residence time t_{res} describes how long a xenon atom stays within the rubidium vapor. When it is chosen long enough the equilibrium is reached which is the maximum xenon polarization that can be achieved.

2.4.2 MEOP of ^{3}He

For completeness, a few words should be lost about the polarization process of ^{3}He. In principle, it is possible to hyperpolarize ^{3}He with SEOP [45, 42, 46] as explained above for ^{129}Xe. In the scope of this experiment, it was decided to use the method of metastability optical pumping (MEOP). The big advantage of this method over SEOP is that large polarizations can be reached in a much shorter time. In Fig. (2.4.3) the underlying process is shortly summarized.

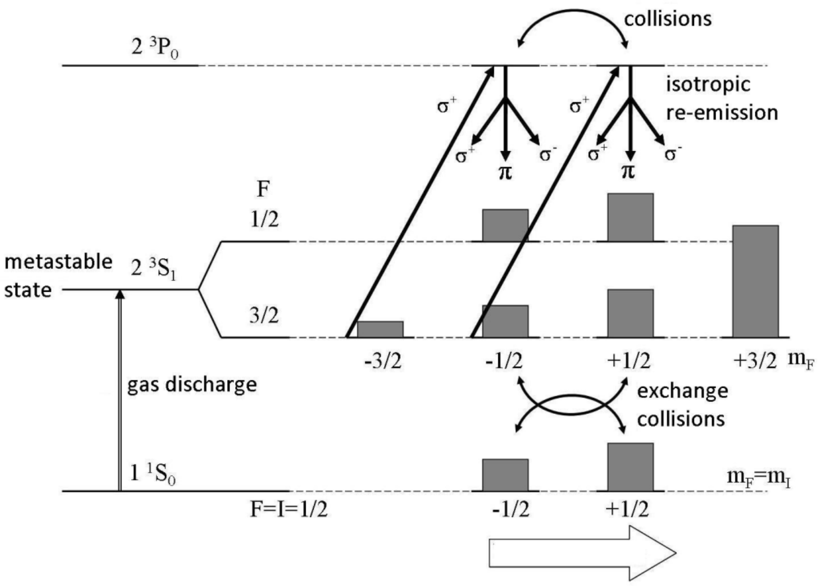

Figure 2.4.3: Energy levels of ^{3}He. The σ^+ light pumps the lower m$_F$ states to higher m$_F$ states, source: [47].

The ground state of ^{3}He 1^1S_0 can be excited into the metastable state 2^3S_1 by a weak gas discharge. According to the selection rules, this transition is forbidden. Therefore, the lifetime of around 1 ms is quite long. During this time, the valence electrons of helium atoms in this state can be excited into the 2^3P_0 state by using right-handed circularly polarized laser light with a wavelength of 1083 nm. The consequence is the increase of the Zeeman levels m_F by +1. This state has a much shorter live time of roughly 100 ns. As in the optical-pumping process of rubidium, collisional mixing will yield to an equal population of the m_F levels in the 2^3P_0 state. After spontaneous de-excitation the net-angular momentum is not changed. For this reason, higher m$_F$ states are more populated than lower m$_F$ states as they are not addressed by the right-handed laser light. This results in an overall polarization of the electron spin. Via the hyperfine interaction, the electron spin is coupled to the nuclear spin of ^{3}He which leads to a nuclear polarization. When the 2^3S_1 state de-excites back to the ground state 1^1S_0, e.g. via interaction with unpolarized atoms, the nuclear polarization is preserved. Further details and a quantitative description of MEOP of ^{3}He can be found in [48].

2.5 Measuring precessing spins using a SQUID

In the context of the Helium-Xenon Experiment, the HP noble gases helium and xenon are mixed and stored in a spherical glass cell. Assuming a homogeneously magnetized sphere, it can be shown [49] that the magnetic field within that sphere is homogeneous. Outside the sphere the magnetic field behaves exactly like a dipole:

$$\vec{B}(\vec{r},t) = \frac{\mu_0}{4\pi r^2} \frac{3\vec{r}(\vec{m}(t)\cdot\vec{r}) - \vec{m}(t)r^2}{r^3} \quad . \tag{2.5.1}$$

The vector $\vec{m}$ represents the magnetization and depends on the polarization of the noble gases. When the spins are precessing coherently, $\vec{m}$ is changing with time yielding to a time dependent magnetic field.

This magnetic field can be measured using a SQUID magnetometer. As indicated by the first letter in its name, a SQUID consists of a loop which is superconducting. For this loop the magnetic flux is quantized in units of $\Phi_0 = \frac{h}{2e}$. When the external magnetic flux is changed, internal screening currents I_s will compensate for this flux to a multiple of Φ_0. Increasing the external flux linearly will yield to a periodic behavior of I_s. Experimentally, however, it is challenging to detect I_s directly. For this reason, the loop is divided into two halves by two thin isolating or normally conducting layers forming two Josephson junctions (see Fig. (2.5.1)). The Josephson effect describes the quantum mechanical tunneling of cooper pairs through that barrier [50]. By applying a properly chosen bias current I to that loop, the screening current can be translated into a voltage U across the SQUID. Further details addressing the working principle of SQUIDs can be found in [51], [52] and [53].

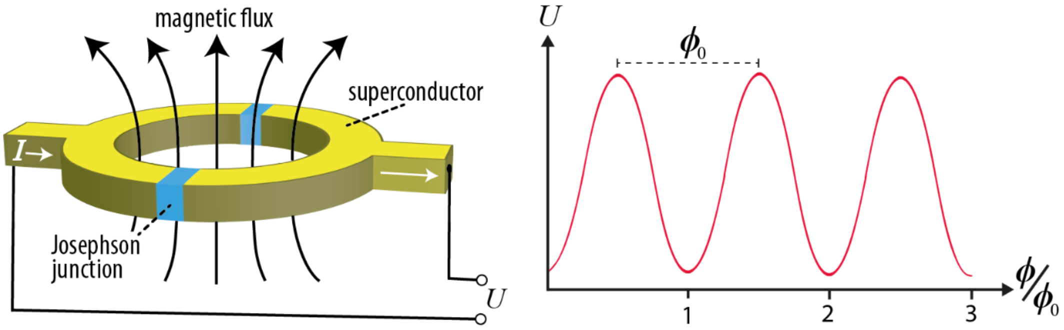

Figure 2.5.1: Configuration of a SQUID acting as flux-to-voltage converter. Source: [17].

The bias current determines the operating point in the characteristic curve (Fig. (2.5.1), right). To achieve maximum sensitivity to Φ it should be chosen at the steepest point at $(2n+1)/4\Phi_0$. To further increase sensitivity, a superconducting gradiometer coil consisting of two antiparallel windings is coupled into the SQUID (see Fig. (2.5.2)). With this configuration, only local gradients can be measured whereas homogeneous background noise is discriminated which further increases the SNR. Assuming the field of a spherical cell containing HP gas given in equation(2.5.1), the measured signal is proportional to

$$S \sim \frac{1}{d^3} - \frac{1}{(d+b)^3} \tag{2.5.2}$$

where b is the distance between the two windings of the coil and d the distance between the cell and the lower winding.

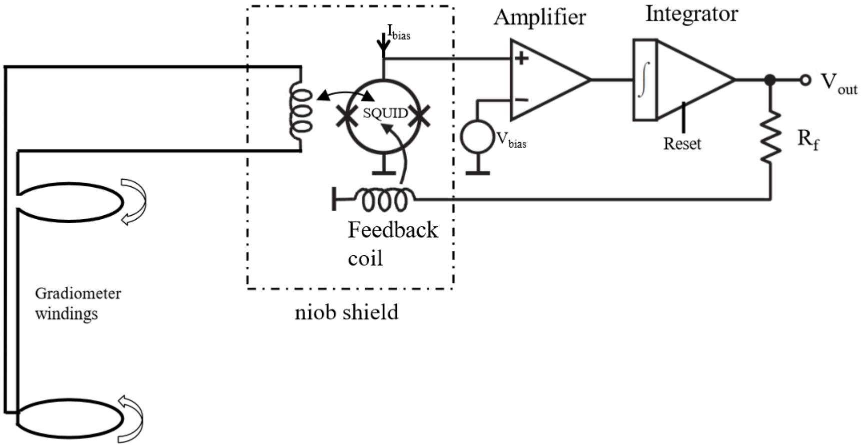

Figure 2.5.2: SQUID in flux-locked feedback mode. Source: [53].

Typically, the SQUIDs are operated in flux-locked feedback mode. This means that the operating point is never left, regardless of the external flux. When the flux changes, the change in voltage is amplified and integrated yielding to a current which is fed back into the SQUID via a feedback coil. The flux can be measured via the voltage across the feedback resistance R_f. The main advantage of this approach is that the characteristic curve is linearized. This works only when the changes of the flux (in the present case, of the gradients) are not too large otherwise the screening currents will jump when compensating to the next flux quantum.

In order to operate the SQUID system within the MSR, they have to be cooled with liquid helium. At liquid-helium temperatures of 4 Kelvin the SQUID will become superconductive. To achieve long measurement times of roughly one weak, a non-magnetic dewar was constructed storing about 16 liters of liquid helium which has to be filled in the beginning of a measurement. Further details concerning the practical operation of the SQUID system can be found in [54].

Figure 2.5.3: SQUID system with dewar within the MSR. The measurement cell is mounted below the SQUID at the center of the MSR.

Chapter 3

The MSR

Parts of the results presented in this chapter have been published in a technical paper [55] and are contained within the bachelor's thesis of Thang Le Pham Huy [56].

As described in the chapter before, it is crucial to perform the Helium-Xenon Experiment in a very clean magnetic environment. Two aspects are of significant importance. Firstly, the magnetic field should be very stable in time. For the experiment, a stability of 10^{-4} would be desirable. But this level of stability is far of reach due to external influences, e.g. movement of ferromagnetic objects like cars, elevators etc. or the change of the Earth's magnetic field due to geological processes. A second criterion for a suitable environment is the gradient of magnetic fields. As discussed before, the existence of gradients greatly reduces the T_2^* relaxation time and therefore the sensitivity of this experiment.

For these reasons a dedicated shielding of the external magnetic field is necessary. The standard approach is the use of so-called Mu-metal. This is a very ferromagnetic alloy which has a large magnetic permeability reaching to values of $\mu_r \approx 200000$ and above [57]. When the experiment is completely surrounded by a sphere of Mu-metal, a shielding of an external magnetic field can be established. This can be explained illustratively: the larger μ_r of a certain material is, the more magnetic field lines are forced to go through this material and thus the larger the shielding effect becomes. This is also depicted in Fig. (3.0.1).

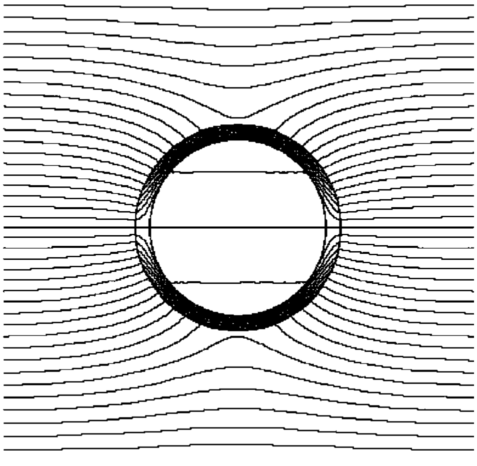

Figure 3.0.1: Magnetic shielding using a highly permeable material [58].

This concept was used when an MSR was constructed at the Physikalisches Institut in Heidelberg in 2021. This room was manufactured by the company Vacuumschmelze in Hanau, Germany. It has an outer edge length of 3 m in all directions and is mounted on a platform of aluminum plates and rails that lift the whole MSR 20 cm above the ground level. This has been done for two reasons: Firstly, the building and so the floor is made of reinforced concrete which influences the external magnetic field considerably. This influence becomes smaller with larger distance. Secondly, this lifting allows for adding active compensation coils in the afterward if necessary.

Figure 3.0.2: Readily assembled MSR. The introduced coordinate system is used for measurements inside the MSR.

Instead of one shielding layer, as shown in Fig. (3.0.1), the MSR consists of three layers of Mu-metal with a thickness of 3 mm each. Furthermore, there is one additional layer of copper-plated aluminum (10 mm) for electromagnetic shielding. One Mu-metal layer consists of 5 plates with a thickness of 0.6 mm which are glued together. In order to preserve the large μ_r of the Mu-metal plates, mechanical stress has to be avoided. For this reason, a basic construction of aluminum profiles was designed which the Mu-metal plates can be attached to (see Appendix 8). It is not recommended to use ordinary screws to fix the Mu-metal plates due to the large local pressures. Using a wooden board that is screwed to the aluminum profile reduces the local pressure and still yields to a stable connection with a good magnetic contact. The screws are made from aluminum because stainless steel, for instance, produces too large magnetic fields. The edges of one Mu-metal layer are made of L-profiles which are bent before being annealed. By overlapping with both Mu-metal plates in each side a good magnetic contact is achieved as well.

As it is shown in Fig. (3.0.2), the inner volume of the MSR is accessible through a large door which can be opened and closed by hand. In order to achieve a good magnetic contact, the door is pushed with compressed air to the Mu-metal layers of the MSR. Due to changes in magnetic contact, the residual magnetic field within the MSR may also change. The advantage using this technique is that the pressure can be kept very constant in time and therefore the changes of the residual magnetic field within the MSR are minimized. Furthermore, there are several openings through which it is possible to interact with the experiment via optical-fiber cables.

3.1 Performance of the MSR

In order to evaluate the performance of the MSR, the inner residual magnetic field has to be measured. Furthermore, the shielding factors for different directions and different frequencies are of special interest. In the following section it is explained how these quantities are measured.

3.1.1 Measurement technique

There are multiple technologies to measure magnetic fields. The most common ones are listed in Fig. (3.1.1). The most sensitive sensor is the SQUID sensor. It is used in the experiment to resolve the precession of the overall magnetization of the ^{3}He/^{129}Xe gas mixture. For the characterization of the MSR, it was decided to use a fluxgate magnetometer. This type of sensor has a notable relative resolution below 0.1nT. Furthermore, they are much easier to operate than a SQUID sensor which provides more flexibility. Other sensors either have not a sufficient resolution or are too advanced concerning the operation.

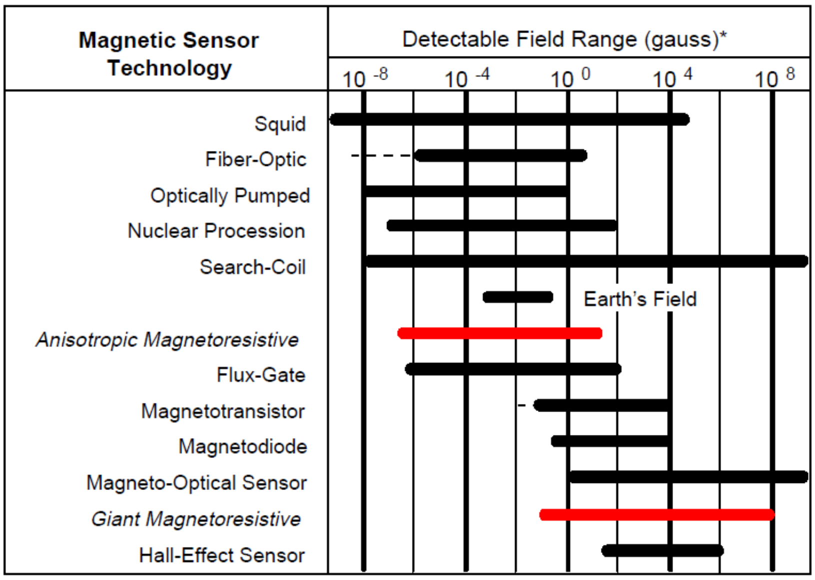

* Note: 1gauss = 10 $^{-4}$Tesla = 10 ^{5}gamma

Figure 3.1.1: Sensitivities for different types of magnetometers, source: [59].

The fluxgate sensors used are fabricated by Stefan Mayer Instruments (FLC3-70). With these sensors, it is possible to measure the magnetic fields in all three axes simultaneously. The magnitude of all field components is converted into a voltage signal. Six wires are connected to the sensor: V_{CC}, GND, three axes and $V_{\mathrm{ref}} = V_{\mathrm{CC}}/2$. These voltage signals are sampled by a differential delta-sigma analog-to-digital converter (ADC) with a resolution of 24 bits (ADS1299, Texas Instruments). The ADC is connected to an 8-bit microcontroller (ATxMega32, Atmel) performing the read-out of the ADC and the serial communication to a computer. The microcontroller is connected by two optical-fiber cables to the PC outside the MSR and is powered by a 50Ah car battery in order to reduce the noise level. Conventional coaxial cables cannot be used because they act as antenna transferring external noise into the inner volume of the MSR. Within the MSR, the six wires of the fluxgate are soldered to four coaxial cables which are connected to the ADC. This is essential because especially the V_{CC} and the GND line would form a conducting loop producing an additional magnetic field of several nT. This would not be acceptable when expecting a residual magnetic field at the same order of magnitude.

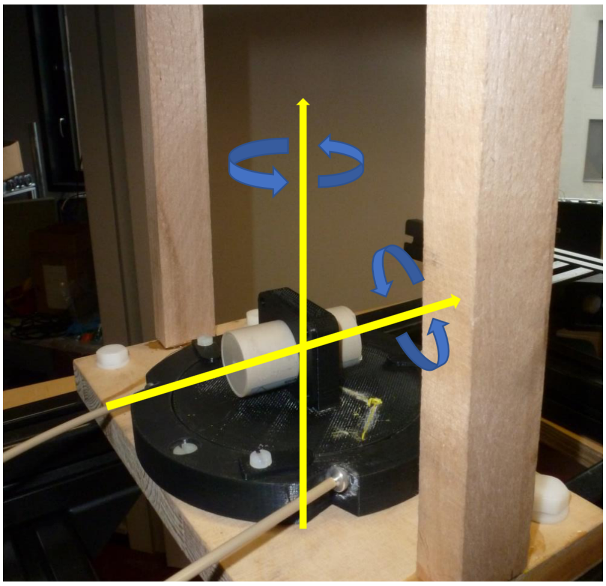

Figure 3.1.2: 3D-printed rotational platform with fluxgate sensor.

Unacceptable is also the large offset of the fluxgate sensor. It may range between 10 to 100 nT which is much larger than the quantity of interest. The only way to overcome this problem is to rotate the sensor by 180° along two axes. Then, the offsets can be eliminated: due to this rotation, the magnitude of the corresponding field component should not change but only the sign. At first glance, this principle sounds very easy, however its realization is not. First of all, it is desirable that the rotation is performed automatically. So, a rotational platform has to be constructed which can be controlled from outside the MSR. Additionally, this platform must not contain any magnetic parts for obvious reasons. In Fig. (3.1.2) the 3D-printed rotational platform is shown. It allows for a rotation of the sensor by 360° around the vertical axis and around the longitudinal axis of the sensor. With this setup all offsets can be deduced and subtracted. The rotation is controlled outside the MSR using two stepper motors and is transferred by stable strings which are running through very stiff plastic tubes forming a Bowden cable.

3.1.2 Residual magnetic field

In the first measurement, the sensor with the rotational platform is located at the center of the MSR. With the door closed, several rotations around the vertical and the longitudinal axis have been performed. The signals are shown in Fig. (3.1.3).

In this plot, the sensor offsets have already been subtracted. For the longitudinal rotation (green area) the z-axis does not change because it is aligned parallel to the axis of rotation. The other axes x and y have a phase shift of 90° as one may expect for a constant magnetic field. Rotating the sensor around the vertical axis, it can be observed

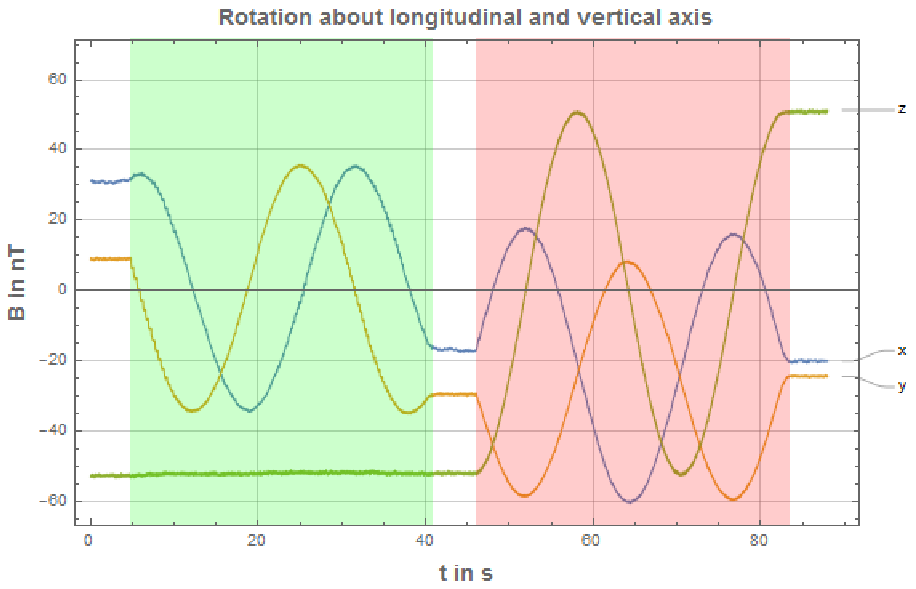

Figure 3.1.3: Signals for the rotation about longitudinal axis (green) and the vertical axis (red). The sensor offsets have already been subtracted.

that the z-axis gives the maximum amplitude due to its perpendicular orientation to the rotation axis. By adding the amplitudes of the x and y axis of the sensor quadratically, one obtains exactly the amplitude of the z sensor. The goal is to extract the absolute magnetic field at the center of the MSR. The strategy is to fit a sine wave simultaneously to all three signals of the horizontal rotation. The frequency and the phase are global fit parameters whereas the amplitudes and offsets were left free. For the z signal a phase shift of 90° is enforced within the fit model. From the z amplitude the horizontal component is already given. The vertical component is obtained by the offsets of the x and y signals which have to be added quadratically. To get the absolute magnetic field, the horizontal and the vertical components have to be added quadratically as well. The offsets of x and y, however, might contain sensor offsets which have to be subtracted. For this reason, an additional measurement is needed to isolate them. This is achieved by the rotation of the sensor about its longitudinal axis. Here, the same fit model was fitted to the data with the exception that the z amplitude was constrained to zero and the x and y amplitudes were enforced to be the same. Furthermore, the x and y signal are phase-shifted by 90° in the fit function.

$$S_x^H(t) = a_1^H \cos(\phi)\sin(2\pi f t) + a_1^H \sin(\phi)\cos(2\pi f t) + c_1^H \tag{3.1.1}$$

$$S_y^H(t) = a_2^H \cos(\phi)\sin(2\pi f t) + a_2^H \sin(\phi)\cos(2\pi f t) + c_2^H \tag{3.1.2}$$

$$S_z^H(t) = a_3^H \cos(\phi + 90°)\sin(2\pi f t) + a_3^H \sin(\phi + 90°)\cos(2\pi f t) + c_3^H \tag{3.1.3}$$

$$S_x^L(t) = a_1^L \cos(\phi)\sin(2\pi f t) + a_1^L \sin(\phi)\cos(2\pi f t) + c_1^L \tag{3.1.4}$$

$$S_y^L(t) = a_1^L \cos(\phi + 90°)\sin(2\pi f t) + a_1^L \sin(\phi + 90°)\cos(2\pi f t) + c_2^L \tag{3.1.5}$$

$$S_z^L(t) = c_3^L \tag{3.1.6}$$

$$|B| = \sqrt{(a_3^H)^2 + (c_1^H - c_1^L)^2 + (c_2^H - c_2^L)^2} \tag{3.1.7}$$

In this measurement shown in Fig. (3.1.3) the residual magnetic field can be estimated to roughly 60 nT. For the operation of the Helium-Xenon Experiment this value is too large. Problematic is not the magnitude of the magnetic field itself but the potential gradients might be too large. If the residual field was very small, then the gradients would not exceed a maximum value. For this reason, a dedicated degaussing procedure was developed in order to reduce the residual magnetic field within the MSR. The degaussing procedure will be presented in detail in the next section. However, before trying to minimize the residual field, it is important to understand the behavior of the sensor and the MSR. An interesting aspect is the drift of the sensor offset versus the drift of the residual magnetic field. Therefore, a measurement over several hours was performed rotating the sensor every two minutes.

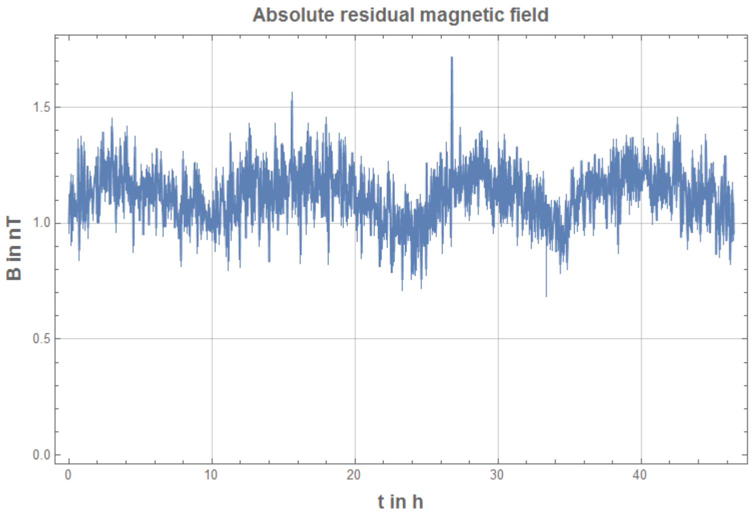

Figure 3.1.4: Drift of the absolute magnetic field at the center of the MSR.

The amplitude is obtained by the fit parameters according to equation (3.1.7). Fig. (3.1.4) shows a constant behavior at a twenty percent level of the absolute residual magnetic field after degaussing. It could be inferred that the absolute value stays in a regime of 1.2 ± 0.2 nT. The statistical resolution of a single data point, i.e. a single simultaneous fit is around 50 pT. This is much smaller than the actual drift of the field. It should be mentioned, that the absolute magnetic field published in the technical paper about the MSR is stated to be <1 nT. In this measurement, a different approach was chosen which might explain the different results [55]. In Fig. (3.1.4), three minima can be observed at 10 h, 24 h and 34 h. It is assumed that they are caused by temperature drifts which can affect both, the electronics and magnetic fields. Due to time constraints, these systematic effects have not been examined in full detail and therefore this result should be regarded as an upper bound of the residual magnetic field. Finally, the drifting sensor offset of the z axis is shown as an example in Fig. (3.1.5). Within ten hours it may change up to 1 nT. For the three axes of the sensor, the drifts may have a different trend but the time scales and the amplitudes are comparable.

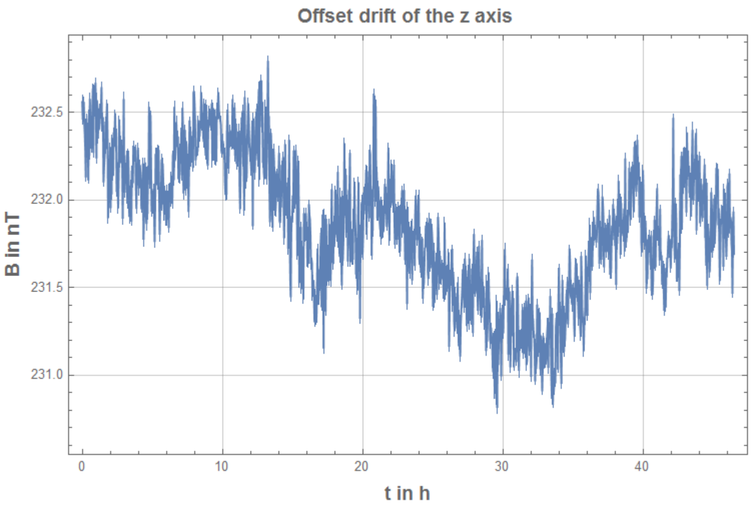

Figure 3.1.5: Drift of the sensor offset for a single axis.

3.1.3 Attenuation factors

For measurements within the MSR, it is also very important to shield external AC signals. Especially the frequency range covering the measurement signal originating from the polarized noble gases (5-15 Hz) is very critical. For this reason, the shielding behavior was examined systematically. In order to measure a shielding factor, a stimulus signal is needed. This is created by a Helmholtz-like coil pair which is located at the outer edges of the MSR. In this way, three pairs of coils are set up in x, y and z direction. The signals for the coils are produced by a function generator (DG4062, Rigol). Usually, a sinusoidal current with frequency f and amplitude A_0 was applied to the coils and amplified by a current amplifier (TOE 7621, Toellner). The quantity of interest is the amplitude of the magnetic field at the center of the coil pair and therefore of the MSR. It is measured using a fluxgate sensor described in the sections above. Here, no rotation is necessary, because the signal is already modulated and the sensor offsets do not contribute. On the other hand, this value can be simulated knowing the applied current and the geometry of the coil pairs. The Mu-metal layers of the MSR are ignored and threatened as air ($\mu_r = 1$). The ratio of these two values is defined to be the shielding factor:

$$S_{\mathrm{i}}(f) = \frac{B_{\mathrm{i,\ sim}}(f)}{B_{\mathrm{i,\ meas}}(f)} \tag{3.1.8}$$

where i is the x, y or the z axis and f the frequency. It should be noted that this definition is not consistent with other definitions used in theory. In [49] e.g. it is assumed, that the shielding factor is measured with an external homogenous field which is not the case for the present setup due to spatial constraints. An important measurement is the dependency of the shielding factor on the frequency. A typical behavior is shown in Fig. (3.1.6). In this plot the shielding in z direction is shown.

It can be observed that the shielding factor at low frequencies (<0.01 Hz) is nearly constant at the level of around 240. For larger frequencies the shielding factor quickly rises to values of more than 10^5. This is caused by the aluminum layer of the MSR which shields external magnetic fields due to eddy currents. For frequencies larger than 10 Hz it became very hard to measure any signal inside the MSR, because the shielding is getting too large. One aspect of concern may be the low shielding factor at low frequencies. The consequence is that slow drifts of the external magnetic field may affect the experiment.

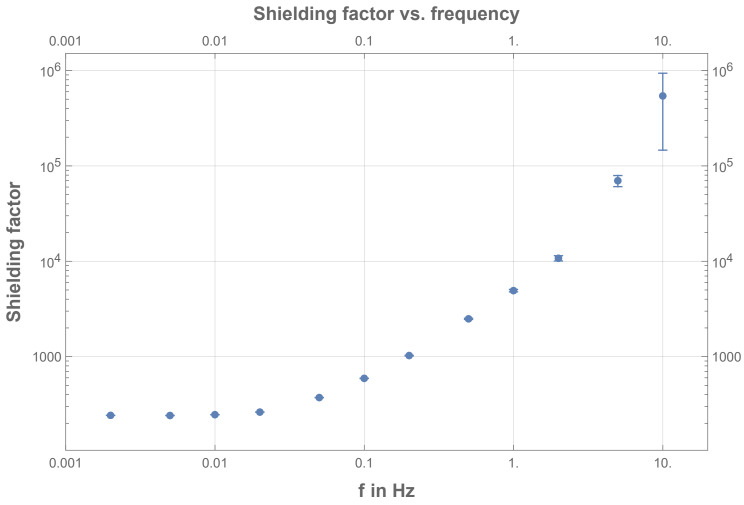

Figure 3.1.6: Frequency dependency of the shielding factor.

When it turns out to cause any problems, a system of compensation coils outside the MSR can be installed in order to reduce external drifts.

During the measurements of the shielding factors a new interesting fact was discovered which is not found in literature. The magnitude of the shielding factor depends significantly on the amplitude $B_{\mathrm{i,sim}}$ of the external magnetic field at fixed frequency. For example, at 20 mHz, in Fig. (3.1.7) it is shown that the shielding factor differs by a factor of 2 for different external amplitudes.

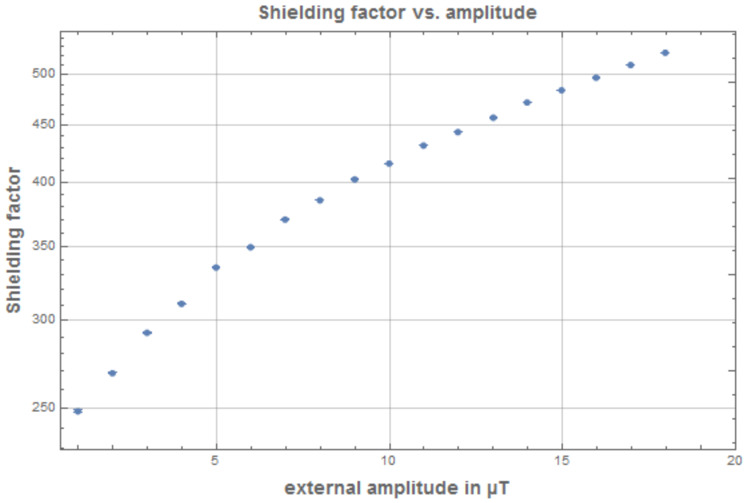

Figure 3.1.7: Amplitude dependency of the shielding factor for a constant frequency of 20 mHz.

3.2 A new way of degaussing

For measurements inside the MSR it is crucial to maintain the same conditions for different runs. Here, the most critical parameter is the magnetic field or, more correctly, the gradient of it. Furthermore, the magnetic field should be very stable in time during the experiment. Relaxation processes within the Mu-metal layers are the dominant source for drifts of the magnetic field. In order to reduce these drifts, the strategy is to minimize the remnant magnetization of the Mu-metal. The process of getting there is called degaussing. In the next section, the degaussing routine used for the MSR is presented.

3.2.1 Degaussing procedure

We start with a closed magnetic ring consisting of a material with a very large μ_r. In the case of the MSR this material is the Mu-metal where 4 sides of the cube are forming such a ring. Around this ring a stimulus coil is wound. The windings of the stimulus coil are equally distributed to the four edges. In total, 4 x 5 windings are used per ring. In Fig. (3.2.1), the stimulus coil is shown for a single ring only. Due to the geometry of the MSR, however, such a ring can be oriented in all three directions. Additionally, the MSR has three layers which means that there are in total nine rings.

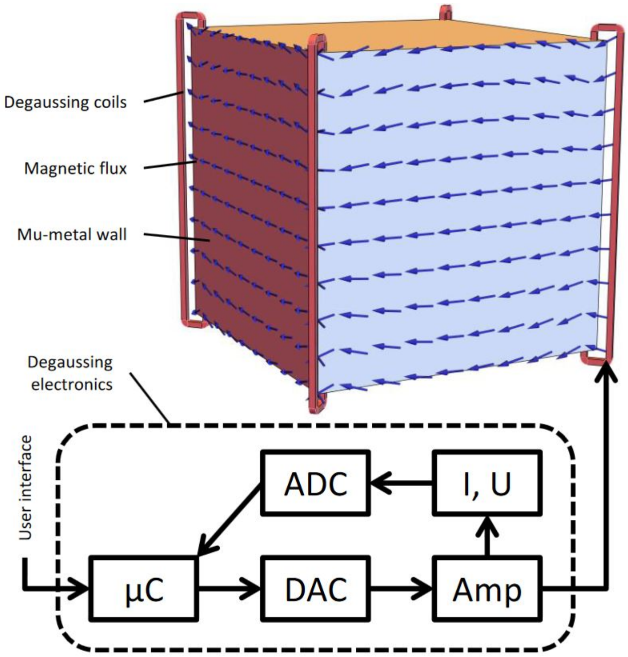

Figure 3.2.1: One of nine Mu-metal rings of the MSR with the stimulus coil. Source: [60].

To the stimulus coil, a sinusoidal current is applied which is translated into an oscillating magnetic field. If the magnetic field is large enough the Mu-metal will be saturated. This can be observed when measuring the hysteresis loop as shown in (3.2.2).

For small external magnetic fields like the Earth's magnetic field a large remnant magnetic field can be observed (in Fig. (3.2.2) at $H \approx 0$). Of course, the value of around 0.4 T is very large due to the large $\mu_r \approx 200000$. Dividing by μ_r, a magnetic field value next to the Mu-metal of several μT is obtained. At the center of the MSR this value drops significantly. Typical values which are measured when the MSR is not degaussed are in a range of 10-100 nT. This is already much smaller than the external Earth magnetic field of around 50 μT but the residual magnetic field can be reduced by a factor of around 100 by proper degaussing. The main goal must be therefore to remove the remnant magnetization of all parts of the Mu-metal. A common strategy to achieve this is to start with

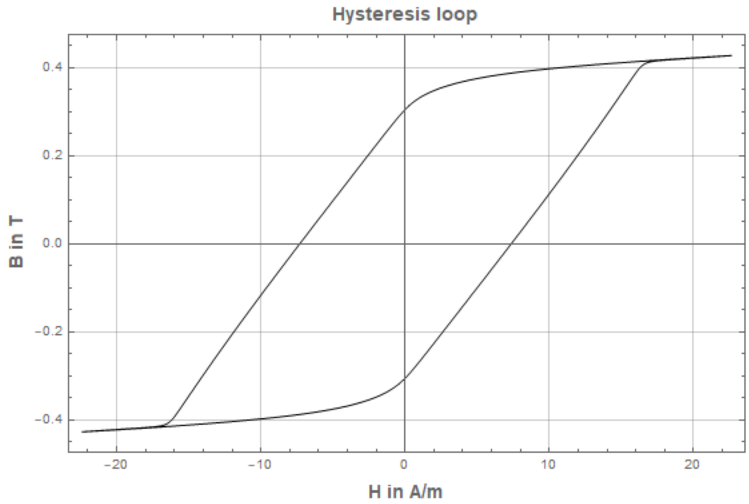

Figure 3.2.2: Hysteresis loop for very ferromagnetic materials.

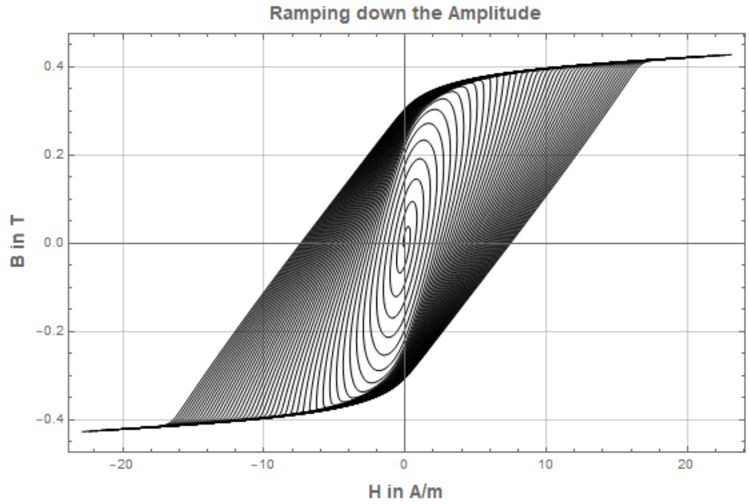

Figure 3.2.3: Behavior of the hysteresis loop when the amplitude is ramped down.

a large current amplitude such that the Mu-metal is well saturated. Then the amplitude is slowly decreased in time. It is recommended to ensure that two neighboring maxima may only differ by one percent [61]. The consequence of applying such a sequence to the stimulus coils can be observed in Fig. (3.2.3). By decreasing the external magnetic field, the remnant magnetization and therefore the magnetic flux of the Mu-metal reduces also. If there is no offset in the current signal of the degaussing coils, the curve will end up in the origin which means that the remnant magnetization is fully removed.

Based on this knowledge a special degaussing routine has been developed. In Fig. (3.2.4) it is shown that the routine consists of four phases. In the first phase (A), the current amplitude is ramped up linearly to a maximum value of 16 A. When the maximum amplitude was reached a few periods are applied in order to create a steady state condition such that the behavior of the Mu-metal is not dependent on its history anymore (B). A very special fact is that the starting frequency of 0.5 Hz is very small. This is not found in current literature and therefore this choice will be motivated in the next section. Next, the frequency is increased linearly at maximum amplitude (C). Finally, the amplitude decays exponentially, applying the rule stated above, that two neighboring maxima differ

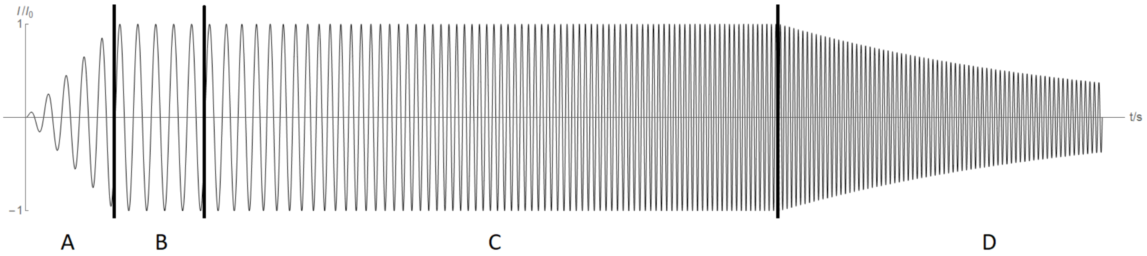

Figure 3.2.4: Degaussing routine developed for the MSR.

only by one percent (D). When optimizing the degaussing routine, the quality measure was the residual magnetic field at the center of the MSR and the execution time. The best results have been obtained when the frequency ramp was left out and when the exponential decay was performed at low frequency. At this point it has to be mentioned that the degaussing sequence shown in Fig. (3.2.4) has to be applied for three directions and for three layers. Therefore, the degaussing of the MSR (without frequency ramp) may take up to nine hours. For this reason, the frequency ramp was introduced in order to accelerate the exponential decay. By ramping the frequency from 0.5 Hz to 5 Hz the overall execution time of degaussing can be limited to around half an hour. So, this degaussing routine was chosen to be a suitable compromise between execution time and a good degaussing behavior.

3.2.2 Influence of offsets

The signal presented above was generated with a 20-bit digital-to-analog converter (DAC) which is connected to a microcontroller which samples the DAC values with a rate of 1 kHz. This allows to produce arbitrary waveforms and provides a high level of flexibility. One uncertainty of this realization of degaussing, however, may be offset errors. In Fig. (3.2.3) it was assumed, that the H field and therefore the current is offset-free. If this was not the case, the final point would not be the origin of the B-H plane but it would be slightly shifted in the H axis. Due to the large magnetic permeability of the Mu-metal a small change in H may result into a large change in B. In most applications, a transformer is used between the signal generation and the degaussing coils ensuring that all DC components are removed. In the setup used in Heidelberg, the degaussing coils are directly connected to the current amplifier without a transformer. Therefore, it is very important to examine the impact of the offset for degaussing. For this reason, several scans have been performed in which the offset was changed by purpose. One step consists of setting the offset to a defined value, degaussing the MSR, and waiting for one hour in order to measure the absolute residual magnetic field after degaussing using the rotational platform described before. In a first rough scan, the offset was varied by 1500 DAC bits per step. This is equivalent to a voltage change of about 9.5 mV. To relate this number, it should be mentioned that the maximum amplitude of the degaussing signal is 5 V which yields to a maximum current of 16 A. After the rough scan, a finer scan was performed around the minimum using a difference of 300 bits per step. In Fig. (3.2.5) the combination of both scans is shown. A clear minimum lying around 0 V can be observed. The fact that both scans which were recorded during two separate nights are matching very well shows that this result is highly reproducible.

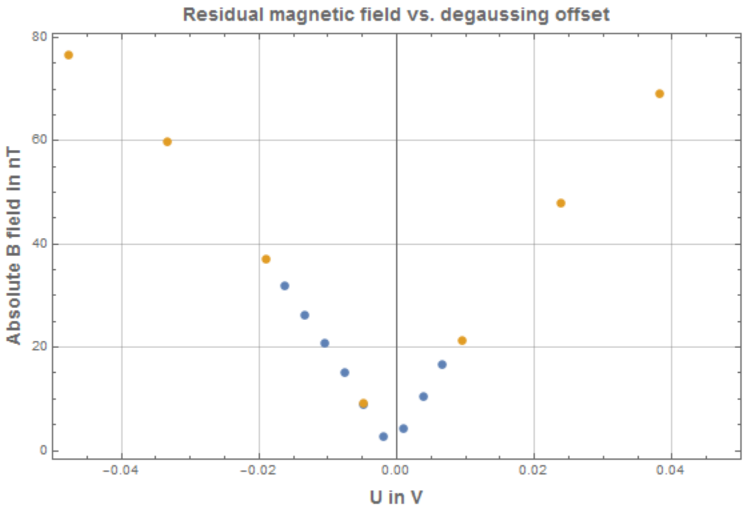

Figure 3.2.5: Dependence of the absolute residual magnetic field after degaussing when changing the offset, (orange: rough scan, blue: detailed scan).

Unfortunately, the conditions during this measurement were not perfect. Firstly, the SQUID system was already installed within the MSR. So, the measured magnetic field may also have some contributions originating from the SQUID system which are hard to isolate. Furthermore, the rotational platform could not be operated in the center of the MSR also due to the SQUID system. But all in all, it could be shown, nevertheless, that the offsets are under control and that they are not critical for the existing degaussing setup.

3.2.3 Toy model motivating the degaussing routine

The ability to saturate the Mu-metal is an important requirement in order to perform an optimal degaussing. The most relevant component for this is the current amplifier because the external magnetic field H is proportional to the applied current. According to Ampere's law the maximum current amplitude of 16 A allows for a maximum magnetic field of

$$H(\text{I=16 A}) = \frac{N \cdot I}{l_B} = \frac{20 \cdot 16\ \text{A}}{4 \cdot 3\ \text{m}} = 26.7\ \text{A/m} \quad . \tag{3.2.1}$$

Here, N is the number of windings for the stimulus coils per ring and l_B the path length of the closed magnetic ring. With this magnetic field it has to be possible to fully saturate the Mu-metal layers. Otherwise, a new current amplifier has to be taken into consideration. The saturation behavior of a certain material can be nicely observed by measuring its hysteresis loop. On the other hand, however, it is not clear how the saturation behaves within the material. It is desirable that every part of the Mu-metal layer is saturated and not just the outer parts of it.

For a theoretical description of the saturation behavior for a certain material within an oscillating external magnetic field the following classical model was constructed. We start with a Mu-metal plate with an expansion of 3m x 3m and a thickness of 2b = 3 mm.

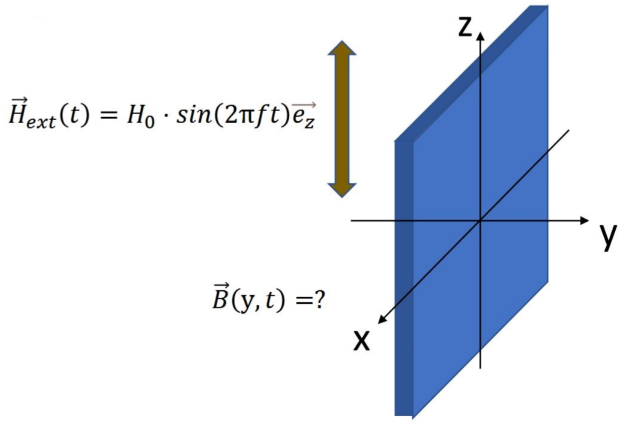

Figure 3.2.6: Orientation of the Mu-metal plate.

It is oriented as shown in Fig. (3.2.6). The external magnetic field is assumed to be homogeneous in space and sinusoidal in time:

$$\vec{H}_{\text{ext}}(\vec{x},t) = H_0 \sin(2\pi f t)\vec{e}_z \quad . \tag{3.2.2}$$

The goal is to find out how the external magnetic field is distorted and shielded by eddy currents within the Mu-metal plate. This is a purely classical problem and can be principally solved by Maxwells's equations. Due to the low timescale of this problem (for f < 50Hz, $c/f \gg 2b$), it is justified to use the quasi-static limit of the Maxwell equations [49]:

$$\nabla \times \vec{H} = \vec{j} \tag{3.2.3}$$
$$\nabla \times \vec{E} = -\partial_t \vec{B} \tag{3.2.4}$$
$$\nabla \cdot \vec{B} = 0 \tag{3.2.5}$$
$$\vec{j} = \sigma \vec{E} \tag{3.2.6}$$

where σ is the electric conductivity of the Mu-metal and $\vec{j}$ the induced current density. By taking the curl of the first equation we obtain

$$\nabla \times \nabla \times \vec{H} = \nabla \times \vec{j} \tag{3.2.7}$$
$$\nabla\nabla \cdot \vec{H} - \Delta\vec{H} = -\sigma\partial_t\vec{B} \tag{3.2.8}$$
$$\nabla\nabla \cdot \vec{H} - \Delta\vec{H} = -\sigma\partial_t\vec{B}(\vec{H}) \quad . \tag{3.2.9}$$

At this point it is very important to note that μ_r depends significantly on the external magnetic field $\vec{H}$. Instead of $B = \mu_0\mu_r H$ we have

$$\frac{\partial B}{\partial H} = \mu_0\mu_r(H) \tag{3.2.10}$$

or

$$B(H) = \mu_0 \int \mu_r(H) dH \quad . \tag{3.2.11}$$

This fact is encountered by defining the dependency of B and H empirically. Looking at the hysteresis curve in Fig. (3.2.2) it would be suggestive to choose a parametrization for B like

$$B(H) = \frac{2\alpha}{\pi} \arctan(\beta H) \quad . \tag{3.2.12}$$

With this B-function (as it is called in the following) a partial differential equation in $\vec{H}$ is obtained. Before solving this equation, it is worth mentioning that the expansion of the Mu-metal is much larger than its thickness. Therefore, it is natural to restrict the problem to one dimension (which is the y axis) for geometrical reasons. When restricting the partial differential equation to the y axis, the following rules apply: $H_x = H_y = \partial_x H_i = \partial_z H_i = 0$. What remains is

$$\partial_y^2 H_z(y,t) = \sigma(\partial_t H_z(y,t)) B'(H_z(y,t)) \tag{3.2.13}$$

where the prime denotes the derivative of B with respect to its argument. This equation has to be solved for the interior of the Mu-metal plate which means that $(y,t) \in [-b,b] \times [0,t_0]$. The boundary condition is provided by the external magnetic field $H_z(-b,t) = H_z(b,t) = H_{\text{ext, z}}(t)$ and the initial condition is chosen to be $H_z(y,0) = 0$. This gives a well-defined initial boundary problem and can be solved numerically.

Due to the choice of the B-function, the partial differential equation is highly nonlinear. That is the reason why even numerical solvers might have problems to find the correct solution of this equation. The standard approach to solve nonlinear partial differential equations is the use of finite-element-methods solvers (short: FEM solver). In this case the FEM solver of Mathematica (Version 12.1) has proven to be very efficient. The function "NDSolve[ ]" takes an expression of the differential equation and for the boundary conditions. Optionally, a user-defined mesh can be generated and passed to the solver. This turned out to be very helpful because a standard mesh did not work very well. The standard mesh was a triangular mesh where the mesh points were chosen without any pattern. Here the trick was to generate a rectangular mesh with equidistant mesh points in the y and the t direction. Typically, the y domain [-b,b] was divided into 200 and the t domain [0, t_0] into 5000 steps. An open question was how to choose the maximum time t_0. The boundary conditions are showing a periodical behavior in time. So, it is assumed that the solution will also show this kind of periodicity. By starting with an arbitrary initial condition, however, it is not likely that it will be reached again one period later. This is why a relaxation of the solution is expected until an equilibrium is reached when the solution is nearly perfectly periodic. Such a relaxation process is observed within the first two periods. After around 3 periods it disappeared. For this reason t_0 was chosen to be as long as five periods. The first four periods are thrown away and the last period was further examined.

3.2.4 Validation of the toy model at a mockup

In order to test the model presented above a simple mockup was built up. Around a hollow Mu-metal cylinder a stimulus coil and a pickup coil were wound with 20 windings each.

The wall thickness of the cylinder is 1 mm, the length 200 mm and its inner diameter is 82 mm. The stimulus coil is connected again to a Toellner-current amplifier which amplifies the signal originating from a Rigol function generator. In most measurements an ordinary sine wave was applied to the stimulus coil. The induced voltage of the pickup coil and the voltage signal of the current monitor of the Toellner amplifier were sampled with an 18-bit ADC converter (RedLab-1808X, Meilhaus Electronic). Depending on the frequency of the applied sine wave the sampling rate was chosen to be 1 kHz or 10 kHz.

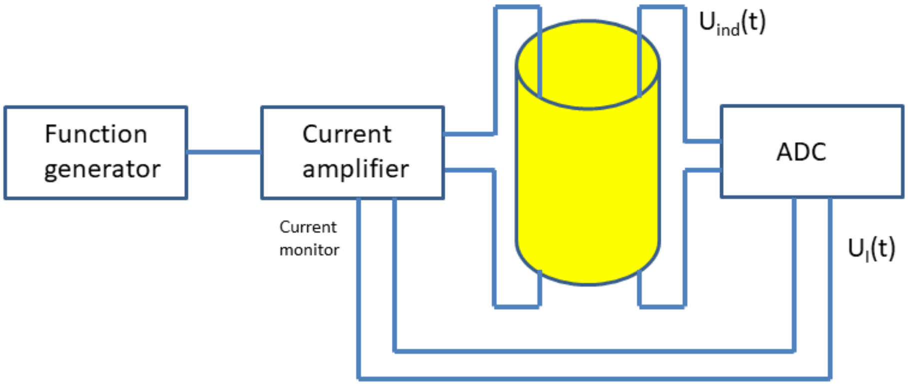

Figure 3.2.7: Setup of the mockup for testing the theoretical model.

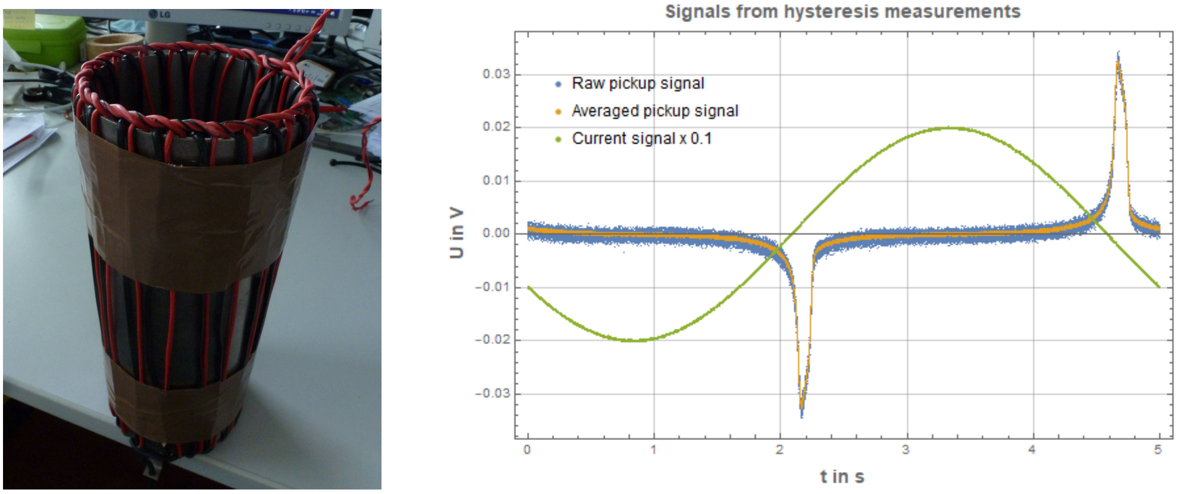

Figure 3.2.8: Left: Used Mu-metal cylinder with its pickup coil (red) and stimulus coil (black), right: measured signals for the determination of the hysteresis loop, note that the current monitor signal was divided by 10 for visualization reasons.

By applying a sinusoidal current to the stimulus coil a periodic B field is generated. Therefore, a voltage signal is induced at the pickup coil:

$$U_{\text{ind}}(t) = -n\dot{\Phi}(t) = -nA\dot{B}(t) \quad . \tag{3.2.14}$$

This induced voltage and the signal of the current monitor is shown in Fig. (3.2.8). Already at this point it can be concluded that the Mu-metal nearly completely saturated as there are flat regions at zero voltage showing that the B field does not change in time and therefore not in H. Due to the high noise level of the pickup signal it turned out to be beneficial to average the signal over a few periods. The average is also shown in the plot. To deduce the signal of the magnetic flux $B(t)$, equation(3.2.14) has to be integrated in time:

$$B(t) = \int_{t_0}^{t} \frac{U_{\text{ind}}(t')}{nA} dt' \quad . \tag{3.2.15}$$

In reality, the sampling points of the pickup signals are just summed. Due to the large sampling rate of 10 kHz and the low frequencies of the signals (0.1-10 Hz) the numerical error is negligible. An important aspect doing the integration is the offset. If there were a small offset in the pickup data $U_{\text{ind}}(t)$, the integrated signal would drift linearly. Therefore, offsets are removed by regarding exactly one period and subtracting the mean of it. In this way it is ensured that the B field signal starts and stops at the same value for one period such that the hysteresis loop is closed. In Fig. (3.2.9) the integrated B field signal of the pickup signal shown in Fig. (3.2.8) is depicted. To get to the hysteresis loop, the current signal has to be converted into a magnetic field H. This is done using Ampere's law (compare with equation (3.2.1)):

$$H(I) = \frac{nI}{l_B} = \frac{20}{\pi \cdot 0.0825m} I = \frac{123.5}{m} I \quad . \tag{3.2.16}$$

It is worth to mention that the current monitor of the Toellner amplifier converts the output current with a factor of $8A/5V$ in to a voltage signal. This factor has also to be taken into account when calculating the H field. Having determined the H field and the B field signals for one period it is now possible to draw the hysteresis curve by plotting the B field against the H field. The result is shown in Fig. (3.2.9).

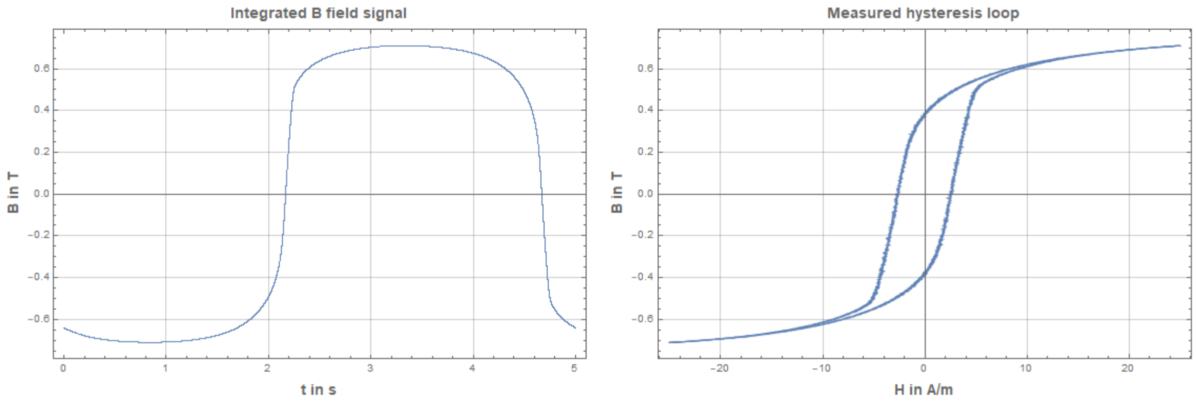

Figure 3.2.9: Left: integrated B field signal, right: obtained hysteresis loop from measured signal shown in Fig. (3.2.8)

With this procedure several measurements have been performed, changing both amplitude and frequency. In Fig. (3.2.10) a sweep of different frequencies at large H fields is shown. In this context, large means that the H field is much larger than 25 A/m which will be reached with the setup of the MSR. The chosen frequencies are 0.1 Hz, 0.2 Hz, 0.5 Hz, 1 Hz, 2 Hz, 5 Hz, 10 Hz, 20 Hz, 50 Hz, 100 Hz.

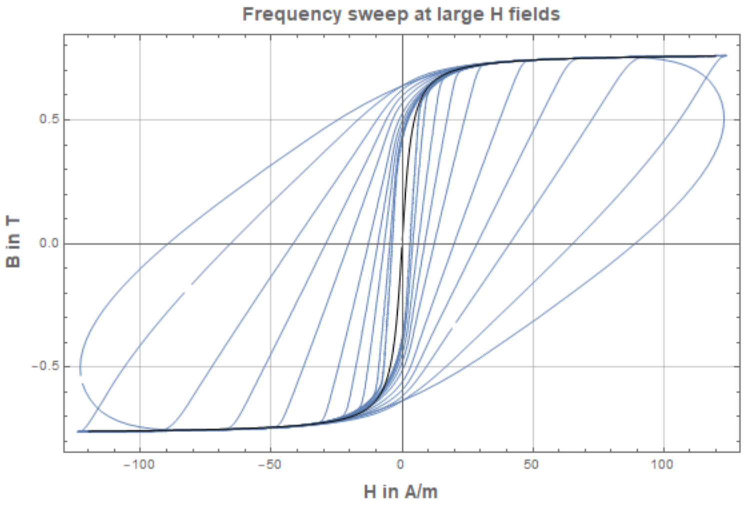

Figure 3.2.10: Frequency sweep for large external H fields. The innermost hysteresis loop was recorded at 100 mHz the outermost at 100 Hz. In black the chosen B-function is also drawn.

In this plot several observations can be made. First of all, there is a nice saturation at a B field of 0.77 T. This value depends on the composition of the Mu-metal and changes for different alloys. Furthermore, it can be inferred that the hysteresis of the loops increases with frequency. At very large frequencies (≈ 100 Hz) the hysteresis loops are merging into ellipsoids. To understand this behavior the theoretical model described above can be applied to the Mu-metal cylinder. First of all, the B-function has to be determined. Regarding Fig. (3.2.10), a natural parametrization of the B-function would be an Arctan function:

$$B(H) = \frac{2\alpha}{\pi} \arctan(\beta H) \tag{3.2.17}$$

where α is the B field at saturation which is here 0.77 T. The slope in the origin parametrized by β was adjusted according to the slope of the innermost hysteresis loops. Therefore, a value of 0.35 m/A was chosen for β. The obtained B-Function is also drawn in black in Fig. (3.2.10). The last parameter needed in order to solve the partial differential equation (3.2.13) is the electrical conductivity σ. The value of σ is not easy to determine because it changes for different alloys so there is no standard literature value. Measurements of σ are also complicated as the geometry of the sample has to be taken into account. For this reason the value of σ has been manually adapted such that the theoretical results describe the measurements best.

Having solved the partial differential equation (3.2.13) the magnetic field $H_z(y,t)$ is now known. It can be converted into $B_z(y,t)$ by plugging the values into the B-function. By integrating out the spatial dependency, the magnetic field signal seen by the pickup coils can be calculated:

$$B(t) = \frac{1}{2b} \int_{-b}^{b} B(H_z(y,t))dy \quad . \tag{3.2.18}$$

Together with the external H field which was chosen to be a sine wave the theoretical hysteresis loop can be drawn. By comparing the measurements in Fig. (3.2.10) with the theoretical results the following matching can be achieved.

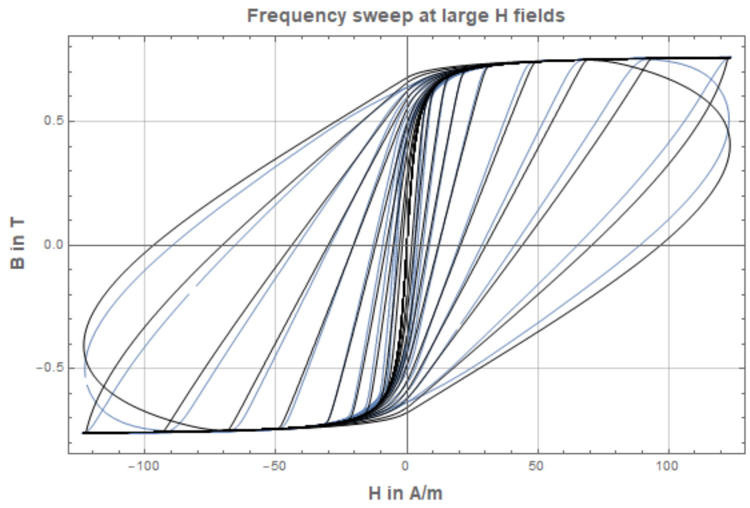

Figure 3.2.11: Comparison of the measurements (blue) and the simulations (black).

Fig. (3.2.11) shows a nice agreement between the measurements and the theoretical model. The same measurement was repeated with lower H field values of 25 A/m which corresponds roughly to the value reached during the degaussing of the MSR. In Fig. (3.2.12) still a nice matching between measurements and theory can be recognized but for smaller frequencies at low H fields small deviations are observed. This might be explained by an improper choice of the B-function. Comparing the slope at the origin with the slopes of the innermost hysteresis loops the B function should be steeper. But in this case, the parametrization with the Arctan function would have failed and a more complicated function would have been needed. Finally, three measurements in which the amplitude was ramped at fixed frequency are presented in Figs. (3.2.13) - (3.2.15):

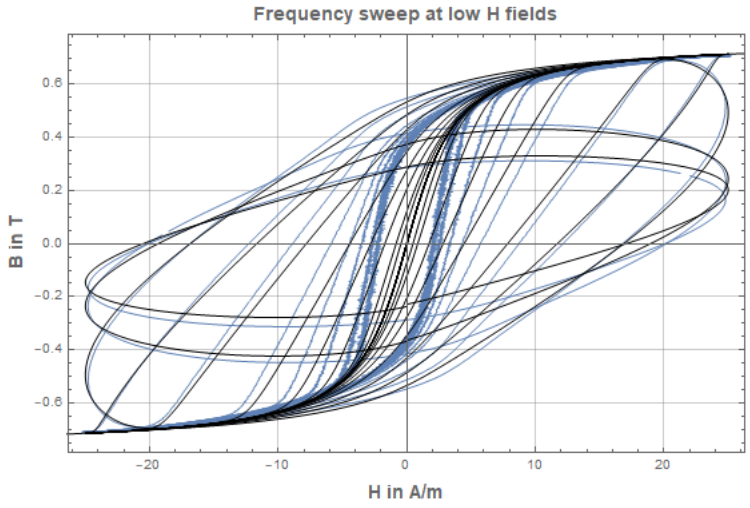

Figure 3.2.12: Comparison of the measurements (blue) and the simulations (black).

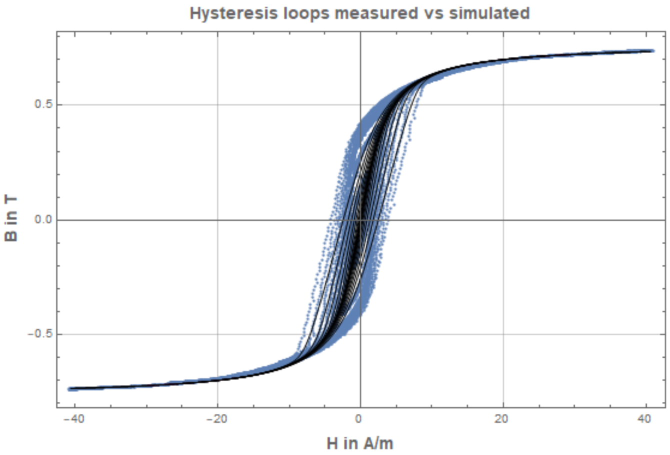

Figure 3.2.13: Amplitude sweep at 0.5 Hz.

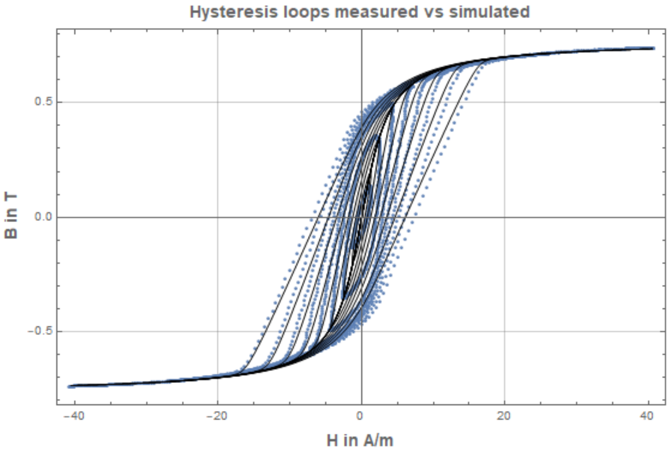

Figure 3.2.14: Amplitude sweep at 2 Hz.

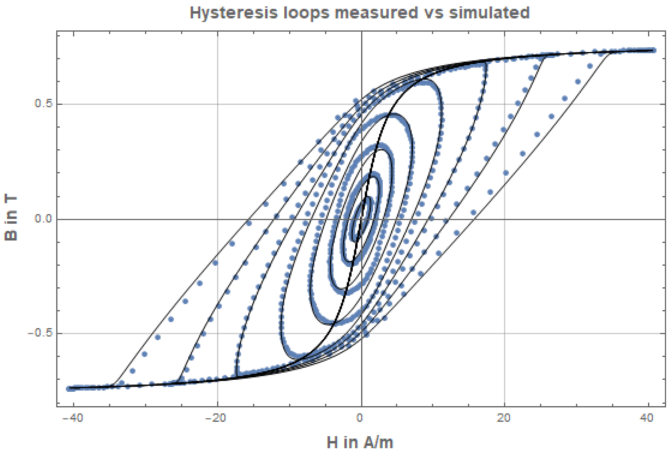

Figure 3.2.15: Amplitude sweep at 10 Hz.

In Figs. (3.2.13) - (3.2.15) the agreement between data and theory becomes better with increasing frequency. One reason for this might be that eddy currents increase with frequency and therefore become more important describing the shape of the hysteresis loops.

It should be noted that for all measurements which are presented above a conductivity of $\sigma = 2.1 \times 10^6\ \Omega^{-1} m^{-1}$ was assumed. Together with α, β defining the B-function, the thickness $2b$ and the external H field amplitude H_0 only five parameters in total are needed in order to describe the shape of the hysteresis loops in Mu-metal. Regarding possible deviations of this model, it should be mentioned that the B-function was just an approximation and has to be determined empirically. Furthermore, the expansion of the Mu-metal cylinder is still finite. So, the approximation in one dimension might also have limits. All in all, it could be shown that hysteresis loops in Mu-metal can be described by classical effects which are the existence of eddy currents.

The big advantage of this model is that the spatial dependency is also accessible. Regarding external magnetic fields of $H_0 \approx 25$ A/m, the low-frequency and large-frequency case can be compared:

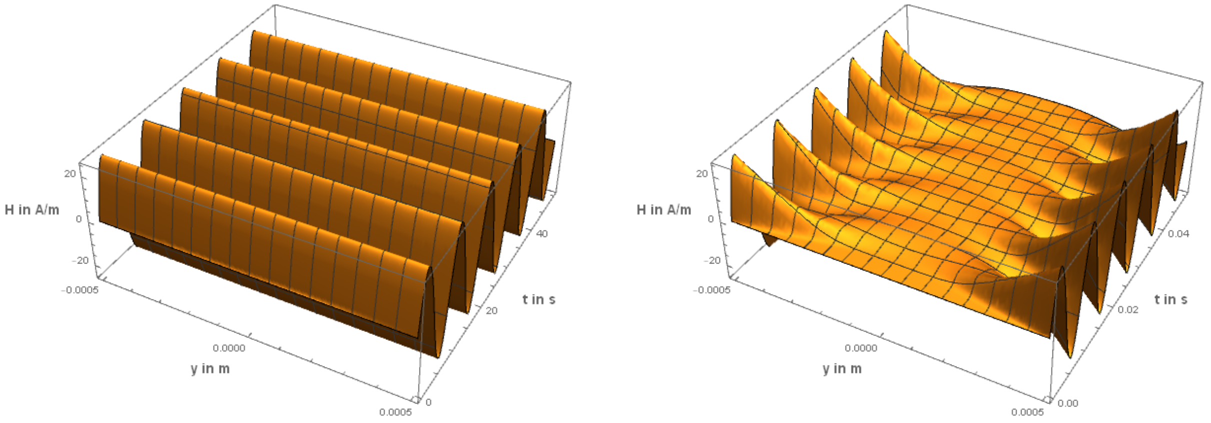

Figure 3.2.16: H field in space and time for a frequency of 0.1 Hz (left) and for 100 Hz (right).

In both plots the sinusoidal boundary conditions can be easily discovered. In y direction the spatial dependency across the thickness of the Mu-metal layer is shown. For low frequencies, it can be observed that the external H field fully penetrates into the Mu-metal and is not shielded or distorted. In the opposite case of large frequencies, however, the external H field is nearly shielded completely in the middle of the Mu-metal (at y=0) and a distortion due to eddy currents can be observed.

This result already explains why a very low frequency was chosen for the degaussing procedure. Degaussing the MSR, it is important to ensure that the whole Mu-metal layers are fully saturated. This can be achieved when eddy currents do not become too large. In the next section the introduced model will be applied to the MSR and compared with measurements.

3.2.5 Application of the toy model to the MSR

In principle, the setup remains the same as before (see Fig. (3.2.7)). For the MSR the same type of current amplifier (TOE7621, Toellner) was chosen allowing for a maximum current of 16 A. Instead of the Mu-metal cylinder the outer Mu-metal layer of the MSR was tested. The ring, consisting of four sides of the outer cube, was chosen such that the door of the MSR is not included. A pickup coil was added by pushing a cable with 10 wires through the outer ring. The wires are connected to each other ensuring that 10 windings are obtained.

For the simulation the thickness, the electrical conductivity σ and the B-function of the Mu-metal alloy have to be changed. For the first parameter, a thickness of 3 mm was assumed. The B-function and σ have to be extracted again from a measurement. According to the results of the previous section the hysteresis of the loops becomes smaller with frequency. Therefore, a measurement at a very low frequency of 0.5 mHz was performed. As a side mark, the period of this signal corresponds to roughly 30 minutes. In order to achieve sufficient statistics, the measurement took several hours. In Fig. (3.2.17) the result is presented. First of all, a nice saturation behavior can be observed. In the case of the MSR, the saturation already occurs at B-field values of roughly 0.4 T. Due to the low frequency, eddy currents are significantly reduced. The consequence is that the hysteresis becomes very narrow. Therefore, it is easy to guess the form of the B-function needed for further simulations:

$$B(H) = \frac{2\alpha}{\pi} \arctan(\beta H) + \gamma H \quad . \tag{3.2.19}$$

Here, a different parametrization was used by adding a phenomenological, linear term in H. The parameters are $\alpha = 0.4$ T, $\beta = 1.26$ m/A and $\gamma = 0.0016$ Tm/A.

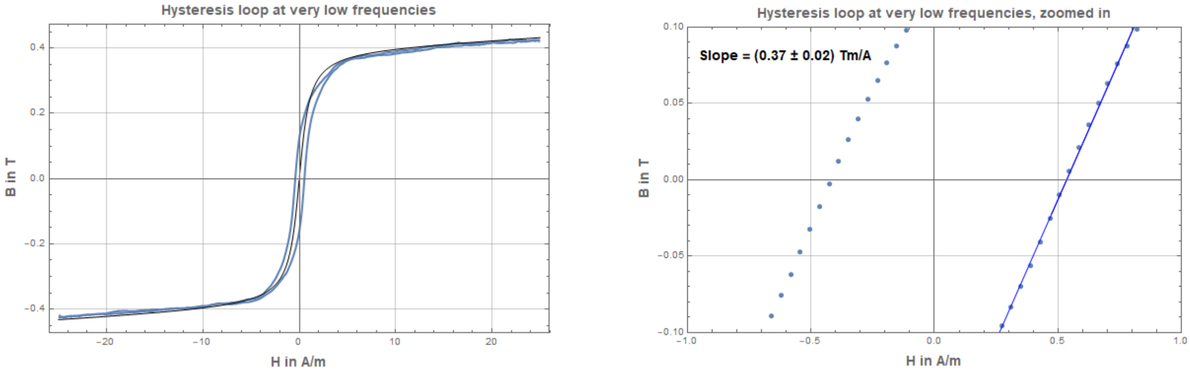

Figure 3.2.17: Hysteresis loop measured at very low frequency at the MSR with the B-function used for further simulations(left), and a zoom into the origin (right).

Finally, one more interesting fact could be discovered. Zooming into the origin of the measured hysteresis loop, the slope m at the steepest points can be extracted by a linear fit. The determined number can be converted into a value for the maximum μ_r:

$$\mu_r = \frac{1}{\mu_0} \cdot \frac{\partial B}{\partial H} = \frac{m}{\mu_0} = 294000 \pm 16000 \quad . \tag{3.2.20}$$

This is an important check of quality for the MSR. For Mu-metal as such, it is not surprising that a very large μ_r can be measured. But it should be noted that the layers of the MSR are consisting of many different parts assembled together. So, it is not obvious that the overall μ_r remains so large. Mu-metal plates are very sensitive to mechanical pressure or even to deformation. In this case μ_r will drop remarkably and the magnetic shielding is lost. On the other hand, however, to obtain a large overall μ_r for a ring, the magnetic contact between two Mu-metal plates has to be also large enough which requires a minimum pressure applied to the plates. For this reason, the transport and also the assembly is very demanding. The result found above shows that (at least the outer layer) is very well manufactured and assembled.

In the following, further measurements are presented and compared to the simulation. In Fig. (3.2.18) a frequency sweep was measured at maximum amplitude of around 25 A/m. The frequencies were the same as in Fig. (3.2.10) stopping however at 10 Hz. With this measurement the conductivity could be estimated to $(1.23 \pm 0.01) \times 10^6\ \Omega^{-1} m^{-1}$. The error was obtained by trying different values of σ for the simulation. Regarding the hysteresis of the simulated loops, they are very sensitive to σ. This is due to the fact that the hysteresis depends mainly on eddy currents. By changing σ it is possible to tune how much eddy currents may contribute within simulations. Furthermore, it becomes clear why the ellipsoids are observed at much lower frequencies than before using the cylinder. At the MSR the transition of the curved into ellipsoids already starts at 5 Hz. For the cylinder this transition starts at roughly 20 Hz (see Fig. (3.2.12)). This can be explained by the thickness of the Mu-metal plates. At the MSR the thickness is three times larger than at the cylinder which means that the external magnetic field has to penetrate much deeper into the Mu-metal. Therefore, the shielding becomes much better and the situation shown in Fig. (3.2.16) for 100 Hz is more likely reached which results in elliptical-shaped loops.

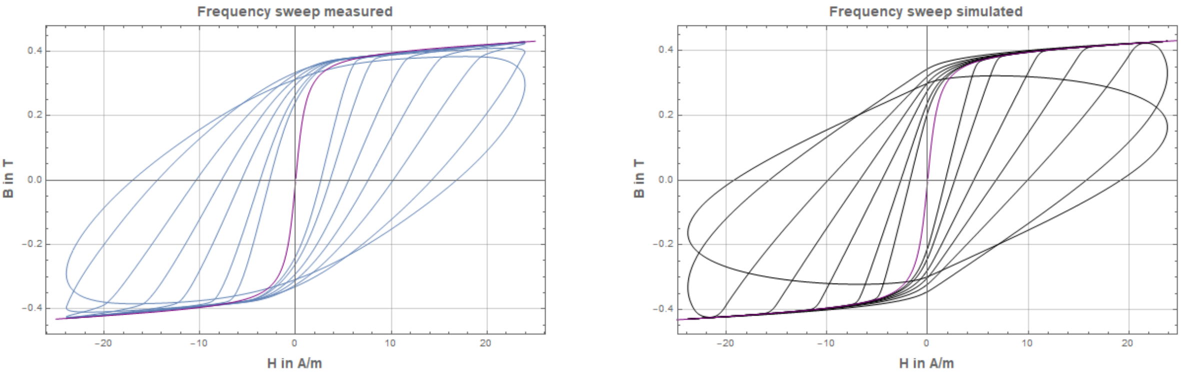

Figure 3.2.18: Frequency sweep measured at the MSR (left) and the corresponding simulations (right).

Finally, a combined plot is shown in which three frequencies are picked and simulations and measurements are compared. In case of the MSR, the agreement between theory and experiments is much worse than for the cylinder.

Looking at Fig. (3.2.19) the measured hysteresis loops are at least described qualitatively by the model. It should be emphasized again that the model presented is very simple and therefore very idealistic. Especially the 1d approximation will have certain limits. Taking a closer look to the Mu-metal layers it can be noticed that there are several overlapping regions ensuring a good magnetic contact along the Mu-metal rings. This has the consequence that the thickness may be twice as large in some regions which is not taken into account for the simulation. Comparing this situation with the cylinder the cylinder has a much more homogeneous geometry and the model gives a better agreement.

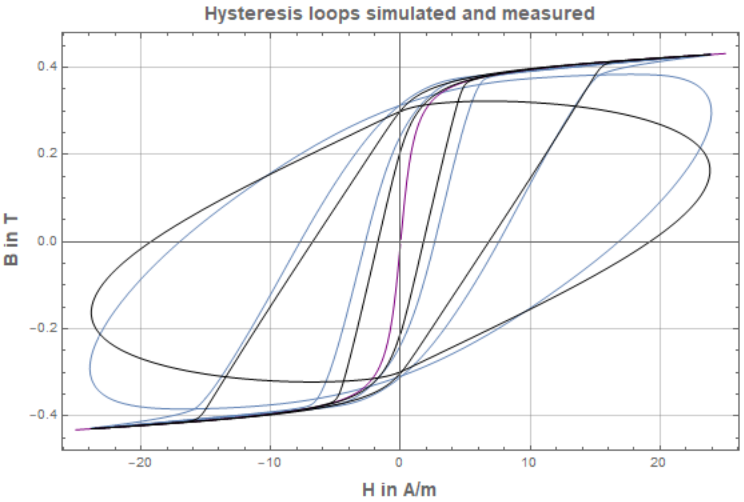

Figure 3.2.19: Hysteresis loops at 0.1 Hz, 1 Hz and 10 Hz simulated (black) and measured (blue) at the MSR.

Nevertheless, the model can still be used to motivate the degaussing routine chosen for the MSR. Especially the fact could be proven that low frequencies should be used because eddy currents are shielding external magnetic fields preventing the whole Mu-metal layer to be saturated.

Chapter 4

The Xenon Polarizer

In this chapter the commissioning and the adaptation of the xenon-polarizer system is presented. In a first part, the setup is introduced and it is described which changes have been made. In a second part, the functionality of the polarizer is verified and its performance is demonstrated.

4.1 Setup and components

The following setup was mainly constructed by Prof. Dr. Werner Heil at the Johannes-Gutenberg-Universität in Mainz using components of a previous version of xenon polarizer. The setup which is presented in the following is based on the former xenon polarizer which is described in full detail in [62].

4.1.1 Vacuum system

For the xenon polarizer it is crucial, that several requirements are fulfilled. The first one is that no oxygen has the opportunity to enter the system for two reasons: Firstly, oxygen reduces the relaxation time of polarized xenon significantly and, secondly, it would oxidize the rubidium, which is located in the optical pumping cell. Therefore, the vacuum system has to be leak-proof. An additional aspect is the magnetic field. Once the xenon gas is polarized, it should be ensured, that the relaxation time is not too short due to magnetic field gradients. For this reason, it is not recommended to use pipes or connections consisting of e.g. stainless steel. Before the gas mixture enters the optical pumping cell, this is not critical. But after leaving it, it is. For this reason, only parts consisting of glass or plastic are used. In Fig. (4.1.1) the overall setup is depicted. The valves are labeled uniquely and their labels will be consistently used throughout this thesis. All parts contained in this sketch will be introduced within the next sections.

4.1.2 Gas mixing unit

As a starting point of the overall setup, the gas mixture has to be produced. ^{4}He and N_2 are used as buffer gases and xenon as the gas to be polarized. In order to obtain a specific mixture of these gas components, three mass flow controllers (F-201C-RAA-33-V, Bronkhorst) are used. Their principle of working is based on heat capacity measurements of the flowing gas. Due to different heat capacities for different gases, the mass flow controllers have to be calibrated for a specific gas or a defined mixture. Via a digital interface the nominal value for the flow can be set, and the actual (measured) flow can be

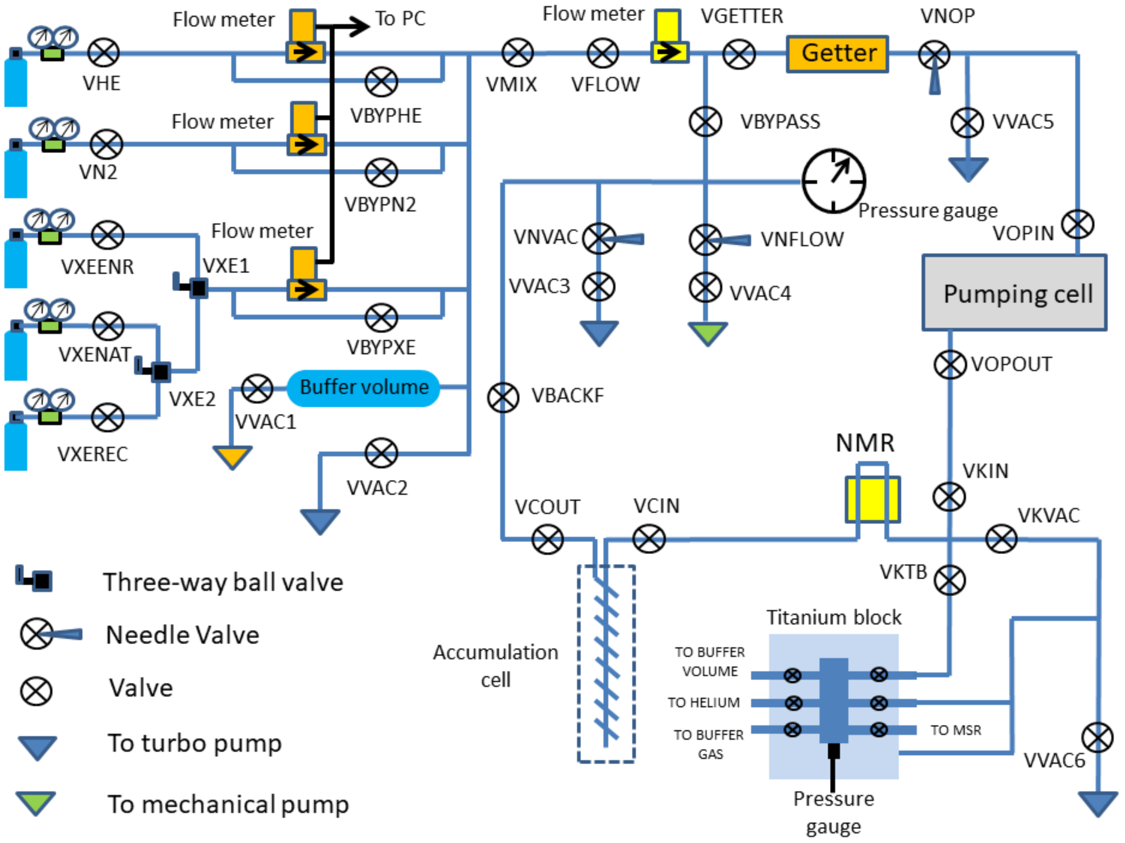

Figure 4.1.1: Sketch of the overall vacuum system containing the gas mixing unit, the titanium block, the optical pumping cell, the NMR monitor and the accumulation cell.

read. Before passing the flow controllers, the gases are stored in gas tanks of ultra-high purity. With a pressure reducer for each tank the initial pressure is reduced to 5 bar. The outlets of the flow controllers are combined to one line containing the desired gas mixture. This line is fed into another flow meter calibrated to a standard gas mixture of 1% Xe, 8% N_2 and 91% ^{4}He, which is used throughout this thesis if not otherwise noted. The additional flow meter was inserted for practical reasons only in order to have access to the overall flow in real time via an LCD display. Finishing the preparation of the gas mixture, a getter (GPUS300F-IX-04R00CA, Entegris) was included ensuring that no oxygen and other impurities can enter the optical pumping cell. For the xenon-gas supply, three options can be chosen. For general testing, a gas tank of natural xenon is attached. A tank containing enriched ^{129}Xe can be used for production runs, e.g. EDM measurements. Due to the high cost of enriched xenon gas, it should be recovered after a measurement. The corresponding recovery system will be presented later. The third option is the use of recovered xenon gas.

4.1.3 Optical pumping cell

Within the optical pumping cell, the polarization of xenon will take place. For choosing the proper material for this cell, several requirements must be fulfilled. The temperatures while polarizing may range between 100-200°C and the pressure of the gas mixture may change from 0 to 2 bar. Furthermore, the material must not absorb too much of the incident laser light nor change its circular polarization. Due to the fact that rubidium is involved within the polarization process, the material should be chemically inert. For these reasons, it is a common choice to construct the oven out of glass. In the present setup, Duran glass was used. It has also good wall relaxation properties such that xenon polarization can build up. In Fig. (4.1.2) the design of the optical pumping cell is depicted. It can be observed that the cell consists of two volumes. The design of the smaller volume after the inlet is copied by a Vigreux condenser. In that volume, around 0.5 grams of rubidium with high purity is stored. The choice of this Vigreux design has two advantages: During operation, the rubidium needs to be heated in order to tune its vapor pressure. Due to the larger surface, heat can be better transferred to the internal gas. Secondly, due to the Vigreux structure, the flowing gas mixture will become turbulent ensuring that it will mix with the rubidium gas. Therefore, the smaller volume is also called saturation volume. The mixture of ^{4}He, N_2, ^{129}Xe and Rb flows into the larger cylindrical-shaped volume where rubidium, and by spin-exchange, xenon is polarized.

In this setup, the temperature of both volumes can be adjusted separately. Around the saturation volume, a heating wire of 300 Watts is wound and is wrapped by aluminum foil. The larger volume, which is the actual pumping cell, is located within an aluminum jacket which is connected to four cartridge heaters with 100 W each. Due to its large heat conductivity, the aluminum jacket provides a homogeneous temperature distribution at the contact surface with the pumping cell. The jacket is enclosed by ceramic plates to ensure a thermal isolation such that temperatures up to 200°C can be reached. Both heating systems are controlled by a separate two-point controller with adjustable temperature. As feedback signal, the temperature is measured by a PT-100 sensor. The hysteresis is set to ±2°C.

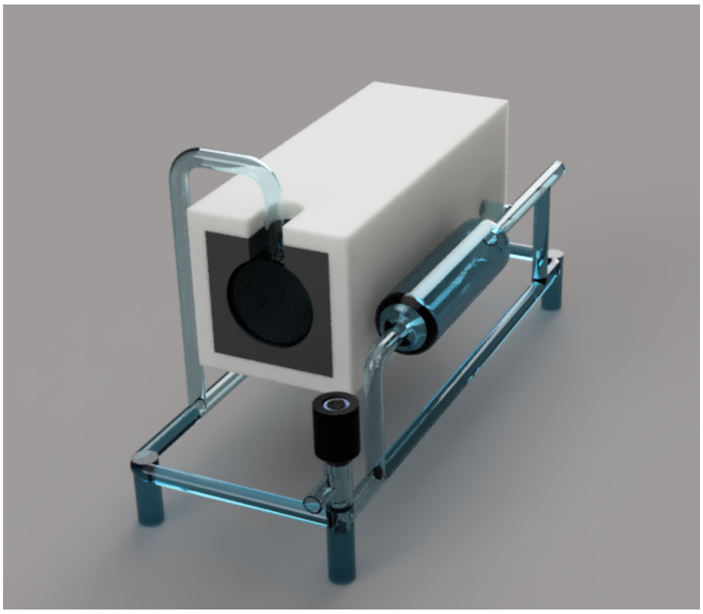

Figure 4.1.2: Optical pumping cell embedded into the oven. Source: [63].

4.1.4 Laser

The most important part for the xenon polarizer is the laser. It has to provide all the power which is pumped into a macroscopic amount of rubidium. This is achieved by exciting the D_1 transition of the rubidium atom, as explained in chapter 2. Therefore, the wavelength of the laser should be around 795 nm. The laser used in the present setup was manufactured by Optigrate (LS795-C-65 W). It provides a maximum power of 60 W at a wavelength of 795 nm. Its spectral line width is around 0.05 nm which is technically very hard to achieve at such powers. According to the manual, the laser head is based on semiconductor laser diode bars. In order to obtain the narrow line width, the broader line of the diode is narrowed by a subsequent highly resonant volume Bragg grating recorded in photo-thermo-refractive glass. Therefore, the wavelength can be tuned by changing the temperature of the glass. This allows for an optimal matching of the laser light to the rubidium-absorption line. The spectral range which can be covered by the laser reaches from 794.65 nm to 795.00 nm.

4.1.4.1 Optical setup

In Fig. (4.1.3) the optical setup is sketched. It starts with the laser which emits the photons very divergently. To obtain a parallel beam, a telescope is needed. The distance between laser and telescope is of significant importance as it will influence the beam diameter and the emittance angle. In between, a $\lambda/4$ plate is placed which can be rotated by 360°. It is assumed that the output light of the laser is already linearly polarized. An additional $\lambda/4$ plate can convert the linear polarization into a circular polarization. The condition is that the angle of the $\lambda/4$ is chosen properly. Having achieved a parallel circularly polarized beam, it can be matched to the window of the optical pumping cell. To adjust the position of the beam, two dielectric mirrors are used which can be inclined in two axes. The mirrors are specially coated ensuring that the polarization of the laser beam is not affected. After the beam has passed the optical pumping cell, it will hit the beam stop which consists of a power meter (model: 4Π, LaserCont).

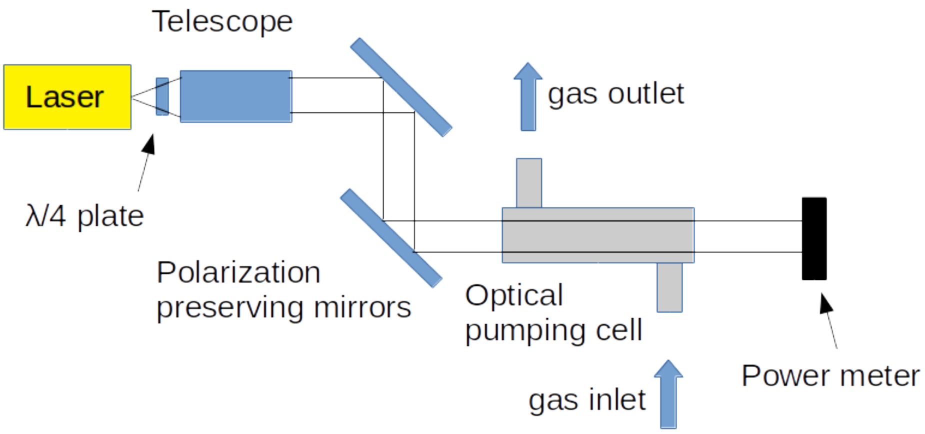

Figure 4.1.3: Setup of laser and pumping cell.

In the beginning, the laser was characterized by using this power meter. It measures the power of the laser light via the temperature change caused by absorption with a sampling rate of 1 Hz. This means that the measured signal has a very slow response and is very susceptible to systematic errors. Therefore, the sensor needs to be water-cooled for guaranteeing more stable conditions. In the Appendix, a few guidelines are provided which have to be regarded when working with such a power meter.

4.1.4.2 Laser power

In the first measurement, the maximum laser power was tested. The power meter was located between the two mirrors. With the power supply of the laser, the input current was increased in steps of 2 A. The maximum current of the laser must not exceed 50 A. In Fig. (4.1.4) the result is shown. One step took 30 s and its samples were averaged in order to obtain the data point. Therefore, the errors of the data points are too small (<0.1 W) to be resolved.

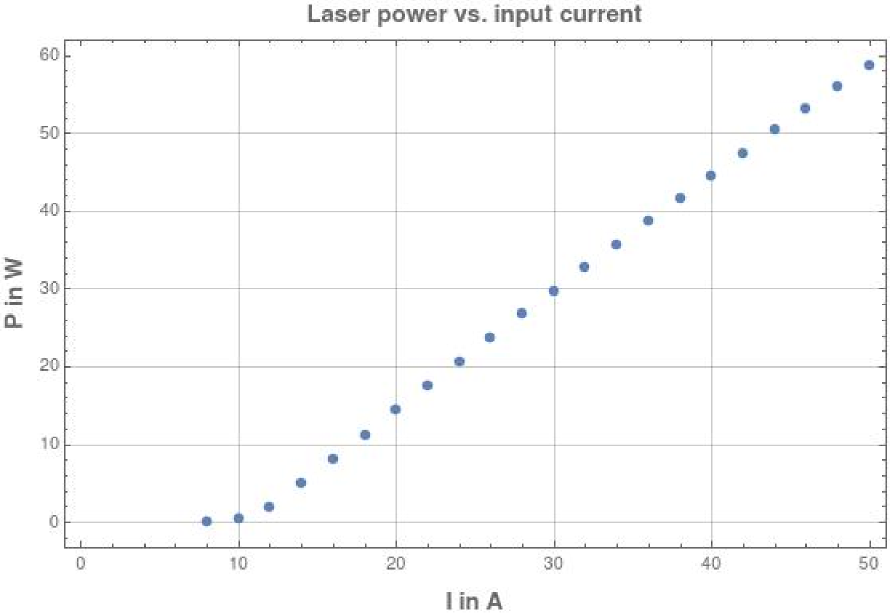

Figure 4.1.4: The laser power can be tuned with the input current.

Looking at the maximum laser power, it may be realized that the 60 W can be reached. Furthermore, a very linear dependency could be measured.

4.1.4.3 Beam profile

In the next measurement, the profile of the laser beam was regarded. One time, the power meter was put at the same location as before and another time, it was put directly before the optical pumping cell. The laser power was fixed to a constant value of around 14 W. In front of the power meter an iris diaphragm with adjustable diameter was placed. The diameter was reduced in steps of 30 seconds. The results are shown in Fig. (4.1.5). Again, all data points are averaged leading to small errors (<0.1 W). Given the fact that the distance between the two points is 800 mm, one can calculate the angle of beam divergence by reading off a difference of 6 mm in diameters of half maximum power. A value of $\alpha = 0.43°$ was found. The deviation from 0° is explained by the position of the telescope. When finding the optimal distance to the laser, the beam diameter itself is changed too. The optical pumping cell has a diameter of 42 mm which is in agreement with the beam diameter obtained by Fig. (4.1.5).

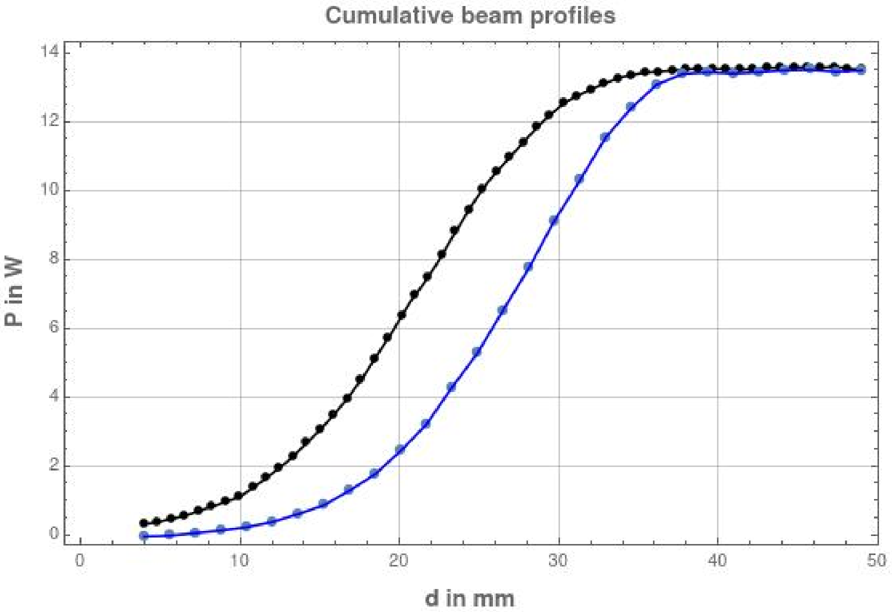

Figure 4.1.5: The cumulative laser profile was measured at two different points. Black: between the two mirrors, blue: before the optical pumping cell.

4.1.4.4 Circular polarization

In the last measurement, the most important quantity was examined which is the degree of circular polarization. In order to perform optical pumping of rubidium successfully, it is crucial to ensure that the pumping light is fully circularly polarized. Wrong components of polarization will yield to a de-pumping reducing the overall rubidium polarization. Especially at the first commissioning of such a polarizer, many parameters have to be correctly tuned. One of them is the angle of the $\lambda/4$ plate right after the laser output. When a signal of xenon polarization can be measured, it will be very easy to change the angle a bit to find its optimal setting maximizing the polarization signal. But when this signal cannot be measured, which is very likely the case for the first commissioning, it is highly desirable to reduce the free parameter space. For this reason, larger efforts were made to find the optimal setting of the $\lambda/4$ plate before measuring xenon polarization.

Before describing the procedure to measure the degree of circular polarization, the concept of Stokes parameters should be introduced. They are used to characterize the polarization state of a laser beam. In general, a beam can have linear or circular polarization. These polarizations can be mixed yielding to elliptical polarized light. But in reality, the beam may have also unpolarized components. These can be fully described by the Stokes parameters.

The following paragraphs are based on the introduction of Stokes vectors in the dissertation of Michael Wolf [48] who used an identical setup to determine the Stokes parameters for a similar laser.

An electromagnetic wave propagating in z direction can be described by its electric field vectors:

$$E_x(t) = \hat{E}_x \cos(\omega t + \delta_x) \tag{4.1.1}$$

$$E_y(t) = \hat{E}_y \cos(\omega t + \delta_y) \quad . \tag{4.1.2}$$

The Stokes parameters are defined as

$$\vec{V} = \begin{pmatrix} I \\ M \\ C \\ S \end{pmatrix} = \begin{pmatrix} \hat{E}_x^2 + \hat{E}_y^2 \\ \hat{E}_x^2 - \hat{E}_y^2 \\ 2\hat{E}_x\hat{E}_y\langle\cos(\delta)\rangle \\ 2\hat{E}_x\hat{E}_y\langle\sin(\delta)\rangle \end{pmatrix} , \tag{4.1.3}$$

where $\delta = \delta_x - \delta_y$. It is very common to normalize all components to the first one, i.e. $\bar{I} = 1$, $\bar{M} = M/I$, $\bar{C} = C/I$ and $\bar{S} = S/I$. To get more familiar with this new concept, some examples are presented. Starting with natural light, we have $\hat{E}_x^2 = \hat{E}_y^2$ and $\langle\cos(\delta)\rangle = \langle\sin(\delta)\rangle = 0$. This gives a normalized Stokes vector of

$$\vec{V}_N = \begin{pmatrix} 1 \\ 0 \\ 0 \\ 0 \end{pmatrix} \quad . \tag{4.1.4}$$

The reader may proof himself the correctness of the normalized Stokes vectors for linearly

$$\vec{V}_x = \begin{pmatrix} 1 \\ 1 \\ 0 \\ 0 \end{pmatrix}, \vec{V}_y = \begin{pmatrix} 1 \\ -1 \\ 0 \\ 0 \end{pmatrix}, \vec{V}_{45^\circ} = \begin{pmatrix} 1 \\ 0 \\ 1 \\ 0 \end{pmatrix}, \vec{V}_{-45^\circ} = \begin{pmatrix} 1 \\ 0 \\ -1 \\ 0 \end{pmatrix} \tag{4.1.5}$$

and circularly polarized light

$$\vec{V}_{RH} = \begin{pmatrix} 1 \\ 0 \\ 0 \\ 1 \end{pmatrix}, \vec{V}_{LH} = \begin{pmatrix} 1 \\ 0 \\ 0 \\ -1 \end{pmatrix} \quad . \tag{4.1.6}$$

When all Stokes parameters are known, the degree of polarization of the beam can be calculated. For that, the Stokes vector is split into a fully unpolarized and a polarized component:

$$\vec{V} = \begin{pmatrix} I_N \\ 0 \\ 0 \\ 0 \end{pmatrix} + \begin{pmatrix} I_p \\ M \\ C \\ S \end{pmatrix} \quad . \tag{4.1.7}$$

Using the fact, that for the polarized contribution $\langle\delta\rangle = \delta$, it can be calculated from the definitions of the Stokes vectors that:

$$M^2 + C^2 + S^2 = I_p^2 \quad . \tag{4.1.8}$$

Therefore, it is sensible to define the degree of polarization by

$$P = \frac{I_p}{I} = \frac{\sqrt{M^2 + C^2 + S^2}}{I} \tag{4.1.9}$$

and the degree of circular polarization by

$$P_{\text{circ}} = \frac{S}{I} \tag{4.1.10}$$

where $I = I_N + I_p$.

In order to find the Stokes parameters, a setup shown in Fig. (4.1.6) was built up. It contains a diaphragm which reduces the beam diameter to 17 mm. By milling a conical hole through an anodized plate of aluminum, it is ensured that no reflection at the boundary can affect the measured signal. After passing the diaphragm, the laser light hits a quarter wave plate ($\lambda/4$ plate) which is mounted such that it can be rotated around the beam axis using a stepper motor. In addition, a polarizing beam splitter (PBS) is put into the beam. It transmits the parallel polarized component whereas the vertically polarized component is reflected perpendicularly and hits a beam stop. The transmitted component is measured by the power meter used in the measurements before. The whole setup was mounted after the mirrors and before the optical pumping cell (see Fig. (4.1.3)).

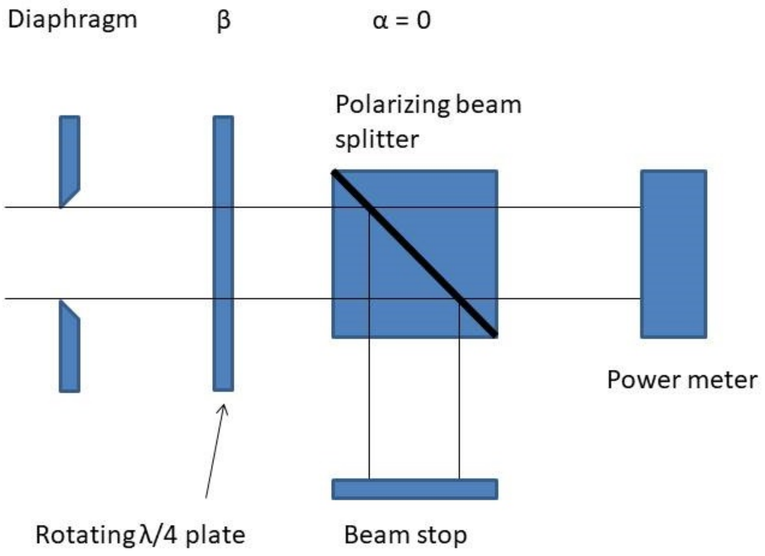

Figure 4.1.6: Setup to determine the Stokes parameters od the incident beam. The $\lambda/4$ plate is rotated around the beam axis whereas the beam splitter is kept fixed.

For an incident beam with Stokes parameters I, M, C, S the expected intensity measured by the power meter with respect to the angle β of the $\lambda/4$ plate, the angle α of the PBS, the phase shift Δ of the $\lambda/4$ plate and the fraction δ of the vertical polarized contribution transmitted by the PBS can be calculated. This formula was also calculated by Stefan Wolf [48] using the formalism of Müller matrices [64]:

$$\begin{aligned} I_{\text{measured}} = \frac{1+\delta}{2} I + \frac{1-\delta}{2} M\left[\cos(2\beta)\cos(2\alpha-2\beta) - \sin(2\beta)\sin(2\alpha-2\beta)\cos(\Delta)\right] \\ + \frac{1-\delta}{2} C\left[\sin(2\beta)\cos(2\alpha-2\beta) + \cos(2\beta)\sin(2\alpha-2\beta)\cos(\Delta)\right] \\ + \frac{1-\delta}{2} S\left[\sin(2\alpha-2\beta)\sin(\Delta)\right] \quad . \end{aligned} \tag{4.1.11}$$

In context of this thesis, it is the goal to obtain a rough estimate of the Stokes parameters. Therefore, a more idealistic picture may be drawn. Assuming an ideal $\lambda/4$ plate ($\Delta = \pi/2$) and an ideal PBS ($\delta = 0$), equation (4.1.11) becomes more simple. Due to the fact that the PBS is not rotating, α can be fixed to 0°. It remains

$$I_{\text{measured}} = \frac{1}{2} I + \frac{1}{4} M + \frac{1}{4} M\cos(4\beta) - \frac{1}{2} S\sin(2\beta) + \frac{1}{4} C\sin(4\beta) \quad . \tag{4.1.12}$$

The strategy is now to measure the power of transmitted laser light as a function of β. To achieve this, a stepper motor was used which rotated the $\lambda/4$ plate. It was found that not only the $\sin(2\beta)$ term can be used as signal for contributions of circular polarization. By one rotation in β, all Stokes parameters can be extracted by one fit. This is a striking difference to the procedure used in Stefan Wolf's thesis. In retrospect, however, it turned out that this procedure is already well-known and used e.g. in [65].

Again, as in the measurements before, the rotation around β was divided into several steps of 30 seconds duration. Over each step the average was taken yielding to a statistical error below 0.1 W. By fitting the function

$$f(t) = a\sin(2\omega t) + b_1\sin(4\omega t) + b_2\cos(4\omega t) + d \tag{4.1.13}$$

to the angle dependency measured, the Stokes parameters can be extracted by

$$I = 2d - 2b_2 \tag{4.1.14}$$

$$M = 4b_2 \tag{4.1.15}$$

$$C = 4b_1 \tag{4.1.16}$$

$$S = -2a. \tag{4.1.17}$$

In order to do this correctly, the angle β should be precisely known. Unfortunately, this was not the case for the $\lambda/4$ plate which was used. For this reason, the time was shifted, such that there was no contributing $\cos(2\omega t)$ term. The disadvantage of this method is that the sign of the Stokes parameter S is lost, i.e. one cannot distinguish between left and right handed circularity. But for the first, it is sufficient to maximize its absolute value. This can be achieved by carefully changing the angle ϕ of the first $\lambda/4$ plate right after the laser as shown in Fig. (4.1.3). It is important to not confuse it with the $\lambda/4$ plate rotating with angle β. In Fig. (4.1.7), two sweeps in β are shown with different settings of ϕ. For $\phi = 246°$, the best circular polarization was found. This can be seen at the black line in Fig. (4.1.7). It does not show any contributions from the 4ω terms in fit function $f(t)$. These will become larger, when ϕ is 254° which is 8° away from the optimum. In this case, the incident laser beam contains already measurable elliptical components. For these measurements, the laser power was chosen to the maximum power of 50 W. This was done to increase the signal-to-noise ratio such that the fits produce clean signals.

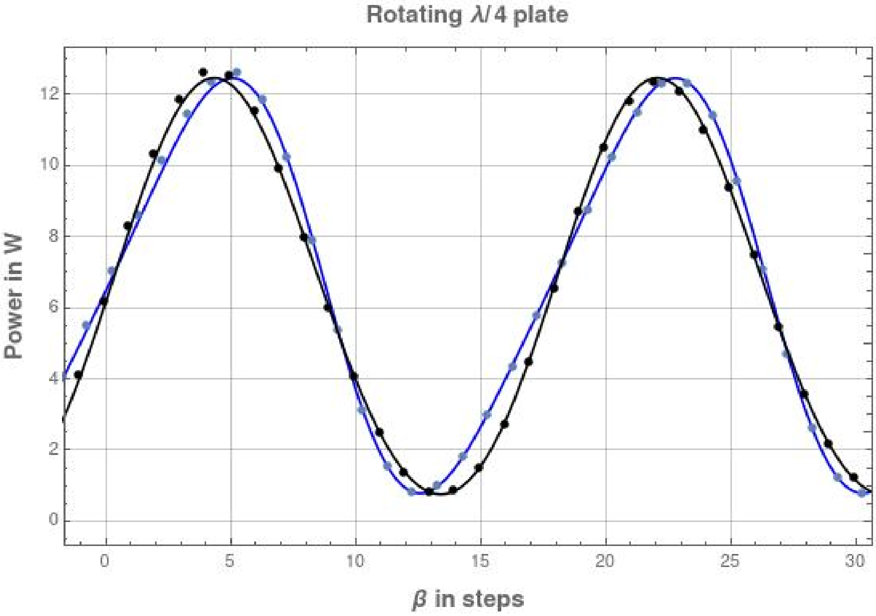

Figure 4.1.7: Signal dependency of angle β. Black: Only the doubled frequency contributes when the incident beam is circular polarized. Blue: If the beam contains elliptic components, the $\sin(4\omega)$ and $\cos(4\omega)$ terms will contribute.

In Fig. (4.1.8), the measured circular polarization obtained by Eq. (4.1.11) and the degree of polarization (4.1.9) with different settings for ϕ are plotted. It is clearly an optimum to observe for the circular polarization (blue) whereas the degree of polarization (orange) remains nearly constant. Going to $\phi = 246°$, the following Stokes parameters can be found:

$$I = 13.22 \pm 0.04 \tag{4.1.18}$$
$$M = -0.95 \pm 0.07 \tag{4.1.19}$$
$$C = 0.40 \pm 0.07 \tag{4.1.20}$$
$$S = \pm 11.70 \pm 0.04 \quad . \tag{4.1.21}$$

The sign of S is unknown, as explained above. Plugging these values into Eq. (4.1.11), a maximum circular polarization of

$$P_{\text{circ}} = 0.885 \pm 0.004 \tag{4.1.22}$$

and a degree of polarization of

$$P = 0.889 \pm 0.004 \tag{4.1.23}$$

is obtained. It seems to be surprising that a large fraction (10 %) of unpolarized light is measured. The reason has not been examined yet. Possible unknowns in this context are the mirrors, the telescope or the laser itself. One possibility to remove this unpolarized component is to place a large PBS (5 cm) before the optical pumping cell followed by a $\lambda/4$ plate. Due to the cost of such a PBS it should be carefully checked how much the polarization process will be improved.

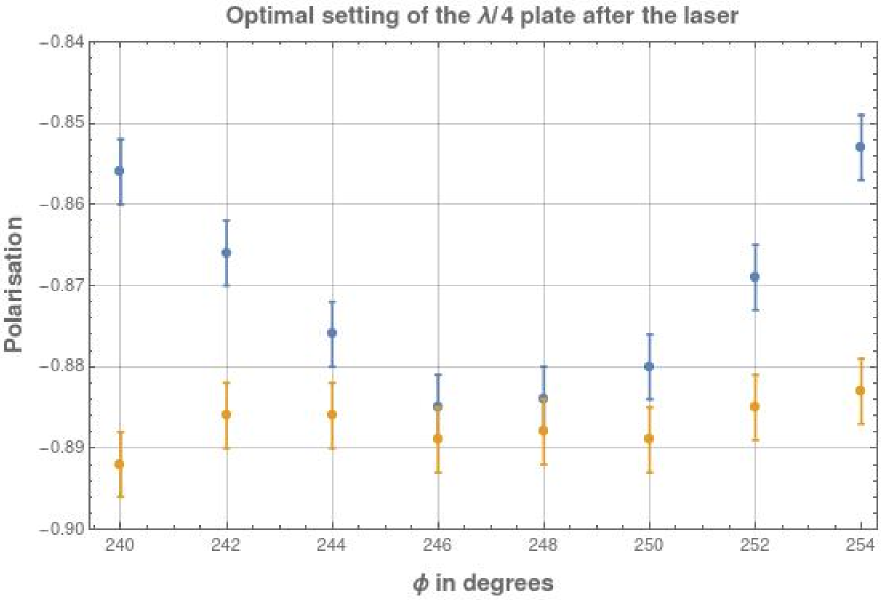

Figure 4.1.8: Circular polarization (blue) and degree of polarization (orange) depending on the angle ϕ of the first $\lambda/4$ plate.

4.1.5 NMR online monitor

In order to optimize several parameters determining the degree of polarization of the xenon gas, it would be helpful to have access to a live signal which can be maximized when optimizing a parameter.

4.1.5.1 Setup

To obtain a measure for the xenon polarization, an NMR coil was installed after the optical pumping cell (see Fig. (4.1.1)). The coil is wound around a U-shaped glass pipe with 180 turns using enameled copper wire (diameter 200 µm). Furthermore, a stimulus coil with 10 turns was added. It has a resistor of 50 kΩ in series and was connected to a function generator allowing to acquire frequency scans or applying synthetic NMR-signals.

The NMR coil is used for both, as flip coil applying Pi/2 or Pi pulses and as pickup coil measuring the signal of spin precession. For a good signal-to-noise ratio the NMR-coil is shielded by a housing of copper with 5 mm thickness. Additionally, the NMR coil is

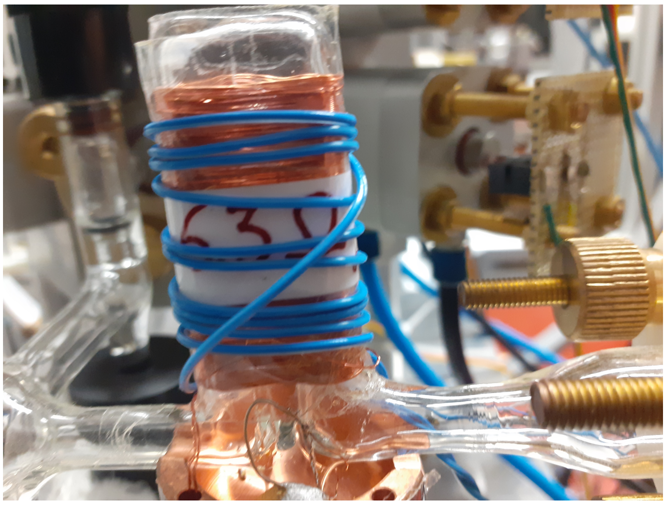

Figure 4.1.9: NMR coil with stimulus coil (blue) for systematic tests. The gas mixture flows from left to right.

attached to an LC filter tuned to the resonance frequency given by the magnetic field B_0. Given a good Q-factor, noise contributions from irrelevant frequency components are extremely suppressed whereas the frequency component of interest is amplified.

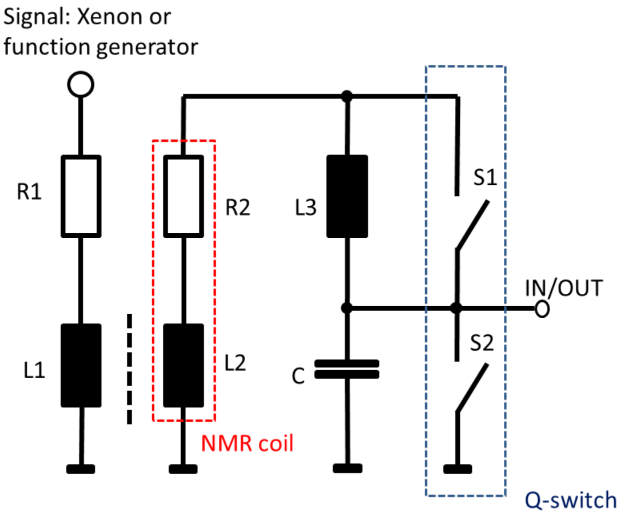

Figure 4.1.10: Peripheral circuit of the NMR coil. In the beginning, the Q switch was not part of the circuit and was added later.

The Q-factor of the series circuit of R_2, $L = L_2 + L_3$ and C is given by

$$Q = \frac{1}{R_2}\sqrt{\frac{L}{C}} \quad . \tag{4.1.24}$$

R_2 is given by the series resistance of the NMR coil and cannot be further minimized. Care must be taken choosing a proper capacitor. Its equivalent series resistance (ESR) should not be too large. The ratio of L and C can be optimized such that C is made small (8 nF) and L rather large (5.5 mH). Such a large inductance can be achieved by winding a coil around a toroid ferrite. The more windings are added the larger the inductance becomes but also the series resistance will increase. To test the NMR circuit, a frequency scan was taken. With a function generator, a sine wave was applied to the stimulus coil. A linear frequency sweep from 20 kHz to 30 kHz within 10 seconds was chosen. The signal at "IN/OUT" (see Fig. (4.1.10)) was recorded with an oscilloscope measuring its envelope.

In Fig. (4.1.11), the result is shown. As fit function, the transfer function of the RCL series circuit was used. It is important to multiply it with ω due to the induction law. The induced voltage over L_2 scales with the time derivative of the magnetic field. The offset d was introduced in order to account for the noise level contributing to the envelope of the signal

$$A(\omega) = \frac{a\omega}{\sqrt{C^2 R_2^2 \omega^2 + (CL\omega^2 - 1)^2}} + d \quad . \tag{4.1.25}$$

It is important to mention that the fit parameters have to be chosen as a, d, $u = CR_2$ and $v = CL$. It is not possible to fit R_2, C, L separately, as they occur linear dependently in the transfer function above. The resonance frequency and the Q factor are given by:

$$f_0 = \frac{1}{2\pi\sqrt{v}} \tag{4.1.26}$$

$$Q = \sqrt{\frac{v}{u^2}} \quad . \tag{4.1.27}$$

Using the obtained fit parameters u and v, a resonance frequency of (24215.4 ± 0.8) Hz and a Q factor of (73.1 ± 0.4) were estimated.

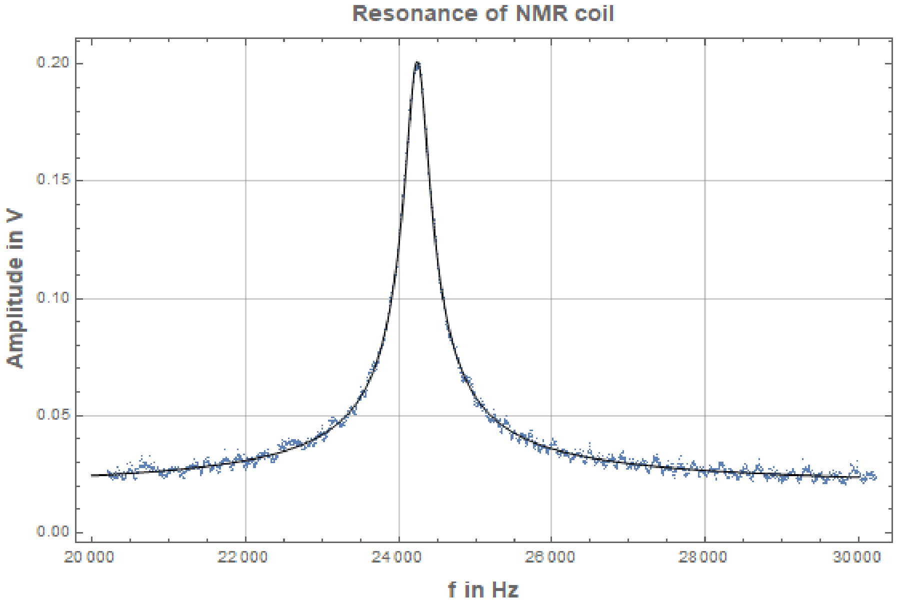

Figure 4.1.11: Frequency sweep of the NMR circuit with fitted function $A(\omega)$.

The resonance circuit is connected to a Low Field NMR spectrometer (KEA-2, Magritek). It measures the precession signals and generates the excitation pulses which are amplified by a self-made gated operational-amplifier circuit (see Appendix 8). To control the spectrometer, the proprietary software Prospa is used. It allows to set up the excitation pulses and handles the data storage. When the spins are flipped by a Pi/2 pulse, the signal of the free induction decay (FID) is measured by the resonance circuit. The voltage signal is fed into a preamplifier. After the preamplifier, the signal is mixed down yielding to a real and an imaginary part. By taking the absolute of both signals, the envelope of the FID can be regarded, which is helpful to extract the relaxation time. Alternatively, the Fast-Fourier Transform (FFT) can be calculated from the complex data points allowing to infer the precession frequency of the spins.

4.1.5.2 Q-switch

When starting to perform first tests with this setup, a serious problem became apparent. It is well-known when working with resonance circuits and is called ring down. Applying a Pi/2 pulse for typically 1 ms the resonance circuit is excited and starts to oscillate. After the Pi/2 pulse, the oscillation is damped by the finite Q and decays exponentially (see Fig. (4.1.12)). As a consequence, the data acquisition should start approx. 10 ms after the Pi/2 pulse stopped. Assuming relaxation times at the same order of magnitude, a large fraction of the FID signal cannot be measured. It would be favorable to start the acquisition shortly after the excitation pulse. Therefore, the effect of the ring down must be minimized.

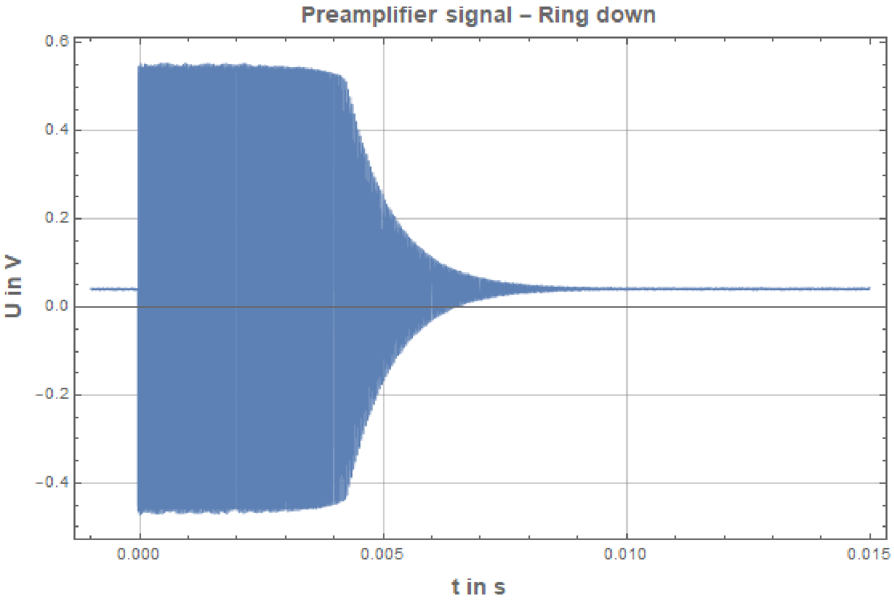

Figure 4.1.12: Preamplifier signal of the spectrometer. After a 1 ms pulse, a clear ring down occurs. The preamplifier is saturated for the first milliseconds.

The idea was to add a Q-switch to the resonance circuit which was already successfully realized in e.g. [66] and [67]. As the name suggests, the Q factor of the circuit can be changed depending on whether a pulse is applied, or a signal is measured. The first try was to insert a switch S1 across L3 (see Fig. (4.1.10)). For S1, an analog switch (DG419, Maxim Integrated) was used. It can be controlled by a TTL signal and provides a low resistance of 35 Ω when activated. When S1 is closed, the Q factor of the resonance circuit is very low. This has the favorable side effect, that low voltages are needed when feeding a pulse into the resonance circuit with a certain power. Without S1 several tens of volts were needed to apply a pulse of 10 mA. With S1 closed, the voltage is only 2 V. The strategy is to activate S1 when a pulse is applied. The timing is handled by a microcontroller (ATMega328, Atmel). By default, S1 is activated. The microcontroller waits for a rising edge of the trigger signal by the spectrometer. During the applied pulse the trigger signal remains HIGH. A few microseconds after the pulse, S1 is opened such that the Q factor is maximum. Now the data acquisition is started and runs for typically 100 ms. Finally, S1 is closed again and the microcontroller waits for the next trigger pulse.

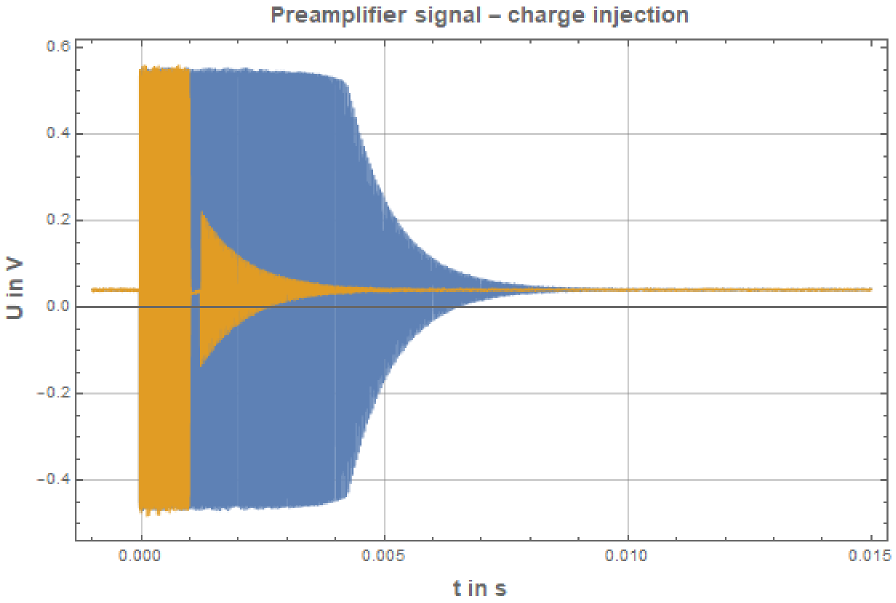

Figure 4.1.13: Adding the analog switch S1, the ring down can be efficiently suppressed. When opening S1, however, the charge injection becomes apparent.

When testing this procedure, it was realized that charge injection plays an important role here. In Fig. (4.1.13) it can be observed that right after the pulse, the ring down is perfectly suppressed as long S1 is closed. When opening S1, however, a small ring down occurs. It is caused by a small amount of charge sitting on a gate of a MOSFET. When the MOSFET switches, the charge

$$Q = C_{\mathrm{GC}}(V_G^{\mathrm{final}} - V_G^{\mathrm{initial}}) \tag{4.1.28}$$

is transferred into the MOSFET channel [68] and therefore injected into the resonance circuit. C_{GC} is the gate-channel capacitance of the MOSFET used in the chip of the analog switch and V_G are the gate voltages before and after switching. The charge cannot be minimized but it can be distributed over time. The second idea is to avoid a fast switching but to slowly ramp the gate voltage. When the characteristic time constant matches the period of the resonance frequency, the resonance circuit will not oscillate because the charge cancels for exactly one period. The problem with this idea is that it is impossible to access the MOSFET gate of the analog switch as it is an integrated circuit. For this reason, S2 was added to the schematic (see Fig. (4.1.10)) which is a discrete MOSFET (SST221, Calogic). When choosing a MOSFET, it has to be ensured that its body diode is not connected internally to Drain or Source. Otherwise, when connected to the resonance circuit, the positive/negative component of the bipolar signal from the excitation pulses is cut. In Fig. (4.1.14) the configuration of the body diode is shown.

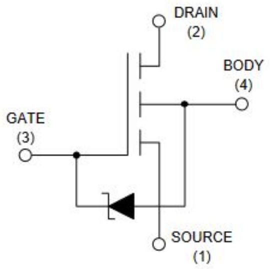

Figure 4.1.14: Symbol of the MOSFET SST211 used as second switch, source: [69].

Drain is connected to ”IN/OUT”, Source to GND and Body is clamped to -5 V. The Gate is controlled by a TTL signal originating from the microcontroller. The ramp of the switching signal is achieved by an RC filter which is located between the gate and the microcontroller. By tuning the time constant of the RC filter, the ring down caused by the charge injection could be minimized. In Fig. (4.1.15), it can be observed that almost no ring down is left. Therefore, the acquisition can be started 1ms after the excitation pulse has stopped. This provides a significant gain in signal that can be measured compared to the situation without these switches.

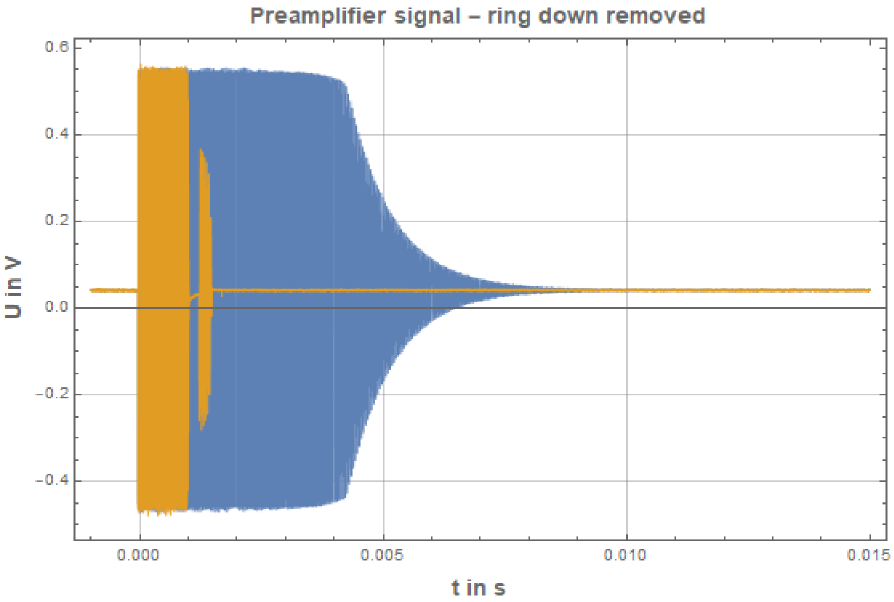

Figure 4.1.15: The combination of S1 and S2 produces the best result such that the data acquisition can be started 1ms after the pulse has stopped.

After the Q-Switch was installed, it was carefully tested how the analog switch and the MOSFET are affecting the behavior of the resonance circuit. Of course, both switches must be opened during this consideration. It turns out that the resonance curve does not change significantly, Q and f_0 remained nearly the same: Q $= (72.1 \pm 0.2)$ and $f_0 = (24240.6 \pm 0.4)$ Hz. One drawback is the increase in noise. In order to operate both switches, a symmetric power supply of ±5 V is necessary. The voltages are created using DC-DC converters followed by voltage regulators. This setup can be easily constructed but its noise performance has not been optimized yet.

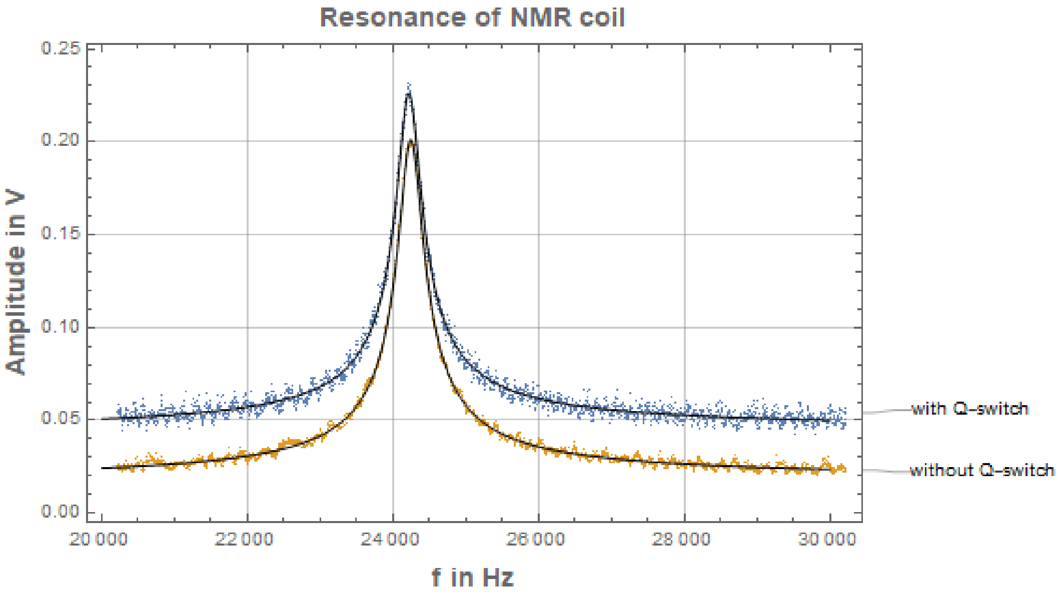

Figure 4.1.16: Effect of the installed Q-switch to the resonance curve.

To sum up this section, a timing diagram of the switches S1 and S2 is shown. ”1” means the switch is activated (closed) and ”0” means the switch is opened. When defining the time delay between the edges, the overall goal was to minimize the time difference between excitation pulse and data acquisition. On the other hand, however, the switching times may not be too short. Otherwise, the ring down originating from the charge injection of S1 is not completely suppressed. Therefore, a compromise has to be chosen.

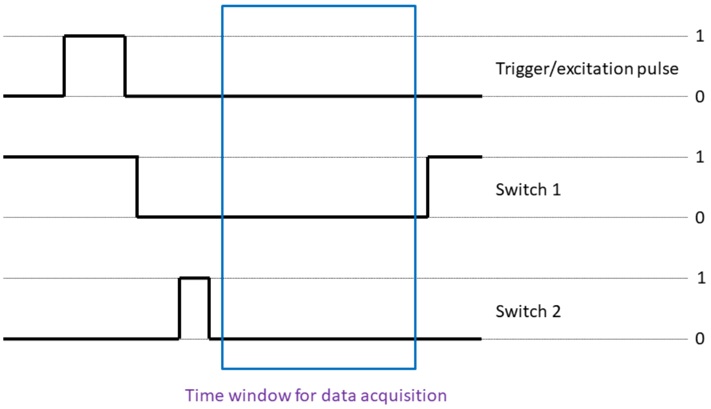

Figure 4.1.17: Timing sequence of the switches (not to scale). The rising edge of the trigger signal starts the sequence which is controlled by the microcontroller.

4.1.5.3 Setting up 90° pulses using Prospa

In order to obtain an estimate of the polarization of the xenon gas, the FID signal can be regarded. The KEA spectrometer provides the opportunity to configure excitation pulses to flip the spins by 90°. This is achieved by an internal macro called ”1 Pulse”. It applies a sinusoidal current to the NMR coil which is modulated by a rectangle. The parameters which can be chosen are divided into two sets. The first one (see Fig. (4.1.18)) determines the characteristics of the pulse sequence, like height, duration and frequency. The frequency f_0 should be chosen such that it matches the Larmor frequency of the precessing xenon nuclei. The duration and the height of the pulse is chosen according to equation (2.2.2). Typically, the duration was chosen to 1ms which is the maximum value that the spectrometer supports. Another parameter is the acquisition delay. It can be also set to 1ms due to the Q-switch described before. Without Q-switch, it should be set to 10ms and a large fraction of signal would be lost. The last parameter to set is the repetition time defining the time between two NMR shots. The second set of parameters (see Fig. (4.1.19)) is used to set up the acquisition. The number of complex points times the dwell time gives the total acquisition time. The inverse of the dwell time gives the spectral bandwidth. Depending on the noise level, it might be necessary to average over several shots. This can be achieved by checking the ”Accumulate” button. In the field ”Number of scans” it can specified how often to average.

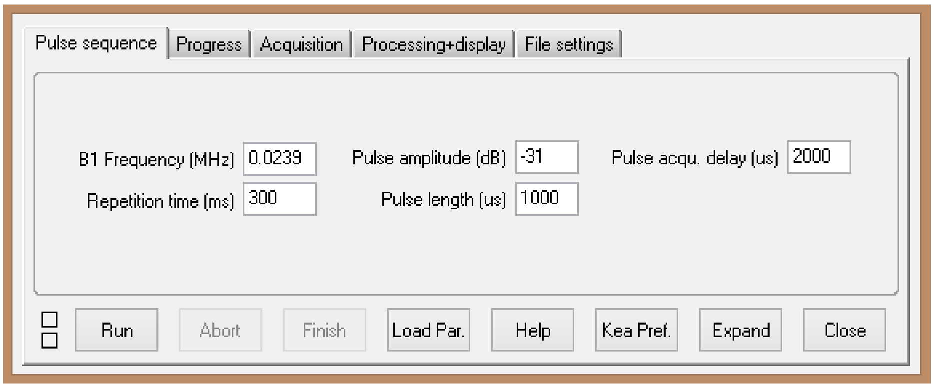

B1 Frequency (MHz) 0.0239
Repetition time (ms) 300
Pulse amplitude (dB) -31
Pulse length (us) 1000
Pulse acqu. delay (us) 2000

Figure 4.1.18: User interface to setup 90° pulse.

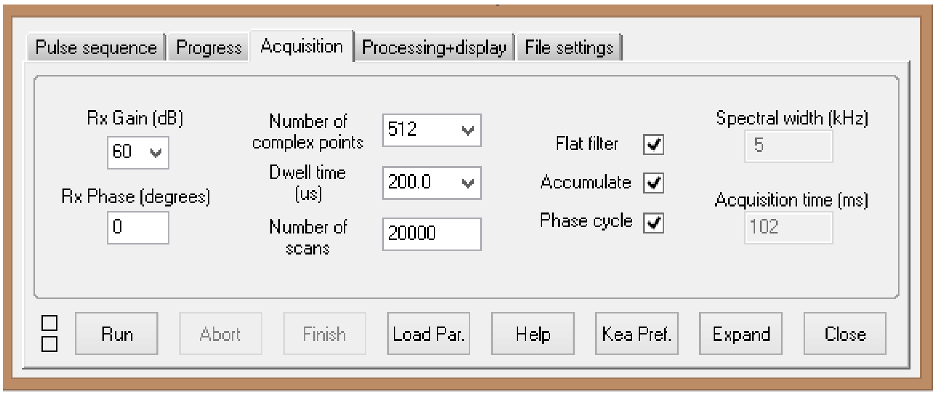

Rx Gain (dB) 60
Rx Phase (degrees) 0
Number of complex points 512
Dwell time (us) 200.0
Number of scans 20000
Flat filter ☑
Accumulate ☑
Phase cycle ☑
Spectral width (kHz) 5
Acquisition time (ms) 102

Figure 4.1.19: User interface to set up the data acquisition.

4.1.6 Magnetic coil system

For the production and storage of HP xenon, a homogeneous magnetic field is necessary. During the optical pumping process, it defines the quantization axis for the valence electron of the rubidium and the xenon spins. In the former setup used in [62], the magnitude of the magnetic holding field was chosen to be 2 mT which was adopted for the present setup. The holding field is generated by a Helmholtz-like configuration of coils. Copper wire with diameter of 1 mm is wound around 12 bicycle rims which are mounted in a row with same symmetry axis. The positions and number of turns are found in Tab. (4.1.1). When designing the coil system, the goal was to reach a field homogeneity of 10^{-3} cm^{-1}. All coils are connected in series to each other and are fed by a power supply with 5 A/300 V maximum ratings (Gen300-5, TDK-Lambda). It is operated in constant current mode providing a stability of 10^{-4} in time. To obtain the desired magnetic field, a current of roughly 2.1 A is applied yielding to a voltage of around 150 V and a heating of the copper wires to maximum 60°C.

# Coil	position in mm	turns
1	-37.5	78
2	-12.5	78
3	12.5	79
4	37.5	78
5	291	187
6	507	145
7	661.5	57
8	686.5	58
9	841	145
10	1057	187
11	1335.5	162
12	1360.5	162

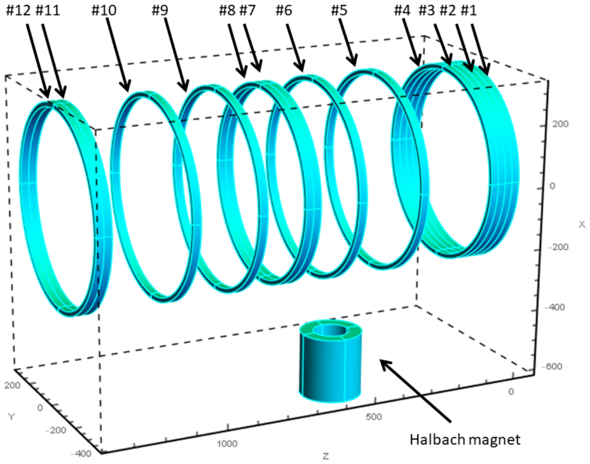

Table 4.1.1: Parameters of the coils generating the magnetic holding field.

In Fig. (4.1.1), the arrangement of the coils is depicted. Additionally, the Halbach magnet with a field strength of 0.3 T in z direction (parallel to the symmetry axis of the coils) is shown. It is needed for accumulating the HP xenon, as it will be explained in a later section. Due to the difference of two orders of magnitude, the position of the Halbach magnet has to be chosen carefully in order to avoid zero crossings of the magnetic field. Otherwise, the polarization of the xenon is immediately lost. Along the transition from the 2 mT regime into the center of the Halbach magnet, the field should therefore change adiabatically.

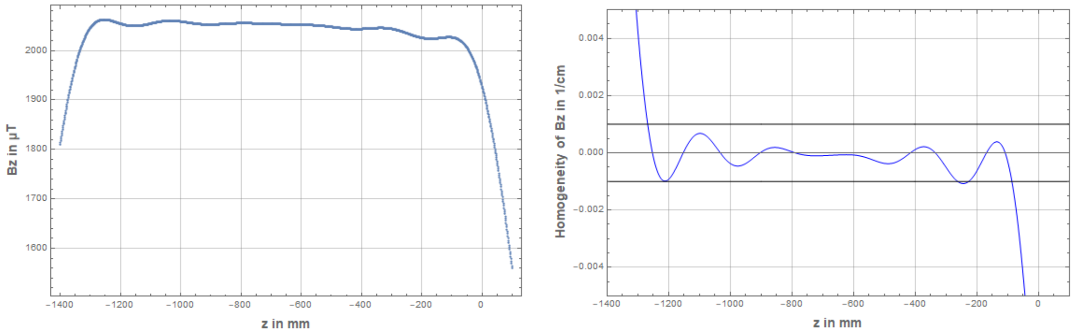

Figure 4.1.20: Simulated magnetic field along the symmetry axis without Halbach magnet. Left: z component of the magnetic field, right: corresponding homogeneity.

4.1.7 Titanium block

The titanium block has to perform various tasks. It serves as pressure monitor during the process of polarization, it is needed when the accumulated xenon is thawed and expanded into the buffer cell and it can produce customized gas mixtures of HP ^{3}He and ^{129}Xe plus an additional buffer gas like N_2. Finally, when the proper gas mixture is produced, this unit is able to connect to the measurement cell within the MSR via a transfer line which will be introduced in chapter 6. It is mandatory in order to transport the HP gas mixture into the MSR to be measured by the SQUIDs.

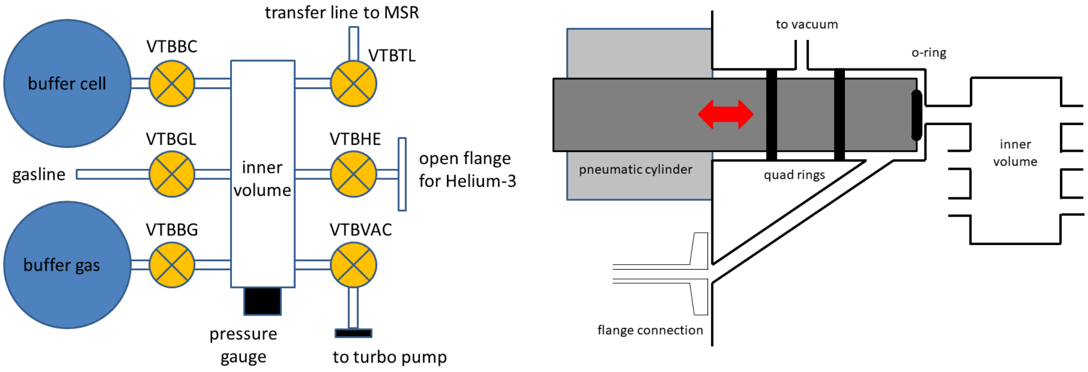

Figure 4.1.21: Left: Circuit of the gas mixing unit, Right: Sketch of the working principle for a single valve.

In Fig. (4.1.21) a schematic overview of the gas mixing unit is depicted. It can be described by an inner volume which can be connected to six different lines. The pressure within the inner volume can be measured by a ceramic sensor (ME770, Ansys). It provides an analog signal of 0.5-4.5 V which is sampled by a 12-bit ADC (MCP3208, Microchip Technology) with a rate of 4 Hz. By opening the corresponding valves, the pressure of each line can be obtained in this way. Each connection is opened and closed by automated pneumatic valves. They consist of a moving piston which is embedded into two quad rings. At the front, an additional O-ring is mounted which is separating the inner volume from the corresponding line when the valve is closed. In the inner volume, HP gas may occur which is very susceptible to smallest contributions of oxygen. For this reason, the transition via the quad rings has to be safe. When moving the cylinder, however, it is not avoidable that smallest amounts of gas are leaking through the quad rings. The solution is to connect the volume between the two quad rings to the vacuum pump. In this way, the gas never has the chance to pass from one side to the other. Another consequence of working with HP gases is that no magnetic materials are allowed. Furthermore, the wall relaxation with this material should not be too large. Good experiences have been made with titanium which is very resistant to corrosion. So, the whole mixing unit consists of a block of titanium in which the inner volume and the connection lines are milled. The pneumatic cylinders are attached to it from outside.

Starting from Fig. (4.1.1), the titanium block is connected to the gas line of the polarizer via the valve VKTB. In standard operation mode, all connections of the titanium block are closed except for VTBGL (see Fig. (4.1.21)) and the pressure of the gas line can be monitored. The valves VTBBC and VTBBG are connected with spherical glass cells with a volume of roughly 500ml. The first one is acting as buffer cell into which the accumulated xenon gas is expanded. In the second one, a buffer gas like N_2 is stored which is mixed into the HP xenon. The valve VTBHE is linked to an open flange which can be used to connect an additional glass cell containing the HP ^{3}He. The whole unit can be evacuated by opening valve VTBVAC. It is important to highlight that in this case all other valves should be closed. Otherwise, the amount of gas would be too large and the running turbo pump would shut down. If, for instance, the buffer-gas cell containing 1 bar of buffer gas should be evacuated, it would be a good practice to pump it step by step by opening and closing the valves VTBVAC and VTBBG alternately. When this takes too much time, one may consider to switch on the mechanical pump and pump the volume via the gas line. The remaining valve VTBTL connects the inner volume to the transfer line.

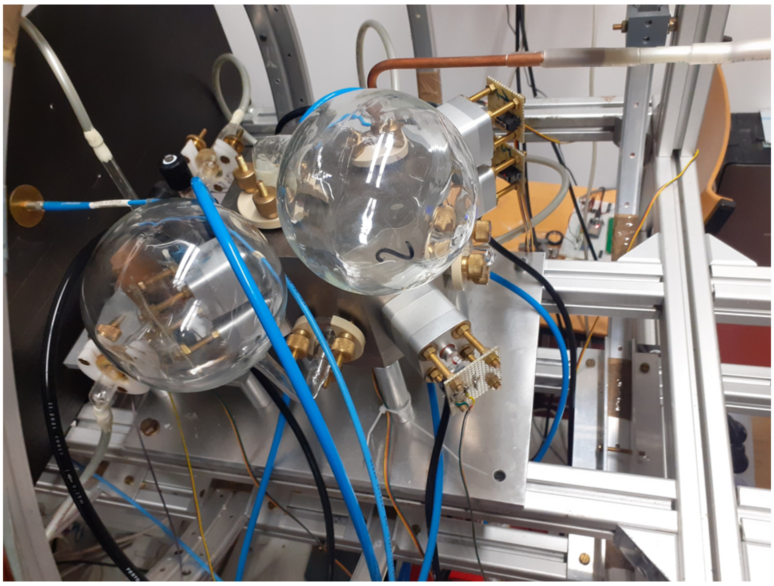

Figure 4.1.22: Gas mixing unit for the preparation of polarized gases. The two spherical glass cells and the transfer line (top-right corner) can be observed.

4.1.8 Accumulation system

Once the xenon gas was polarized within the optical pumping cell, it is still contained within the gas mixture to very low fraction (approx. 1%). The goal is to isolate the polarized xenon gas and to accumulate it up to a specific amount. The strategy achieving this goal is based on cryogenic separation. It uses the fact that xenon has a much higher melting point than the two other buffer gases nitrogen and helium. The following concept was already tested a former design [62] and was used for this xenon polarizer as well.

The basic setup of the accumulation system is shown in Fig. (4.1.23). A cold trap consisting of borosilicate glass is surrounded by a Halbach magnet of 0.3 T in its center [70], [62]. Below the magnet, two dewars can be moved horizontally and vertically. One dewar is filled with liquid nitrogen (LN_2) and the other one with hot water. When accumulating polarized xenon, the dewar containing LN_2 is lifted up such that the trap is cooled down. The buffer gases are passing the trap whereas the xenon gas is frozen out. The amount of xenon ice depends on the flow rate and the time while the LN_2 is lifted up and can be therefore well adjusted. If the desired amount of xenon was reached the gas flow would be interrupted by closing the valve VKIN (see Fig. (4.1.1)) and the trap is connected to the turbo pump in order to remove remnants of the buffer gases. The xenon ice remains and can be thawed by rearranging the dewars so that the cold finger is surrounded by hot water (see Fig. (4.1.23)).

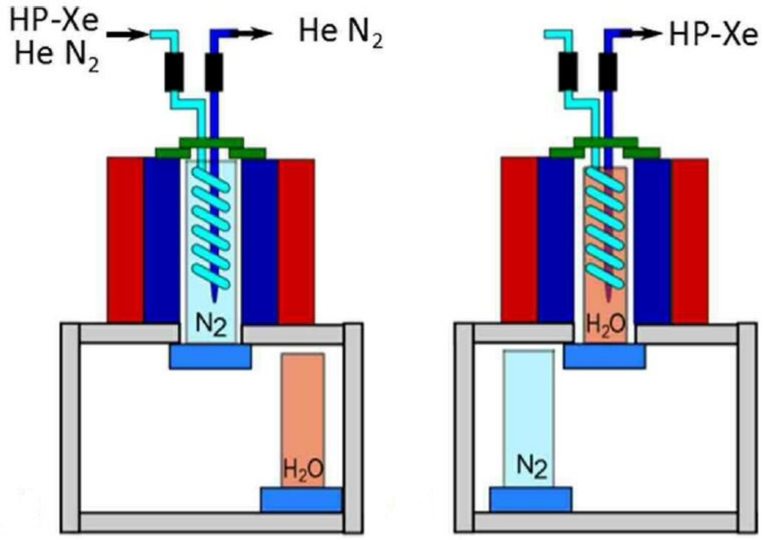

Figure 4.1.23: Cold trap with Halbach magnet, dewars of LN_2 and water. Figure extracted from [62].

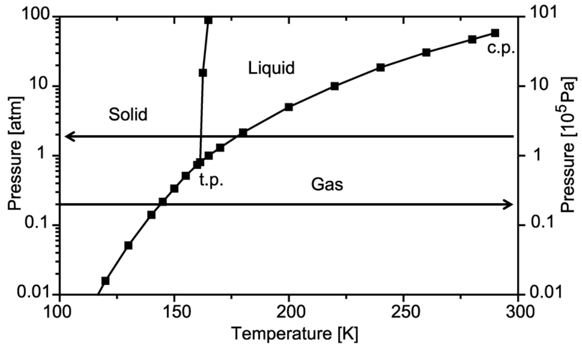

Figure 4.1.24: Freeze and thaw process for the xenon accumulation. Figure adapted from [71].

During this process, the main concern is the loss of polarization. As it can be observed in Fig. (4.1.25), T_1 of solid xenon mainly depends on the magnetic field and the temperature. Two processes are relevant: for low temperature (50-120 K) it was found that the spin-rotation interaction (see chapter 2) is responsible for spin relaxation, where it gives rise to the Raman scattering of phonons in solid xenon [72], [73]. Above 120 K an additional interaction becomes relevant which is the dipole-dipole interaction modulated by vacancy diffusion [74], [75]. It yields to a fast increase of the relaxation rate $1/T_1$. In [72] it is shown that the measurement and the theoretical expectations are nicely consistent (see Fig. (4.1.25)). At liquid nitrogen temperature, which is 77 K, and a magnetic field of 0.3 T, the T_1 relaxation time is expected to be roughly 2 h.

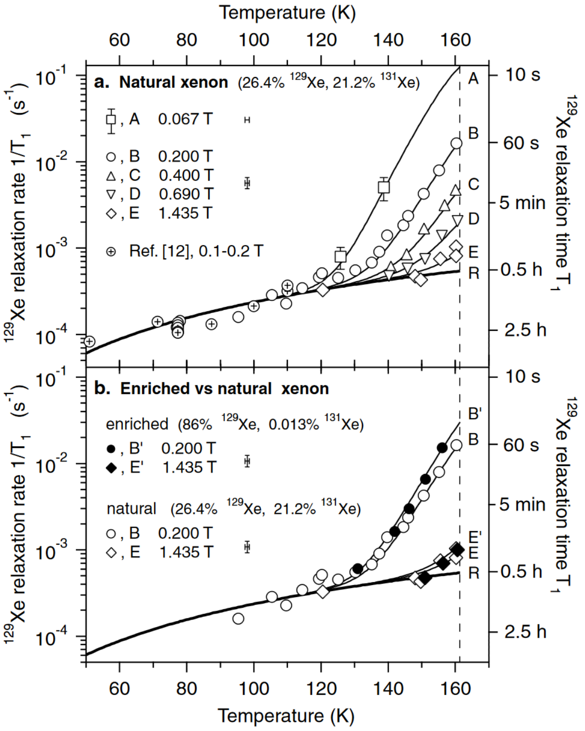

Figure 4.1.25: Dependency for T_1 of solid xenon with respect to temperature and magnetic field. Source: [72].

In this context, another effect has to be regarded. Bringing the cold trap into contact with liquid nitrogen, the glass wall will reach a thermal equilibrium. When xenon is frozen out, it is forming an ice layer at the glass walls which becomes thicker with time. With increasing thickness, the thermal isolation becomes better yielding to higher temperatures at the inner surface. This is dangerous because T_1 may drop to few seconds when the temperature is too large (see Fig. (4.1.25)). For this reason, in the previous version of the polarizer it is proposed, to lift up the dewar containing liquid nitrogen in three steps. The level of the liquid determines the region where xenon is frozen out. By changing it several times, the thickness of the ice layer is kept small. This approach was used as well during this thesis. When the gas flow was stopped by closing valve VKIN and the buffer gas have been removed through the turbo pump, valve VCOUT is closed and only valves VTBGL and VTBBC of the titanium block are opened. The frozen xenon is expanded into the volume consisting of the cold trap, the inner volume of the titanium block and the buffer cell. The volume of the buffer cell is large compared to the remnant volume and therefore most of the HP xenon can be stored within that cell.

4.1.9 Data acquisition and control

As mentioned in the section above, an ADC was used to sample the analog value of the pressure gauge in the titanium block. It is connected to an 8-bit microcontroller (ATMega2560, Atmel) via an SPI interface. This microcontroller has the task to control the pneumatic valves of the titanium block. For this purpose, a valve terminal (VTUG, Festo) is used which distributes compressed air from one input to ten output channels. Six channels are used for the pneumatic cylinders of the titanium block whereas the other four are left for future use. With a digital 24 V signal, the state of an individual channel can be controlled externally. In Fig. (4.1.22) it can be observed that a blue and a black plastic tube is connected to the cylinders. When the black tube is under pressure, the cylinder moves into the titanium block and the valve closes. Putting the blue tube under pressure, the valve opens. With a level shifter, the valves can be controlled with a 5 V TTL signal from the microcontroller. To control the valves as user on a computer, a graphical user interface was developed using the programming language C# and the .NET framework. In Fig. (4.1.26) a screenshot of the app is shown. It is divided into three tab pages. The first one establishes the connection to the hardware components via the serial interface. The second one gives access to the pressure value and to the valves of the titanium block. At the bottom, the channel of the ADC can be selected which is plotted above. The first channel is attached to the pressure gauge and the second channel is connected to the flow meter which provides an analog signal as well. All other channels are reserved and can be used for additional parameters to be monitored in the future. Furthermore, the app provides the opportunity to save the acquired data from all ADC channels into a text file. The third tab page shows the values of the coil parameters like voltage, current and temperatures. All in all, the app is used to control and monitor all relevant parameters when the polarizer is in operation.

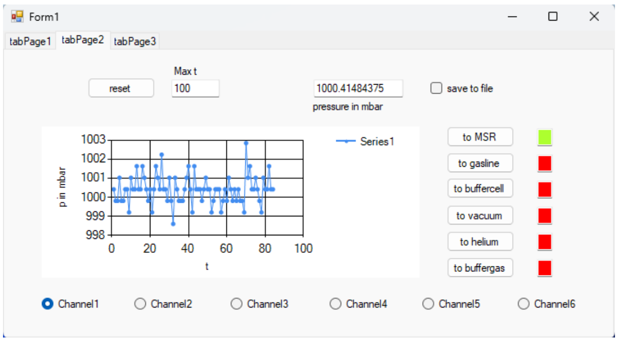

Max t: 100

pressure in mbar: 1000.41484375

☐ save to file

● Channel1 ○ Channel2 ○ Channel3 ○ Channel4 ○ Channel5 ○ Channel6

Figure 4.1.26: Graphical user interface allowing the readout of the pressure sensor and the control of the valves of the titanium block.

Additionally, it was found useful to have a logger which stores basic parameters of the laboratory like room temperature, air pressure and magnetic fields. This data can be used for diagnostics in the afterward. This was implemented in a separate system to be independent of the operation of the xenon polarizer. The basic idea was to set up an SQL database which stores all measurement values. It consists of four columns which are a primary index, a time stamp, a string giving the label of the measurement value and another string giving the actual value. The time stamp refers to the time when the data point is written into the database. All data is collected by an MQTT server and fed into the database. The power of this approach is that it is very flexible and highly scalable. As sensor platform another microcontroller (ESP32, Espressif) was set up. It has the advantage of an integrated Wi-Fi interface which can be used to transfer the data points to the MQTT server. A label can, for instance, look like ”esp32/xenon_lab/magx”. When another sensor should be added to the system, a new label can be defined in the same way. When accessing the database, the different labels can be used to filter out the desired data points. As a future project, it would be desirable to connect the C# program with the database such that all acquired data is stored at one central point.

4.1.10 Recovery of ^{3}He and ^{129}Xe

In principle, all relevant components needed for a successful operation of the xenon polarizer were introduced. Throughout this thesis, only natural xenon gas was used. In the future, however, it is desirable to use enriched ^{129}Xe which provides a three times larger signal than natural xenon due to the higher concentration of the corresponding isotope. Additionally, HP ^{3}He will be used as a comagnetometer. Both gases have in common that they are very expensive and it would not be economic to blow this gases into the atmosphere after each measurement run.

For this reason, it was decided to construct a recovery system which is able to accumulate both gases after each run. In Fig. (4.1.27), the functional schematic of this unit is depicted. All valves are represented by red or green boxes, depending on whether they are opened or not. They are fully automated using compressed air. In contrast to the valves of the titanium block, these valves need only one line which is put under pressure when the valve has to be opened. Removing the pressure will close the valve by an internal spring mechanism. Again, a valve terminal was installed delivering compressed air to all valves. Here, the channels have to be controlled by 230 V/AC. To interact with a microcontroller, an additional stage of sold-state relays was inserted. The advantage of solid-state relays is that they only switch when there is a zero crossing in the AC current. The consequence is that nearly no noise is induced when switching. Also, for the recovery system, a graphical user interface was written in the same style as it was done for the titanium block. As an additional feature, the opportunity is provided to define customized switching cycles for the valves. For this sake, macros where defined which can be written in a text file. This text file can be read in by the application and the macros are executed. At this stage, the macros were kept very simple. The following macro opens the valve to the turbo pump after five seconds: ”VTP;1;D;5;0.0”. All arguments are separated by semicolons. The first argument is the name of the valve to be switched given in Fig. (4.1.27). Only large capital letters are allowed. The second argument gives the state of the valve, ”1” means opened and ”0” closed. The next argument is ”D” by default and an integer after it gives the delay after which the switching is performed. The last argument is a float number which is reserved for future use. By adding different macros line by line, they are executed successively by the application. For reasons of flexibility, it is planned expand the macros by allowing a pressure dependent switching behavior like keeping the valve open until a certain minimum pressure is reached.

The recovery system is attached to the transfer line which connects the measurement cell within the MSR and the titanium block. It can be disconnected with a manual glass valve with a KF-16 flange (see Fig. (4.1.27), bottom left). After a measurement cycle, the goal is to transfer all of the helium-xenon gas mixture from the filling line, the measurement cell within the MSR and the titanium block into a storage volume of 10 liters. To achieve this, a helium-tight scroll pump is used to pump the gas into the recovery system. During this process, all valves are closed except for VSC, V2, VK1, VK2 and V4. It is important to mention that between V5 and V4 a check valve is installed (brown box in schematic) which ensures that no gas can leave the storage volume. To overcome the pressure difference between the storage volume (up to 1 bar) and the transfer line (typically 100 mbar) a compressor is used which can change its volume using valve V9. When the piston moves downwards, VK1 is opened and VK2 is closed. In the case of compression, the states of both valves are swapped. By repeatedly expanding and compressing the

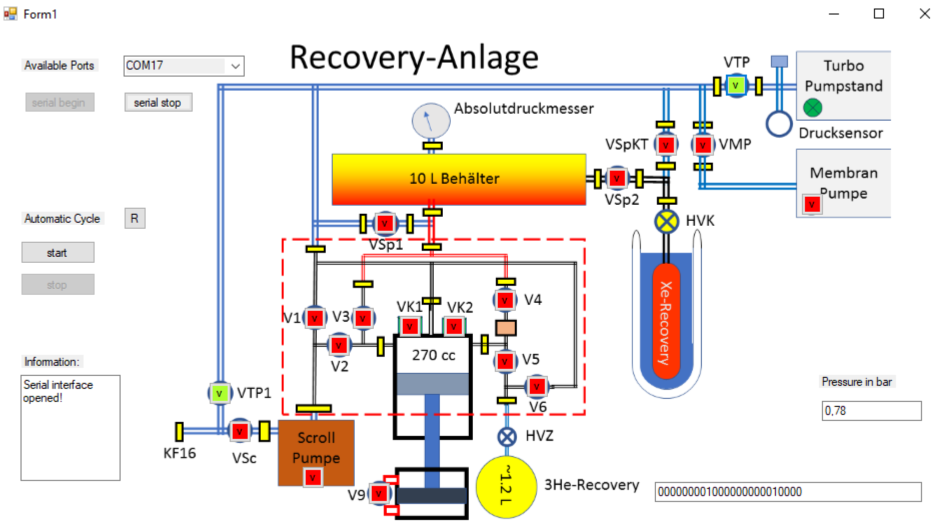

Serial interface opened!

0,78

000000001000000000010000

Figure 4.1.27: Circuit of the recovery unit.

volume, nearly all of the gas mixture can be pushed into the storage volume. Until a pressure of one bar is reached within the storage volume, several measurement runs can be performed within the MSR. Assuming an amount of 0.1 bar l per measurement, the volume of 10 liters is filled after 100 runs to 1 bar.

When the storage volume is full, the xenon gas can be isolated again by cryogenic separation. The valve HVK is a manual valve and has to be closed when all xenon is frozen out. It belongs to the gas bottle which can be disconnected from the recovery system. This bottle can be directly attached to the xenon polarizer and provides the recovered xenon gas. The remaining helium gas is pushed into a glass cell via the compressor and when the pressure is not changing anymore, the valve HVZ, which is a manual valve as well, is closed. Likewise, this glass cell can be demounted too and can be used to be polarized again.

4.2 Results

Having described all components of the xenon polarizer, important results should be presented. In the Appendix 8, all steps which are necessary to operate the polarizer are explained in full detail. In order to observe xenon polarization, the following conditions needs to be established: a stable gas flow with the correct composition of components (helium, nitrogen, xenon) at constant pressure, circularly polarized laser light with correct wavelength and a proper magnetic holding field. Furthermore, the temperatures of the optical pumping cell and the saturator should be chosen properly as well.

4.2.1 Free induction decay of HP ^{129}Xe

The only feedback available whether all parameters are correctly set is the signal of the NMR monitor. When a signal is observed, all parameters can be optimized by maximizing it. When no NMR signal is measured, it would be very hard to find the correct parameter settings. A standard method to find an NMR signal is to perform B_0-sweeps tuning the current of the holding field. In Fig. (4.2.1) a typical NMR shot is shown.

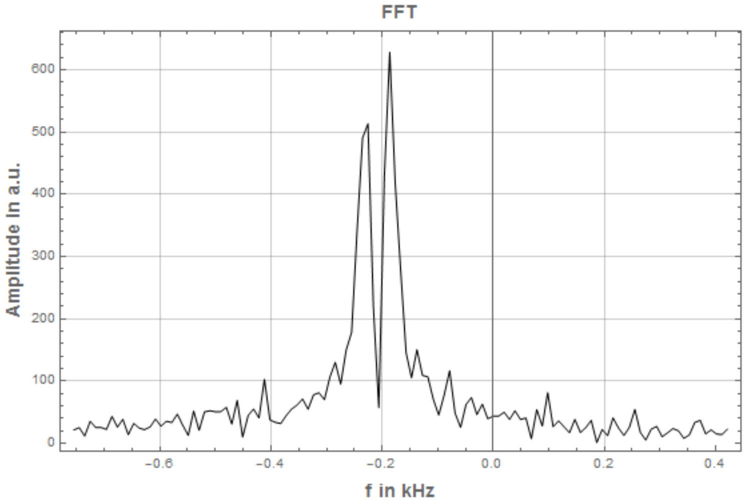

Figure 4.2.1: Fast-Fourier transform of the measured NMR signal of polarized xenon.

At the x axis, the difference of precession frequency and mixing frequency (23.9 kHz), which is called detuning, is plotted. The units of the y axis are arbitrary and scale with the voltage signal fed into the spectrometer. Regarding the FFT of the NMR shot, two peaks are observable. Their appearance can be explained by the geometry of the measurement volume which is a U profile. Because of magnetic field gradients in this region, probably caused by the Halbach magnet, the B_0 is slightly different for the two tubes. To give concrete numbers: The precession frequency of 23.7 kHz yields to a B_0 field of 2.01 mT. With the frequency difference of the two peaks of roughly 0.04 kHz and a separation of the tubes of 15 mm, a gradient of 2.3 µT/cm can be estimated which fits perfectly well to measurements which have been performed. For these measurements, a hall sensor (AK8963, AsahiKasei) was moved to equidistant points and the absolute magnetic field was acquired. The magnetic holding field was switched on and off without changing the result significantly. Therefore, it is assumed that the gradient is mainly caused by the Halbach magnet.

Going into the time domain of the signal, an exponential decay is expected. However, regarding both, real and imaginary part of the FID signal two beatings are observed. Due to the existence of two contributing frequency components, a slower beating is observed as envelope. A faster beating occurs because of the detuning of 0.2 kHz. In Fig. (4.2.2), the real and the imaginary part of the FID signal corresponding to the FFT in Fig. (4.2.1) is shown. Here, the effect of the Q-switch should be highlighted once again: without Q-switch, the data acquisition can only start from 10 ms (see Fig. (4.1.12)). Without the data points before, the double peak could not be well resolved. When measuring NMR shots, the most relevant quantity is the amplitude of the signals. One possibility to extract it is to use the maximum of the FFT which might by a bit risky. It can be observed that the peaks are sampled by few points. Therefore, the errors may become very large. Another strategy would be to take the absolute of real and imaginary part and take the average of the first ten points, for instance. Here the problem is, that the noise is included within the signal as an offset. It is not clear how to isolate the noise contribution properly. This is also the reason why the detuning was kept with ≈200 Hz quite large. By plotting the real and imaginary parts separately, no offset is observed.

For that reason, a more quantitative evaluation of the "raw" data was demanded.

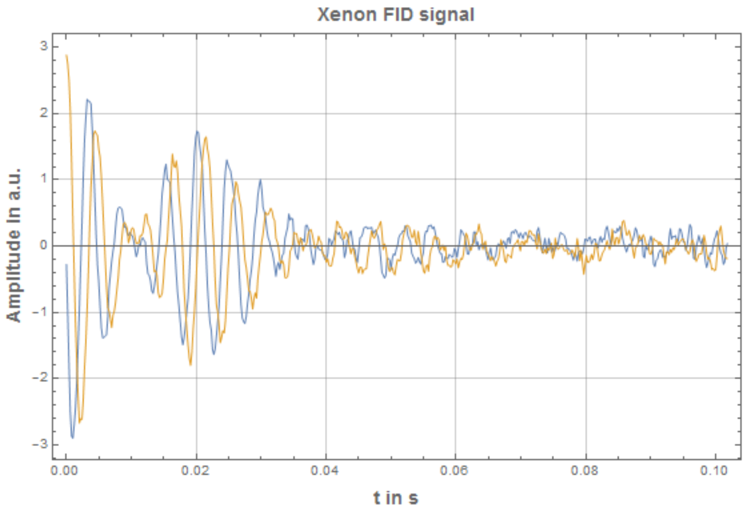

Figure 4.2.2: FID signal of polarized xenon.

In order to describe the signals mathematically, both frequency components are modeled by two sine waves with frequencies of $f_0 \pm df/2$ where f_0 is the detuning and df is the frequency difference of the two peaks. The real part is given by:

$$\begin{aligned} S_{\mathrm{Re}}(t) = \Big\{ & a_1 \cos(\phi_1) \sin\left(2\pi\left(f_0 - \frac{df}{2}\right)t\right) + a_1 \sin(\phi_1) \cos\left(2\pi\left(f_0 - \frac{df}{2}\right)t\right) + \\ & a_2 \cos(\phi_2) \sin\left(2\pi\left(f_0 + \frac{df}{2}\right)t\right) + a_2 \sin(\phi_2) \cos\left(2\pi\left(f_0 + \frac{df}{2}\right)t\right)\Big\} \\ & \times \exp\left(-\frac{t}{T_2}\right)\left(1 - \exp\left(-\frac{t+dt}{\tau}\right)\right) \quad . \end{aligned} \tag{4.2.1}$$

And the imaginary part by:

$$\begin{aligned} S_{\mathrm{Im}}(t) = -\Big\{ & a_1 \cos(\phi_1) \cos\left(2\pi\left(f_0 - \frac{df}{2}\right)t\right) - a_1 \sin(\phi_1) \sin\left(2\pi\left(f_0 - \frac{df}{2}\right)t\right) + \\ & a_2 \cos(\phi_2) \cos\left(2\pi\left(f_0 + \frac{df}{2}\right)t\right) - a_2 \sin(\phi_2) \sin\left(2\pi\left(f_0 + \frac{df}{2}\right)t\right)\Big\} \\ & \times \exp\left(-\frac{t}{T_2}\right)\left(1 - \exp\left(-\frac{t+dt}{\tau}\right)\right) \quad . \end{aligned} \tag{4.2.2}$$

The last exponential factor containing the time scale τ, is an artifact of the Q-switch described in the section above. The task of the Q-switch is to suppress the ring down of the resonance circuit by shortening it. In this state, the output voltage is always vanishing, independent of the signal acquired by the pickup coils. Assume a sinusoidal signal with constant amplitude and a frequency near the resonance frequency of the pickup coil. When the Q-switch opens the resonance circuit, the inverse effect of the ring down occurs: the output voltage starts at zero and increases exponentially until it saturates to a final amplitude. This effect can be compared to the step response of an RC circuit (with the modulated sinusoidal signal). In order to estimate the starting amplitudes of the NMR signal a_1 and a_2 correctly, this effect has to be taken into account. The parameter dt indicates when the Q-switch was released before the data acquisition has started. The value of dt was measured to be 1.3 ms ± 0.1 ms and was kept constant for the fits. The start of data acquisition was chosen to be 2 ms after the 90° pulse has finished. τ is given by the decay constant of the ring down which can be observed in Fig. (4.1.12). A measurement provides 0.949 ms ± 0.001 ms and is consistent to the given resonance frequency and Q value measured in the former section.

All free parameters are the same for $S_{\mathrm{Re}}(t)$ and $S_{\mathrm{Im}}(t)$. By changing sin with cos and choosing the correct signs, the fast beating of $S_{\mathrm{Re}}(t)$ and $S_{\mathrm{Im}}(t)$ is phase-shifted by 90°. This can be exploited by fitting both functions simultaneously to the real and imaginary data sets. This ensures that the fit routine finds the correct minimum. Furthermore, it has to be noted that the fit function has steep slopes. Therefore, it is mandatory to include x errors because a small change in x direction may yield a huge change in y direction. The fits were performed by the fit package "DataFit" which was written by Prof. Dr. Ulrich Schmidt. Finally, the simultaneous fit of the signal in Fig. (4.2.2) is presented in Fig. (4.2.3). In this way, the FID signal can be analyzed quantitatively and it is shown that the signal is understood.

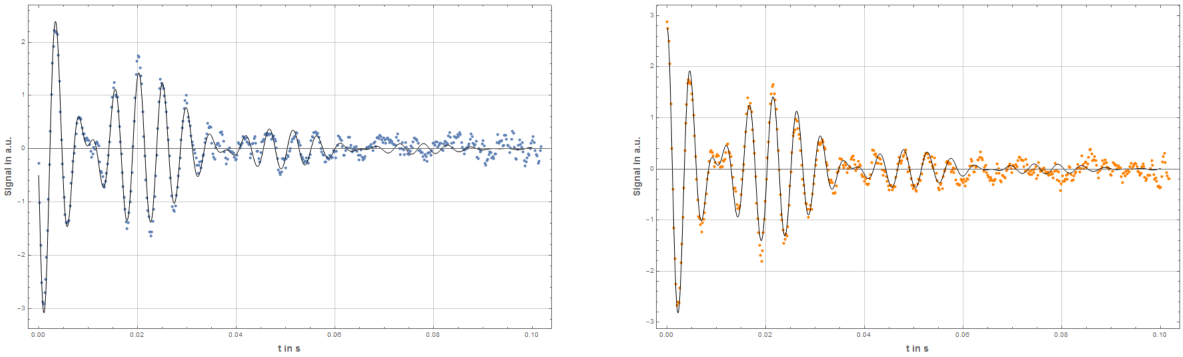

Figure 4.2.3: Simultaneous fit of real (left) and imaginary (right) part of the xenon FID signal. The error bars of 10^{-1} units have been omitted for better visibility.

Due to the low partial pressure of xenon used in the standard gas mixture (≈20 mbar at 2 bar) the signal-to-noise ratio is very low. It is recommended to accumulate over 16 shots in order to reduce noise. In a glass tube of 6 mm inner diameter, the gas flow of 200 ml/min corresponds to a mean drift velocity of 11.8 cm/s. Assuming a path length of the U-profile of 10 cm, a xenon spin needs roughly one second to pass the measuring volume. Therefore, the repetition time should be in the same order. In Fig. (4.2.4) the fitted amplitudes a_1 and a_2 are shown when the repetition time was varied. In the FFT, the amplitudes a_1 and a_2 correspond to the heights of the two peaks. It is interesting to note that one peak does not change much whereas the second peak increases with repetition time until a maximum value is reached. The first leg of the U profile always obtains polarized xenon to be measured. The second leg on the other hand, receives the depolarized gas from the first one. For this reason, it is a good practice to keep the repetition time at least at one second.

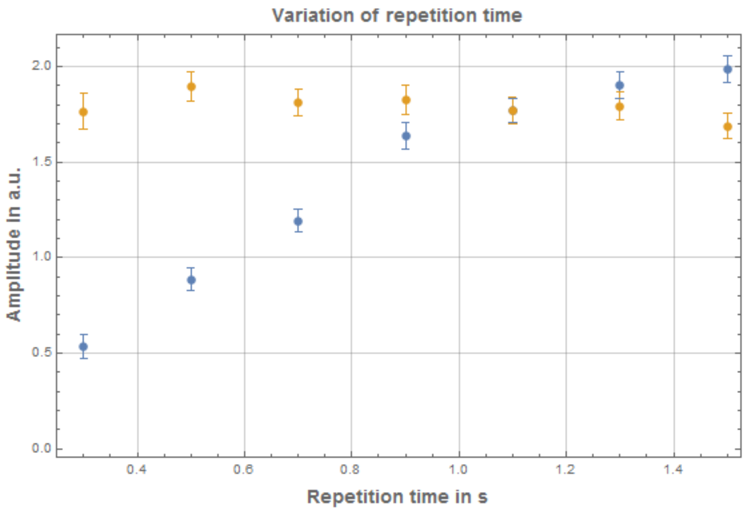

Figure 4.2.4: Amplitudes a_1 and a_2 of the NMR signal for different repetition times.

4.2.2 Long time stability of the pumping process

An important measurement is the test of the longtime behavior of the xenon polarizer under operation. In order to obtain reproducible results of the final polarization all parameters should be kept as constant as possible. In the following results, the polarizer was running for more than one hour and the NMR signal was measured for every 30 seconds. The NMR shots were fitted as explained above and the amplitude $a_1 + a_2$, the precession frequency f_0, the peak separation df and the relaxation time were extracted.

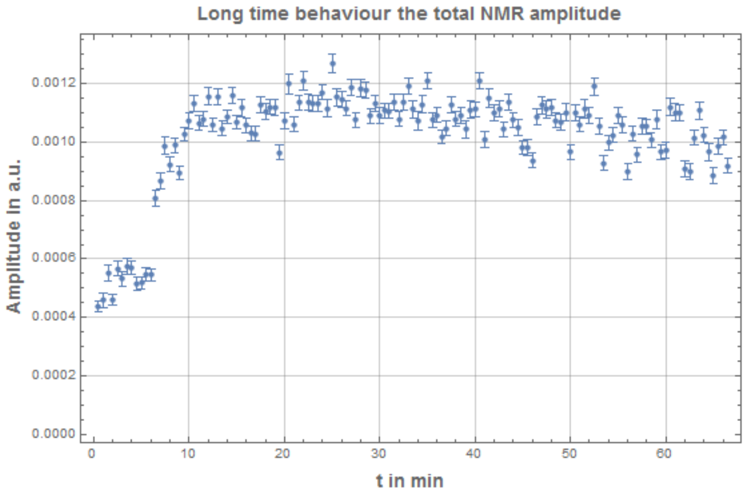

Figure 4.2.5: Amplitude of the NMR signal $a_1 + a_2$ during a long run.

In Fig. (4.2.5) the sum of the amplitudes a_1 and a_2 is shown. In the first 5 minutes, the laser power was set to 15W (corresponds to a current of 20 A) until all parameters like flow, pressure and the oven temperatures have stabilized. Then, the laser power was slowly ramped to 53 W (I=40 A). At t=10 minutes, the desired polarization process started. It can be observed that the amplitude stays at a high level for roughly one hour. Towards the end of this measurement, the amplitude seems to slightly drop. It is not clear so far whether this is caused by the pumping process or whether the NMR monitor is drifting. In Fig. (4.2.6) the precession frequency during the same run is plotted.

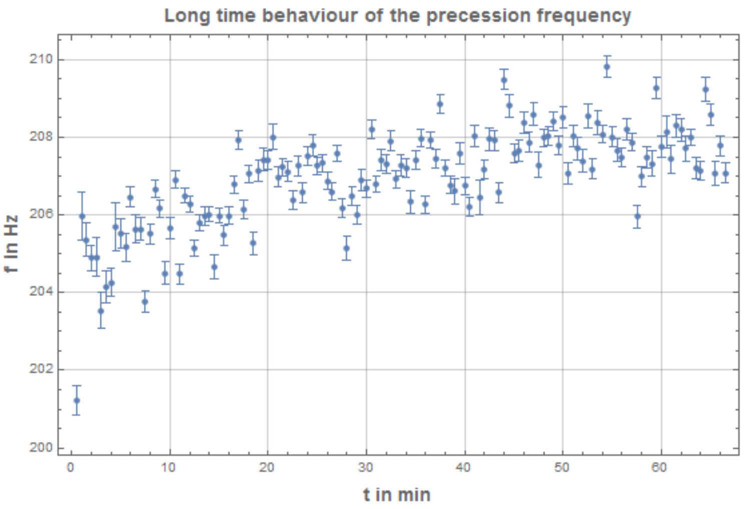

Figure 4.2.6: Small drift of the precession frequency during a long run of the polarizer obtained by fits

The precession frequency is a direct measure for the absolute magnetic field across the measuring volume. A drift of the precession frequency can change the amplitude of the measured signal because of the resonant circuit used in the NMR monitor. But as it is displayed in the diagram, the change in f_0 is roughly 2 Hz. This is very small compared to the resonance frequency f_R of 24.2 kHz. With the estimated Q factor of 73, the bandwidth $B = f_R/Q$ can be calculated to approx. 330 Hz. Therefore, it is not assumed, that the drift of the amplitude is caused by drifts of the magnetic field. It is rather suspected that temperature dependencies are responsible for this kind of behavior.

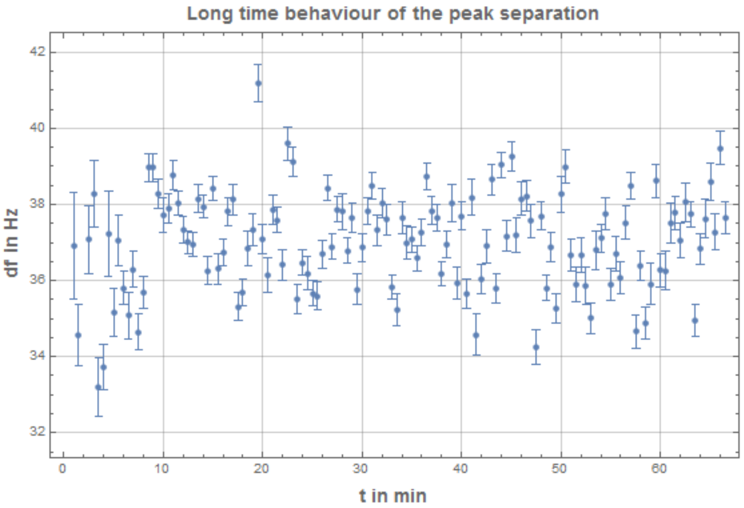

Figure 4.2.7: The frequency difference *df* of the two Fourier peaks is a measure of the gradient across the legs of the U profile.

Fig. (4.2.7) and Fig. (4.2.8) are showing the stability of magnetic field gradients. By monitoring df, the corresponding gradient is directly measured due to the separate legs of the U profile. The plot reveals that in this direction the gradient is rather constant in time. In contrast, the T_2 relaxation time of roughly 22 ms is changing visibly. For instance, between minute 35 and 45, a clear drift of the gradients becomes apparent. According to the time scale of 10 minutes, it is very likely that this process can be related to the MSR which is located in the neighboring room. When closing its door, the Mu-metal relaxes into an equilibrium state for several minutes. This, however, is not concerning because the amplitude of the NMR signal is not directly affected.

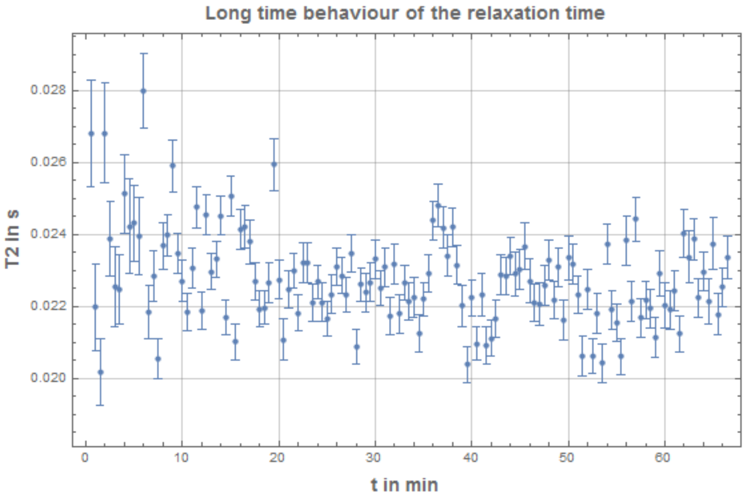

Figure 4.2.8: Transversal relaxation time T_2 of the xenon signal

4.2.3 Accumulation of HP ^{129}Xe

Having verified the long-term stability of the polarization values over one hour, the accumulation of the polarized xenon can be performed as explained in the section above. The whole process of accumulation takes one hour and yields to an amount of roughly 150 mbar·l. The volume into which the frozen xenon is expanded consists of the cold trap, the inner volume of the Tinanium block and the buffer cell which gives a total volume of 547 ml. The final pressure reaches around 270 mbar. After the expansion, there is no flow transporting polarized xenon through the NMR monitor. For this reason, only a single NMR shot can be acquired. But due to the higher xenon pressure, the signal is also larger.

In a first measurement, HP xenon gas was accumulated and expanded. After that, an NMR shot was taken and the xenon gas was frozen out again, by lifting up the dewar containing liquid nitrogen (see Fig. (4.1.23)). The monitored pressure during that process is shown in Fig. (4.2.9). When all xenon gas is frozen, the pressure goes down to nearly zero millibars. Then, the xenon is expanded again. The maximum pressure is reached when all xenon is in gas phase. After both expansions, the NMR signal was measured respectively. It is directly converted into a polarization value using the calibration which is presented in the next chapter of this thesis. For both cycles, polarization values of

$$P_1 = (18.4 \pm 0.3)\% \tag{4.2.3}$$

and

$$P_2 = (17.8 \pm 0.3)\% \tag{4.2.4}$$

were obtained. The relative loss between these two steps is only around 3% which is remarkably low considering the fact that in between the HP xenon is exposed to different magnetic fields and different temperatures yielding to different aggregate states.

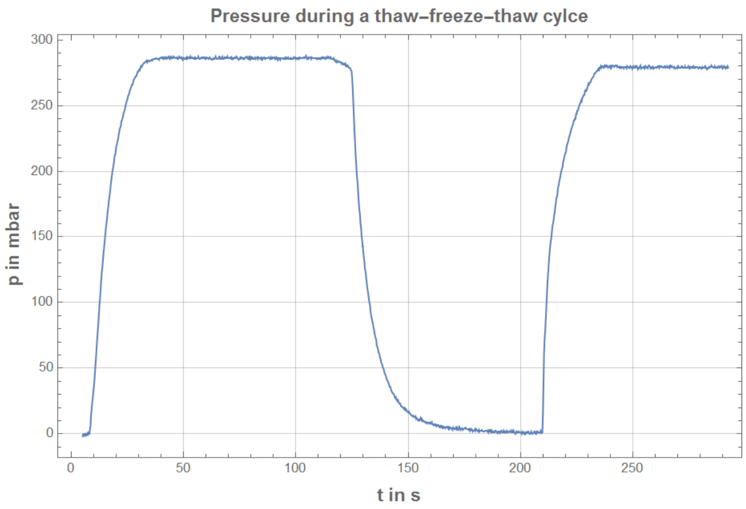

Figure 4.2.9: Pressure during re-thawing and re-freezing HP xenon.

In Tab. (4.2.3), the results of several accumulations are listed. Having the opportunity to measure the polarization before and after the accumulation process allows to quantify the overall polarization losses 1 - $P_{\text{out}}/P_{\text{in}}$. In standard operation, especially with a gas flow of 200 ml/min the polarization loss of roughly 30% is quite large compared to the previous result when repeating the thaw and freeze cycle. In [76], polarization losses of 5-10% during the accumulation were reported.

# Run	flow in ml/min	P_{in} in %	P_{out} in %	relative loss in %	t_{acc} in h
1	100	27.9 ± 2.4	8.4 ± 0.3	70	1
2	200	27.4 ± 3.8	18.8 ± 0.5	31	0.5
3	200	21.2 ± 2.0	14.6 ± 0.3	31	1
4	300	24.4 ± 1.7	14.3 ± 0.3	41	0.5
5	200	29.3 ± 2.6	18.1 ± 0.4	38	0.5

Table 4.2.1: Polarization losses for different accumulation cycles

In these measurements, the flow and the accumulation time t_{acc} were changed. For small flows, the polarization losses become very large. Going to higher flows seems to increase the losses as well. In run 2 and 3, only the accumulation time was doubled with no impact to the polarization losses. The last run (run 5) differs from the other because instead of lifting the liquid-nitrogen dewar in three steps, as it is usually done, it was lifted with constant speed by the use of a stepper motor. However, no obvious difference in polarization losses could not been observed. In order to identify the reason for these losses, several aspects have been considered.

One reason might be the rapidly changing magnetic field along the path into the Halbach magnet. Over a distance of 30 cm the magnetic field increases from 2 mT to 0.3 T. The simulated magnetic field components along the vertical path into the Halbach magnet is shown in Fig. (4.2.10).

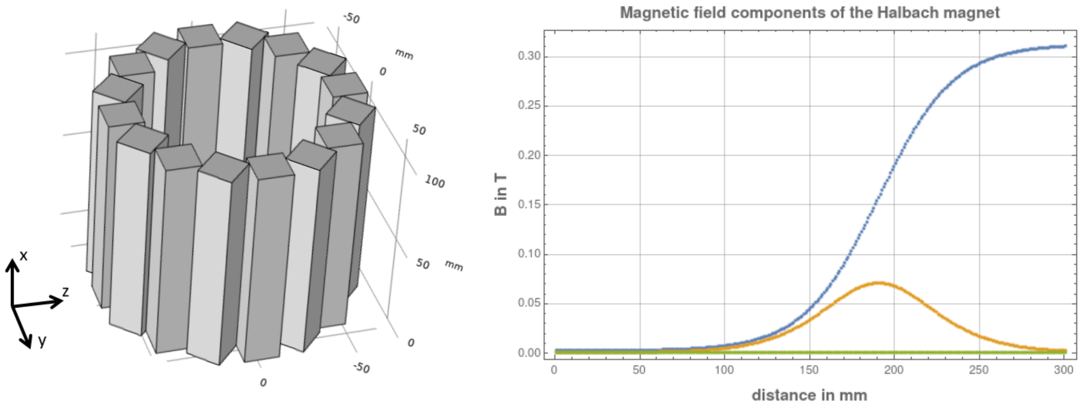

Figure 4.2.10: Left: Sketch of the Halbach magnet (mirrored for negative x). Right: magnetic field components along the path into the Halbach magnet (z=-15 mm, y=0). At t=0, B_z (blue) starts at 2 mT and reaches 0.3 T. Due to symmetry arguments, B_y (green) vanishes. Simulated values and graphic obtained from [77].

In Fig. (4.2.10, right), the center of the Halbach magnet is located at 300 mm, where the magnetic field is maximum. At 200 mm, the Halbach magnet begins. The B_x component is caused by the fact that the glass line runs not along the symmetry axis but has an offset of 15 mm in z direction. Assuming a constant velocity of the polarized xenon atoms flowing into the magnet, the field which is perceived becomes time dependent. In [4], it is shown how the Schrödinger equation for a spin-1/2 particle in an arbitrarily time dependent magnetic field (Eq. (2.2.3)) can be solved numerically or semi-analytically. Starting at t=0 (this corresponds to the left in Fig. (4.2.10)) with a fully polarized spin-up state, the time evolution in this specific magnetic field can be calculated and the polarization losses extracted. As estimated in the section above, the velocity of the flowing xenon is roughly 11.8 cm/s. To reach the center of the Halbach magnet, it would take around 2.5 s. At magnetic fields of 0.3 T, the precession frequency of xenon is in the order of MHz. It will become numerically very hard to resolve all these periods of the precession over that time. To simplify the numerical situation a bit, the overall magnetic field was scaled down by a factor of ten and both, the numerical and the semi-analytical routines, yielded to consistent results. It could be shown that the xenon polarization is preserved to 99.9% during the transition into the Halbach magnet. Even when the flow (velocity) is changed by a factor of ten, the result is the same. It is assumed that increasing the magnetic field by a factor of ten, further reduces the polarization losses because the time scale $\tau = B_0^{-1}\gamma^{-1}$ becomes smaller and therefore the system more adiabatic.

Comparing the experimental results to the outcome of the simulation, it can be deduced that another effect must be responsible for the polarization losses. Regarding the measurements in Tab. (4.2.3), a dependency of the flow rate is observed. Together with the repeating freeze and thaw measurement, it seems to be the case, that the polarization losses become smaller with increasing flow rate. When expanding and re-freezing the xenon, the flows are much larger than it would be the case during the accumulation. In the previous section when the accumulation system was introduced, it was emphasized that the temperature of the solid xenon affects the T_1 relaxation time significantly. Comparing the freezing process of the Xe/He/N_2 gas mixture during accumulation with the re-freezing of pure xenon it should be noted that in the latter case the xenon reaches the low temperature of the liquid nitrogen much faster. On the other hand, reducing the flow as it was done in run 1 should also yield to a better cooling behavior of the xenon and buffer gases which does not reflect the large losses which are observed.

Another reason for the observed polarization losses can be relaxation processes like wall relaxation which occur in a specific region along the path into the Halbach magnet. The longer the residence time of the spins in that critical region, the higher the losses will become.

To conclude this section, it has to be admitted that the origin of the polarization losses remains unknown. Further examinations are necessary to identify the reasons. One approach would be to measure the magnetic field along the trajectory of the flowing xenon into the Halbach magnet. Instead of using simulated magnetic field values, the calculation solving the Schrödinger equation can be re-done with actual measurements. Furthermore, the measurements in Tab. (4.2.3) should be repeated in more detail in order to check the flow dependency. It should be noted that after expanding the xenon, only one NMR shot determines the corresponding polarization value. In the next section, it is explained how T_1 is measured performing several NMR shots at different times. This procedure could have been applied successively in these measurements in order to increase the statistics. Finally, the measurement using a stepper motor to lift up the liquid-nitrogen dewar was a single qualitative test. Systematic measurements using different speeds might also provide further hints.

Due to time constraints, all these detailed examinations have not been done yet. It has to be highlighted that the ability to produce 150 mbar·l of HP xenon with a polarization of 19% is already a huge establishment. It allows for first systematic measurements within the MSR which are presented in chapter 6.

4.2.4 T_1 measurement of the buffer cell

A final measurement with the polarizer, before it was used to produce xenon gas to be transferred into the MSR, was the determination of the storage time T_1 of the buffer cell mounted on the titanium block. After HP xenon gas was thawed and expanded into the buffer cell, the idea is to take several single NMR shots at different times to measure the decay of the polarization signal. Starting with the buffer cell filled by xenon with a pressure of roughly 270 mbar, two volumes are regarded: the first one is the volume of the buffer cell itself, the other one is given by the inner volume of the titanium block and the measuring volume of the NMR monitor. Additionally, connection lines are contributing to that volume as well. It is desired that the volume of the buffer cell is much larger than the second volume. The arrangement of the volumes and the valves is sketched in Fig. (4.2.11). For the names of the valves refer to Fig. (4.1.1) and Fig. (4.1.21).

A measurement cycle is following the same procedure: initially, the buffer cell contains HP xenon gas with VTBBUF closed. The second volume is evacuated by the turbo pump with VTBVAC opened. VCIN is always closed during this measurement. When the volume is evacuated, VTBVAC is closed and VTBBUF is opened and the xenon gas expands into the second volume. When the pressure reaches an equilibrium VTBBUF is closed again, and a single NMR shot is taken. After the acquisition, the volume is evacuated again and the next cycle may begin.

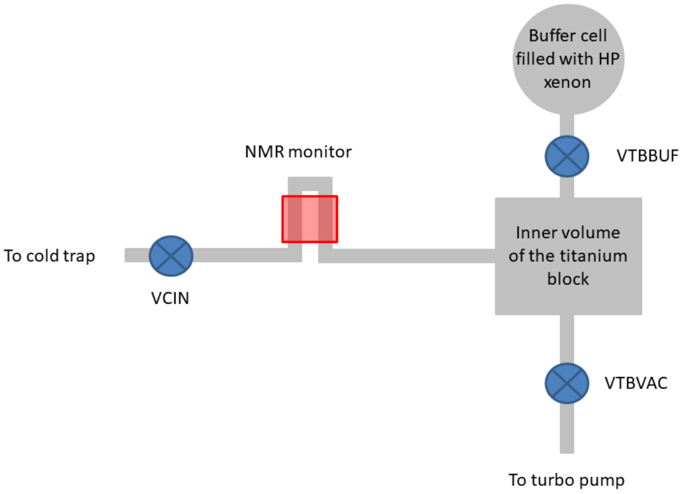

Figure 4.2.11: Schematic of all valves and sub volumes that are relevant for the T1 determination of the buffer cell.

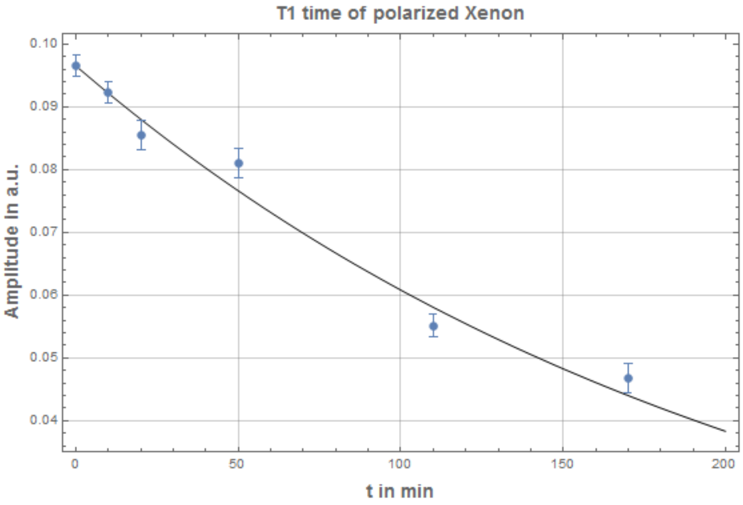

Figure 4.2.12: Measurement of the longitudinal relaxation time T_1 of the buffer cell.

Repeating this cycle at different times allows to measure T_1 for the xenon gas within the buffer cell. When plotting the measured amplitudes against time, they have to be corrected by the pressure. The more cycles are performed, the smaller the pressure and therefore the signal becomes. For this reason, it was decided to take only 6 data points, as shown in Fig. (4.2.12). To these data points, an exponential function was fitted giving a decay constant of

$$T_1 = (217 \pm 11)\ \text{min} \tag{4.2.5}$$

which is more than 3.5 hours. Regarding the fit, it becomes apparent that significant deviations occur. This can be explained by the fact that only one NMR shot can be performed because the destroyed polarization cannot be restored anymore. Comparing the measured T_1 to the maximum possible T_1 for pure xenon of $T_{1,\text{vdW}} = 4.6$ h (see chapter 2), the difference is quite small. Other mechanisms affecting the measured T_1 are the wall relaxation and the interaction with oxygen. Relaxation due to gradients or due to binary collisions can be neglected. Plugging in the magnetic field of 2.01 mT, a gradient of 2µT/cm, a cell radius of 5 cm and a pressure of 270 mbar will yield to T_1 relaxation times which are much longer than the one measured. By

$$T_1^{-1} = T_{1,\mathrm{vdW}}^{-1} + T_{1,\mathrm{wall}+O_2}^{-1} \quad , \tag{4.2.6}$$

the combined T_1 relaxation due to the wall and oxygen can be calculated to 16.6 h which is pretty close to the maximum observed wall-relaxation time for xenon gas of 18 h [25].

The long T_1 relaxation time allows for a certain flexibility regarding the experimental procedure. Before the polarized xenon is transferred into the MSR to be measured, many other steps apart from the polarization process have to be fulfilled in parallel. It turned out to be very beneficial to have opportunity to wait a few minutes until the xenon gas is shot into the MSR.

4.2.5 Operating the Laser

During several runs, a good reproducibility was observed. This was achieved by monitoring several parameters during the polarization process. The most important one is the transmitted laser power after the optical pumping cell. It is a measure of how much power is absorbed by the rubidium gas. This quantity depends on the primary power and the wavelength of the laser beam and the amount of rubidium within the optical pumping cell. The transmitted laser power during the long run shown in the previous section was monitored as well and can be observed in Fig. (4.2.13).

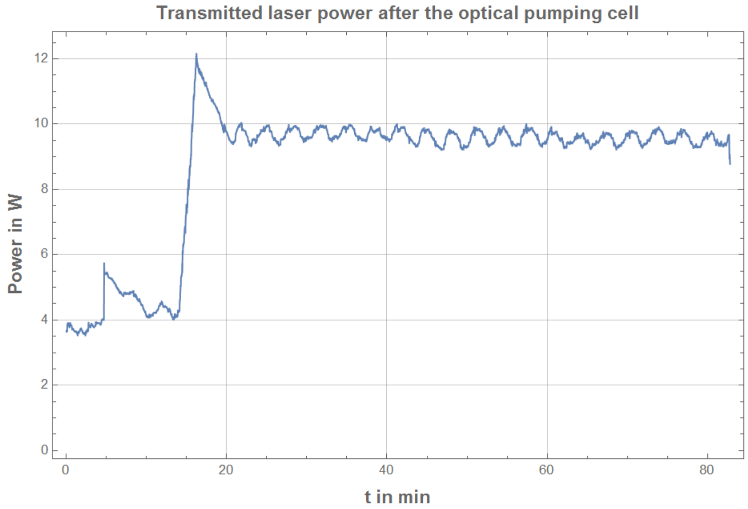

Figure 4.2.13: Transmitted laser power after the optical pumping cell.

From the plot, it can be recognized that the primary laser power was kept small in the first minutes to reach an equilibrium in temperature. After that, the laser power was ramped up to 53 W (I=45 A). For each polarization cycle the transmitted laser power was around 10 W. So, this value is a good indicator whether the polarization process is working as expected. Especially at high laser power, a periodic behavior of the transmitted laser power is measured. The period is roughly 3.5 minutes. The changes of the transmitted power seem not to directly affect the measured xenon polarization. In Fig. (4.2.5), no such modulation in the signal can be observed. The origin of the modulation of the transmitted laser power is not yet fully understood. It could be excluded that the primary laser power changes with time. Locating the power meter in front of the optical pumping cell yielded to a constant power, without such a modulation. For this reason, two opportunities are possible. The first one is that the temperature control of the pre-saturator for adapting the vapor pressure of the rubidium might be unstable. It is a simple two-point controller with a hysteresis of 2 K. A changing temperature may cause a variable number density of rubidium and therefore a different absorption behavior. Unfortunately, this temperature is not monitored yet. Otherwise, it would be easy to find a correlation if this effect is responsible for these observations. Nonetheless, in the future, the control algorithm should be replaced by a PID controller with the opportunity to monitor both, the measured and the set temperature. A second approach to explain the observed behavior of the transmitted laser power could be a changing wavelength of the primary laser beam. In the user manual of the laser, it is recommended that the laser is water-cooled to a temperature of 18°C. As it is shown in Fig. (4.2.14), the temperature is slightly above the recommendation.

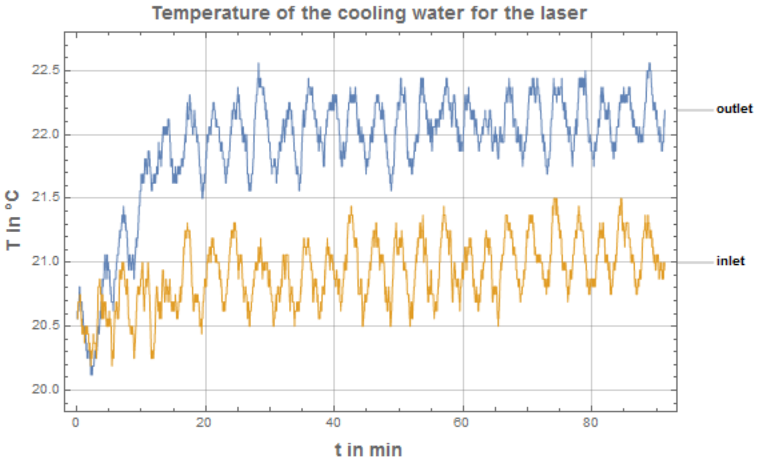

Figure 4.2.14: Temperatures of the cooling water at inlet and outlet of the laser.

The temperatures of inlet and outlet were measured by gluing temperature-sensor ICs (DS18S20, Dallas Semiconductor) to the metallic terminals connecting the water tubes with the housing of the laser head. When turning the laser on, the water temperature of the outlet rises as expected. However, in both terminals an oscillation of the temperature is observed. It is assumed, that the chiller which cools the water down to the desired temperature is not working stable as well. At first glance, the oscillation of the cooling-water temperature seems to match with the oscillations in the transmitted laser power. Further examinations, however, could not reveal a correlation between both. The measurements of the water temperature were performed after the variation of the power became apparent. Depending on the room temperature the oscillation behavior of the water may change.

When the chiller is turned on, the room temperature rises to over 30°C in summer, which is much too high. The reason for this is that the heat power taken out from the water is blown into the air by a big fan. Furthermore, the coils producing the magnetic holding field are also contributing to the increase of the room temperature. To this point, it can be summarized that the conditions under which the laser is operated are not optimal. Usually, the lab is cooled to a fixed temperature with an accuracy of at least 1 K. First steps would be to cool down the coils and to replace the chiller with another one which transfers the heat power into a separate cooling-water system, instead of heating the lab.

Chapter 5

Calibration of Xenon polarization

Having established the polarization process for the xenon gas, it would be desirable to quantify the polarization of it. The basic idea is to measure the NMR signal of a thermally polarized water sample. The polarization can be estimated by the Boltzmann factor. In order to calibrate the setup, the measuring volume has to be identical to the volume used for xenon NMR. Therefore, an additional U-profile was constructed with an identical B_1 coil. The number of turns, length and resistance of the coils were checked and matched to each other.

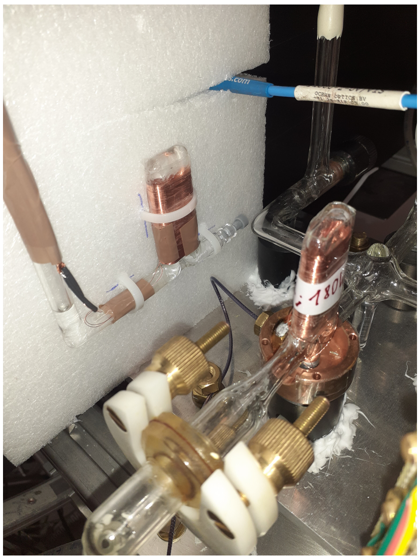

Figure 5.0.1: Two identical NMR probes are manufactured in order to calibrate the NMR signal of the xenon.

The calibration will be meaningful only if the same resonance circuit is used. For this reason, the precession frequency is kept constant by reducing B_0 by a factor $\gamma_{\mathrm{p}}/\gamma_{\mathrm{xe}} \approx 3.6$ where the index p stands for the protons contained in the water sample. This procedure was also applied in other projects, e.g. in [78] and [79]. In the following sections, the process of calibration is presented in full detail.

5.1 Theoretical model

Before the NMR signals of water is measured, some theoretical aspects should be discussed. In chapter 2 it was shown, how spins in a homogeneous magnetic field B_0 can be manipulated by RF pulses. Using the rotating-wave approximation, the time evolution operator $U(t)$ can be calculated. The final spin state after the RF pulse is obtained by applying $U(t)$ to the initial spin-up state $|\uparrow\rangle = (1,0)^T$. In order to write down $U(t)$, the following parameters must be given: B_1, B_0, ω, Δt and ϕ (compare to equation (2.2.4)). In the measurements, B_0 will be chosen and kept fixed such that the Larmor frequency γB_0 matches the resonance frequency of the LC circuit. Δt is also kept fixed to 1ms. When assuming a sinusoidal B_1 signal, its phase ϕ can be set to zero. So, the B_1 amplitude and the excitation frequency ω are the only two parameters which are changed for measurements.

However, not a single spin is considered but an ensemble of roughly 10^{23} spins which are distributed across the measuring volume. The goal is to calculate the voltage signal induced by the flipped spins which is measured by the pickup coil. The same coil is also used to apply the B_1 field to the sample. Due to its geometry the B_1 field is not very homogeneous across the measuring volume. A quick simulation in Radia shows that the B_1 field varies up to a factor of two.

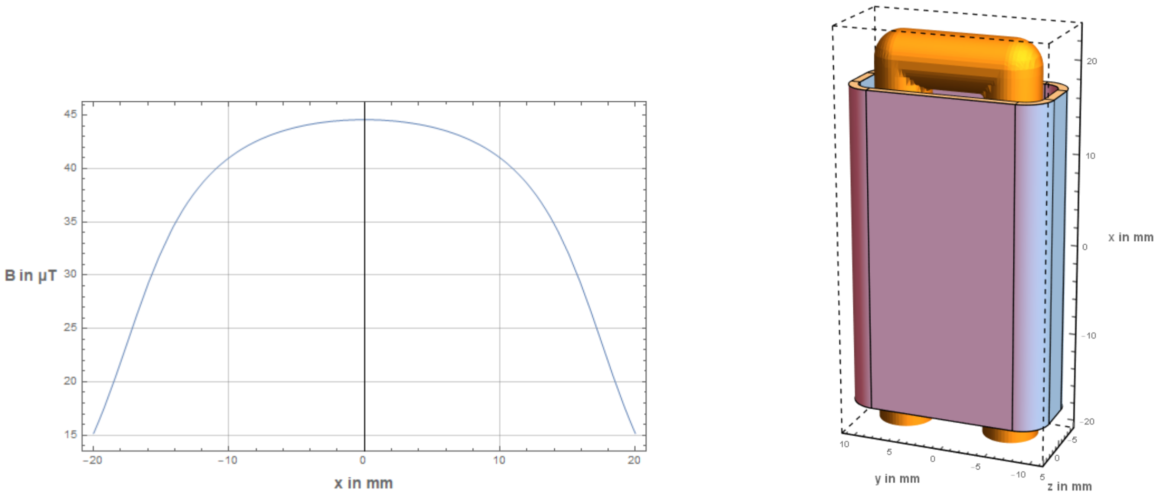

Figure 5.1.1: Left: B_1 field along the symmetry axis simulated for a current of 7.5 mA. Right: measuring volume embedded into the B_1 coil.

The consequence is that some spins are flipped as expected whereas other spins are not. Furthermore, the signal can be damped due to a distribution in phase. To account for these effects the following strategy was worked out:

1. Equally sample N spin positions across the measuring volume and calculate the B_1 field in each sampling point.
2. Calculate the flip angle and the phase after the RF pulse using the time-evolution operator $U(t)$.
3. Correct the magnitude of the signal by the spatially dependent response function of the pickup coil.
4. Take the phase-weighted sum of all spin contributions to obtain the overall voltage signal.

In the first step, a cube was defined which enclosed the whole measuring volume. It is very easy to equally sample that cube. Then only the samples are kept which are contained within the measuring volume. In the following, the number of sampling points N was chosen to be 1000. In each sampling point the magnetic-field vector of the B_1-coil for a current of 7.5 mA was calculated. This first step has to be done only once, because the current can be linearly scaled to arbitrary magnetic field magnitudes in the afterward.

In the second step, the spin-flip is calculated using $U(t)$. For this purpose, several approximations are used. In the beginning, it was assumed, that the guiding field B_0 is homogeneous over the measuring volume and points into z direction. As B_1 amplitude, only the transverse components were regarded by adding them quadratically. The longitudinal z component of B_1 slightly changes the B_0 field periodically during the RF pulse yielding to a small frequency shift of quadratic order which can be neglected. What cannot be neglected is the phase introduced by the B_1 field. For different positions, the transverse projection may point into different directions within the yz plane. Therefore, additional phases ϕ_{mag} will occur damping the overall signal. After the RF pulse, the flip angle θ and the flipping phase ϕ_{flip} are extracted from the flipped state

$$|\Psi(\Delta t)\rangle = U(\Delta t)\,|{\uparrow}\rangle \quad . \tag{5.1.1}$$

By taking the expectation value of the Pauli matrices, the x,y,z components of the flipped spin vector can be extracted:

$$S_i = \langle\Psi(\Delta t)|\,\sigma_i\,|\Psi(\Delta t)\rangle \quad . \tag{5.1.2}$$

The flip angle θ is obtained by

$$\theta = \arccos\left(\frac{S_z}{\sqrt{S_x^2+S_y^2+S_z^2}}\right) = \arccos(S_z) \tag{5.1.3}$$

and the flipping phase by

$$\phi_{\text{flip}} = \arctan\left(\frac{S_y}{S_x}\right) \tag{5.1.4}$$

This procedure can be applied to all sampling points. But before the average can be taken, it has to be noted that the response of the pickup coil to a precessing spin depends on its position.

In step three this response function of the coil is calculated. Starting point is a single rectangular turn of the B_1 coil. It lies in the yz plane at position x'. The dimensions in z direction a are 8 mm and in y direction b 20 mm. The question is: What voltage $V_T(t, x')$ is induced by a precessing spin at position $\vec{x}_0$? This is answered by Faraday's Law:

$$\begin{aligned} V_T(t,x') &= -\frac{d}{dt}\Phi(t) && (5.1.5)\\ &= -\frac{d}{dt}\int_A \vec{B}d\vec{f} && (5.1.6)\\ &= -\int_A \nabla \times \frac{d}{dt}\vec{A}d\vec{f} && (5.1.7)\\ &= -\oint_{\partial A} \frac{d}{dt}\vec{A}d\vec{s} && (5.1.8) \end{aligned}$$

where in the last step, Stokes's theorem was used to convert the surface integral into a line integral. According to [49], the vector potential of a magnetic dipole is given by:

$$\vec{A}(\vec{x}) = \frac{\mu_0 \vec{m}(t)}{4\pi} \times \frac{(\vec{x}-\vec{x}_0)}{|\vec{x}-\vec{x}_0|^3} \quad . \tag{5.1.9}$$

Here, the magnetization vector $\vec{m}(t)$ defines the orientation of the spin with respect to time:

$$\vec{m}(t) = m_0 \begin{pmatrix} \sin(\theta)\sin(\omega t+\phi) \\ \sin(\theta)\cos(\omega t+\phi) \\ \cos(\theta) \end{pmatrix} \quad . \tag{5.1.10}$$

Plugging the expressions for $\vec{A}(\vec{x})$ and $\vec{m}(t)$ into the line integral, an analytic expression of the induced voltage can be obtained:

$$\begin{aligned} &V_T(t,x') = \\ &\frac{m_0\mu_0\omega\sin(\theta)}{8\pi} \times \{ \\ &-\frac{(a-2z_0)\sin(\omega t)}{\alpha - az_0 - y_0^2}\left(\frac{0.5b-y_0}{\sqrt{\alpha-by_0-az_0}}+\frac{0.5b+y_0}{\sqrt{\alpha+by_0-az_0}}\right)\\ &-\frac{(a+2z_0)\sin(\omega t)}{\alpha + az_0 + y_0^2}\left(\frac{0.5b-y_0}{\sqrt{\alpha-by_0+az_0}}+\frac{0.5b+y_0}{\sqrt{\alpha+by_0+az_0}}\right)\\ &+\frac{(x_0-x')\cos(\omega t)-(0.5b-y_0)\sin(\omega t)}{\alpha - by_0 - z_0^2}\left(\frac{0.5a-z_0}{\sqrt{\alpha-az_0-by_0}}+\frac{0.5a+z_0}{\sqrt{\alpha+az_0-by_0}}\right)\\ &+\frac{(x'-x_0)\cos(\omega t)-(0.5b+y_0)\sin(\omega t)}{\alpha + by_0 - z_0^2}\left(\frac{0.5a-z_0}{\sqrt{\alpha-az_0+by_0}}+\frac{0.5a+z_0}{\sqrt{\alpha+az_0+by_0}}\right)\\ &\} \end{aligned} \tag{5.1.11}$$

with

$$\alpha = 0.25a^2 + 0.25b^2 + x_0^2 - 2x_0x' + x'^2 + y_0^2 + z_0^2 \quad . \tag{5.1.12}$$

For simplicity, the phase ϕ of $\vec{m}(t)$ was set to zero. This expression consists of four contributions from the four sections of the turn. To obtain the overall induced voltage

V(t) of a single precessing spin, the expression $V_T(t,x')$ needs to be integrated along the length of the pickup coil which is c=35 mm:

$$V(t) = \frac{1}{c}\int_{-c/2}^{c/2} V_T(t,x')dx' \quad . \tag{5.1.13}$$

This integral needs to be calculated numerically due to the complexity of the expression of $V_T(t,x')$ for all different positions $\vec{x}_0$ of the sampled spins. It should be emphasized that not only the amplitude but also the phase of the precessing-spin signal changes with position $\vec{x}_0$. When calculating the integral above, it is beneficial to integrate the cosine and the sine parts separately to extract the amplitude and the phase difference ϕ_{ind}.

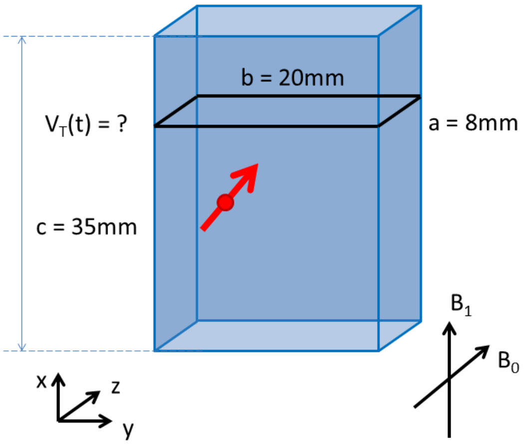

Figure 5.1.2: Orientation of a turn with respect to the precessing spin.

Finally, in step four, all induced voltages of all sampled spins are added together taking into account the phase differences $\Delta\phi$:

$$\Delta\phi = \phi_{\text{mag}} + \phi_{\text{flip}} + \phi_{\text{ind}} \quad . \tag{5.1.14}$$

The obtained final value corresponds to the strength of the measured NMR signal with a certain setting of the B_1 amplitude and an excitation frequency ω. For a different setting, the whole calculation has to be repeated. Fortunately, only step two depends on B_1 and ω and needs to be recalculated. Using the same sampling points the results of step three can be reused by rescaling with the new ω. The absolute value of the NMR signal is hard to calculate because it depends also on the read-out electronics. However, only relative dependencies of B_1 and ω are of interest. When comparing the result to real measurements, an overall amplitude is defined which can be fitted to the data.

5.2 Measuring the NMR signal of water

In a first step, 1.58 g $CuSO_4$ was dissolved in one liter of distilled water which was filled into the NMR measuring volume. The effect of copper sulfate is the reduction of the T_1

relaxation time of the water sample which is usually between three and four seconds. In the used composition, T_1 was measured to be roughly 100 ms [77]. The advantage of a shorter T_1 is a faster repetition time between two NMR measurements.

When performing first NMR shots, the magnetic B_0 field was reduced by a factor of 3.6 to match the resonance frequency of the LC circuit. The probe volume was located next to the xenon-NMR monitor as shown in Fig. (5.0.1). After performing several B_0 sweeps without observing any signal, it was decided to change the location of the probe. Near the xenon-NMR monitor, a field gradient of few µT/cm is present. To that point, it was not clear how sensitive the water sample is to gradients and what T_2 relaxation time has to be expected. For this reason, a separate coil system was used to produce a ten times more homogeneous magnetic B_0 field than used before. The whole setup consists of five ring coils wound around bicycle rims. They are mounted in the same way as it was done for coil system producing the holding field of the polarizer. In order to reduce the noise level, the center is enclosed by a housing of aluminum. Fig. (5.2.1) shows the absolute magnetic field along the symmetry axis and its homogeneity. It can be observed, that the hall sensor (AK8963, AsahiKasei) which was used is operated at its noise limit of 0.1 µT. The asymmetry of the field dependency shows that background fields are contributing.

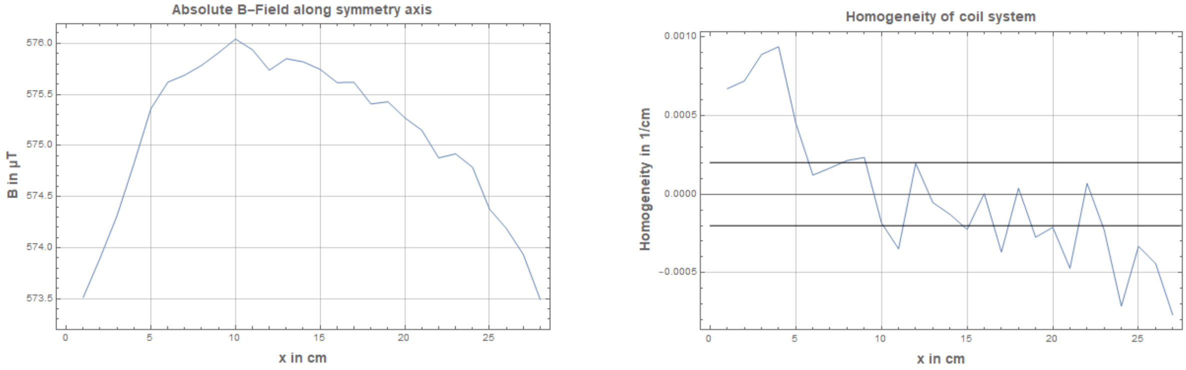

Figure 5.2.1: Left: Magnetic field along the symmetry axis of the new coil system. Right: corresponding homogeneity.

The probe volume is located at the position with the best field homogeneity (x=15 cm, in Fig. (5.2.1)). To find an NMR signal of the water probe, the B_0 field was swept around the expected value. It turned out that the trick is not to increase the field homogeneity (as it was assumed previously) but to increase the number of scans during averaging. When the first NMR signal of the water probe was measured, each run was averaged 20000 times. In Fig. (5.2.2) first measurements of the water signal are shown.

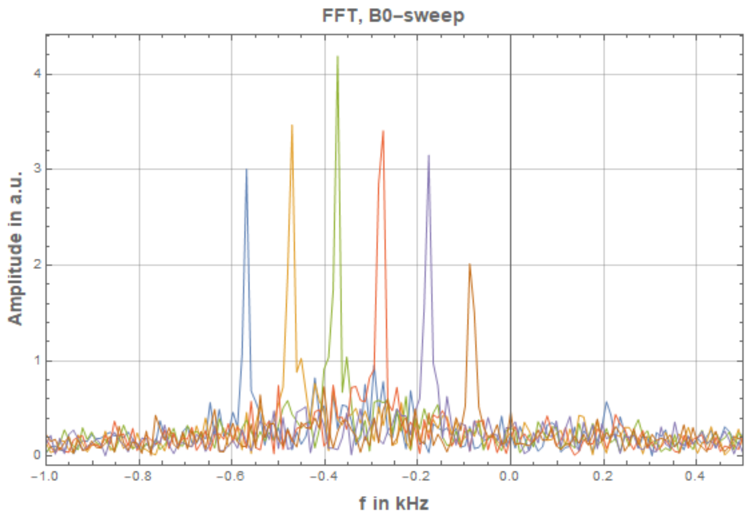

Figure 5.2.2: The B_0 sweep shows a dependency of the amplitude caused by the resonance circuit.

After the B_0 sweep, B_0 was set to the value yielding maximum amplitude. The quantitative analysis was performed in the same way as presented in the chapter before. Here, only one frequency component was regarded, due to the low gradients, i.e. $a_2{=}df{=}0$ in equations (4.2.1) and (4.2.2). In the Fourier spectrum, no double peaks could be observed.

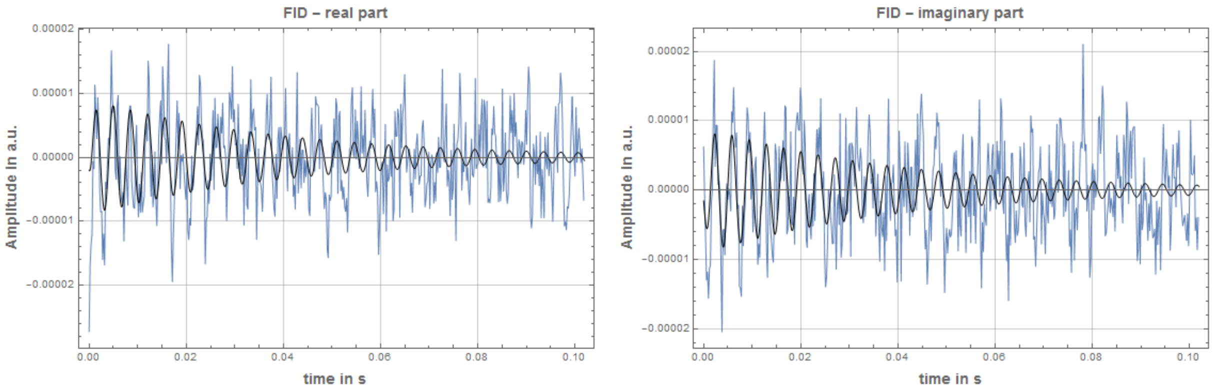

Figure 5.2.3: Simultaneous fit of real and imaginary parts of the water FID.

Especially in this measurement, the idea of fitting real and imaginary part simultaneously became very relevant due to the low signal-to-noise ratio. When fitting both components separately, the fitter will have difficulties to find the global minimum. Therefore, the known phase shift of both signals is an important information which can be used by fitting simultaneously.

When calibrating the xenon-NMR signal an over estimation should be avoided. For this reason, it is important to measure the maximum NMR signal of the water sample because a lower water signal will yield to higher xenon signals when performing the calibration. One effect which may reduce the measured amplitude of the water signal is the drift of the B_0 field. When performing one measurement with 10000 averages with a rate of 300 ms, this would take roughly one hour. During this time B_0 and therefore f_0 might drift. Averaging over these drifts will yield to a de-phasing over time and the amplitude decreases. To be less sensitive to that effect, it was decided to divide such a measurement into 10 measurements of 1000 shots which are averaged separately. In this way, one has the opportunity to check for B_0 drifts and correct for them, if needed.

To obtain the maximum NMR signal of the water sample, sweeps of B_1 with two different detunings (50 Hz and 270 Hz) were performed. The blue line clearly reveals the different flip angles: the first maximum corresponds to 90°, the first minimum to 180° and so on. In the theoretical model, the only unknown was the global amplitude. All other parameters are known and plugged in. In a fit with a free global amplitude, the maximum amplitude of the water signal can be extracted. The maximum value of the theoretical model at a B_1 current of roughly 5 mA was normalized to one, such that the fit result returns the amplitude with the corresponding statistical error:

$$S_p^0 = (1.08 \pm 0.02) \cdot 10^{-5} \quad . \tag{5.2.1}$$

The units of this result are arbitrary and depend on the settings of the spectrometer. When comparing this signal to the xenon signal, it is important to use the same settings or, at least, to know the conversion factor between the units very well. They can be obtained by applying a fake signal to the pickup coil with a function generator and measuring it using different spectrometer settings.

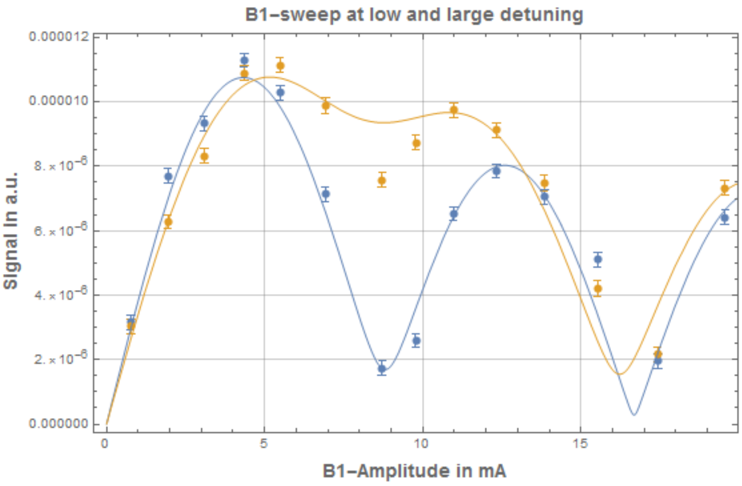

Figure 5.2.4: Two B_1 sweeps at different detunings (orange: 270 Hz, blue: 50 Hz) with the theoretical expectation.

One final remark should be made regarding the measurement cycle: it was stated that the repetition time T_R between two NMR shots was chosen to be 300 ms whereas the T_1 relaxation time was measured to be roughly 100 ms. After a spin-flip of angle θ, T_1 is the time scale, when the thermal equilibrium of the spins is reached, i.e. when the magnetization $\vec{M}(t)$ is again aligned with $\vec{B}_0$. If $\vec{M}(t)$ is not fully aligned but the flip (e.g. by 90°) is already performed, the longitudinal component will be smaller than the total absolute magnetization M_0. Performing several successive NMR shots, an equilibrium of the longitudinal magnetization will establish. In [80] it is derived that this equilibrium is given by:

$$M_{\mathrm{z,e}} = \frac{M_0(1-\exp(-T_R/T_1))}{1-\exp(-T_R/T_1)\cos(\theta)} \quad . \tag{5.2.2}$$

Setting θ to 90°, only the nominator is left. After a 90° flip $M_{\mathrm{z,e}}$ corresponds to the observed transverse magnetization. In the measurements above $T_R/T_1 = 3$, therefore the observed magnetization is smaller than M_0 by a factor of $\exp(-T_R/T_1) \approx 5\%$. If $T_R = 5T_1$ this factor would be 0.7%. However, the total time during a measurement run would also increase with the risk of being more susceptible to drifts in B_0. Due to these considerations, the obtained signal S_p^0 needs to be corrected by a factor of 5%:

$$S_p = (1.13 \pm 0.02) \cdot 10^{-5} \quad . \tag{5.2.3}$$

5.3 Calibration

The strategy to perform the calibration of the xenon-NMR signal is to calculate the magnetization of a thermally polarized water sample at room temperature. Then, the same is done for a gaseous sample of xenon with a polarization of 100%. Taking the ratio of both magnetization values allows to compare with the measured values. According to equation (2.1.10), the thermal polarization of water is given by

$$P_p = \tanh\left(\frac{\hbar\gamma_p B_0}{2k_B T}\right) = (1.896 \pm 0.007) \cdot 10^{-9} \tag{5.3.1}$$

where a temperature of (300 ± 1) K and a magnetic field of (557 ± 1) µT was inserted. To calculate the magnetization, the proton-number density of the water sample has to be determined. It has to be noted that each water molecule contributes with two protons and has a specific weight of 18 g/mol. With this information, the number density is calculated to $n_p = 6.693{\cdot}10^{-28}$ 1/m^3. With equation (2.1.11) the magnetization is given by

$$\begin{aligned} M_p &= n_p \cdot P \cdot \mu && (5.3.2) \\ &= n_p \cdot P \cdot \hbar\gamma_p I && (5.3.3) \\ &= (1.790 \pm 0.007) \cdot 10^{-6}\ \mathrm{A/m} && (5.3.4) \end{aligned}$$

Doing the same with the xenon sample requires to calculate the number density using the ideal gas equation:

$$\begin{aligned} n_{\mathrm{Xe}} &= \frac{N}{V} = \alpha \frac{p}{k_B \cdot T} && (5.3.5) \\ &= (1.274 \pm 0.008) \cdot 10^{23}\ \frac{1}{\mathrm{m}^3} && (5.3.6) \end{aligned}$$

where p = (20.0 ± 0.1) mbar is the partial pressure of xenon within the gas mixture and $\alpha = 26.4\%$ is the fraction of ^{129}Xe isotopes within the natural xenon gas used when measuring. The temperature was again assumed to be (300 ± 1) K. Now, the magnetization of a fully polarized xenon sample can be calculated:

$$\begin{aligned} M_{\mathrm{Xe}} &= n_{\mathrm{Xe}} \cdot P_{\mathrm{Xe}} \cdot \mu_{\mathrm{Xe}} && (5.3.7)\\ &= n_{\mathrm{Xe}} \cdot 1.0 \cdot \hbar\gamma_{\mathrm{Xe}} I && (5.3.8)\\ &= (4.97 \pm 0.03) \cdot 10^{-4}\ \mathrm{A/m}\quad . && (5.3.9)\end{aligned}$$

With the obtained values of M_p and M_{Xe} measured signals can be compared. Attention must be paid to the different T_2 relaxation times. When stating a polarization value of an NMR signal, it is related to the maximum signal right after the Pi/2 flip. In the measurements of both, xenon and water signals an acquisition delay of $\Delta t = 2$ ms was chosen. In Fig. (5.2.3), for instance, the time t=0 corresponds to the start of the acquisition which is delayed by Δt. The polarization of a xenon-NMR signal is given by:

$$P_{\mathrm{Xe}} = \frac{M_{\mathrm{p}}}{M_{\mathrm{Xe}}} \cdot \frac{\exp(\Delta t/T_{2,\mathrm{Xe}})}{\exp(\Delta t/T_{2,\mathrm{p}})} \cdot \frac{S_{\mathrm{Xe}}}{S_p} \quad . \tag{5.3.10}$$

Going back to the previous chapter, in Fig. (4.2.5) the NMR-signal amplitudes of the xenon gas are shown. From this plot one may read off an amplitude S_{Xe} of $(1.1 \pm 0.1)\ \times 10^{-3}$ units. The units are the same, as used for the water NMR measurements. The relaxation time $T_{2,\mathrm{Xe}}$ is shown in Fig. (4.2.8) and can be determined to (22 ± 1) ms. For the water signal, $T_{2,\mathrm{p}}$ can be also extracted by fits (see Fig. (5.2.3)) and was found to be (44 ± 4) ms. With these values, a xenon polarization of

$$P = (37 \pm 3)\% \tag{5.3.11}$$

is obtained.

On one hand, the procedure to calibrate the xenon signal is very clear. On the other hand, there are some systematics which are not fully understood yet. In case of the xenon gas, there is a constant flow during the NMR acquisition. It can be calculated that a xenon spin needs roughly one second to cross the whole measuring volume which is much longer than the T_2 relaxation time of 22 ms. Therefore, the static situation without flow was assumed which is true for the water sample. However, it is not known to what limit this approximation holds for the xenon, and under which circumstances the flow has to be considered. Secondly, the two probes of xenon and water are examined in different aggregate states. It is not fully clear whether the considerations which were made to understand the flip efficiency can be used interchangeably for the gaseous or liquid probes. One improvement will be to reduce the complexity of the measuring volume by going from a U profile to a simple cylindrical volume.

All in all, the calibration measurements provide a rough live estimate of the flowing xenon polarization and allows to reveal eminent information regarding polarization losses. Especially the freeze and thaw cycle can be examined very detailed and the transfer of the HP gas into the MSR is simplified significantly. It is very helpful to know the primary polarization before the transfer. When optimizing the parameters of the polarization process, in principle, the relative NMR signal is also sufficient. But it makes a difference when starting from 3% or 30% absolute polarization. In this context, the calibration was also very helpful.

Chapter 6

Spin precession within the MSR

Parts of this chapter have been worked out in collaboration with Josef Tremmel and are also published in his master's thesis [81].

This chapter describes the final result achieved in this work and combines all preparations done in the chapters before. HP xenon can be transferred into the MSR for being measured with the SQUID system. These experiments provide important information about the systematics of the setup and, most interestingly, about magnetic field gradients. In the first section, the experimental procedure and setup is introduced. Then, after the data-evaluation routine is explained, first results are presented.

6.1 Experimental procedure and setup

In the sections above it was explained how HP xenon is produced. When the polarization process is finished, the gas is stored in the buffer cell connected to the titanium block. To perform measurements within the MSR, the gas has to be transferred into the measurement cell which is also a spherically symmetric cell made from GE-180 glass. In principle, it is possible to connect the measurement cell to the titanium block to be filled with the xenon gas. In [82], it is shown that in this way, HP xenon can be stored and transported for several hours. However, to locate the glass cell at the center of the MSR, one has to open its door to have access. When the door was opened the MSR needs to be degaussed to remove the remnant magnetization yielding to high residual magnetic fields (and gradients). It turned out that the polarization of the gas does not survive the degaussing process. For this reason, a more sophisticated way of transferring the polarized gas into the MSR without opening its door has to be found. Already in previous experiments of this working group [83], [12] this problem was solved by a so-called transfer line. It is a copper tube with an outer diameter of 6 mm and an inner diameter of 4 mm connecting the readily installed measurement cell within the MSR and the titanium block of the xenon polarizer. In Fig. (6.1.1) a sketch of all components is provided.

In this sketch, it is shown how the transfer line connects the titanium block, the measurement cell and the recovery system. The line can be pumped by the turbo pumps of the titanium block and of the recovery system. The recovery system can be disconnected from the transfer line with the manual valve VREC which is made of glass. The measurement cell can be also disconnected by a pneumatic valve which is controlled outside the MSR. To preserve polarization, all materials should be non-magnetic and fluctuating magnetic

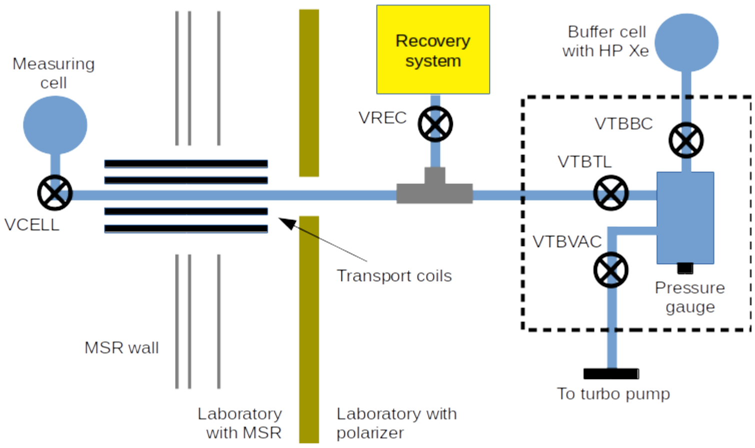

Figure 6.1.1: Sketch of the filling line with all connected parts.

fields in space and time should be avoided. A critical region is the passage through the Mu-metal layers of the MSR. To obtain an adiabatically changing magnetic field, two cylindrical transport coils are introduced producing a parallel guiding field. Their diameter and currents are chosen such that the inner coil compensates the magnetic flux of the outer coil. The effect is that outside both coils the stray fields are canceled to first order which leaves the Mu-metal unaffected. Within the inner coil, however, a longitudinal guiding field is achieved guaranteeing a save passage for the spins without significant losses in polarization. As already mentioned, main parts of the transfer line consist of copper tubes. In order to remove stress near the flange connections at the titanium block or the glass valve, the copper line is interrupted by flexible plastic tubes. The connection is realized by pushing the plastic tube over the copper tube. To seal this transition, it is covered by a shrink tube with glue inside which melts when heat is applied.

Starting with a buffer cell containing around 270 mbar of HP xenon, the first step to transfer the gas into the MSR is to evacuate the whole transfer line, the measurement cell and the titanium block (with VTBBC closed). Having reached a minimum pressure, VREC and VTBVAC have to be closed and the xenon gas can be shot in by opening valve VTBBC. An equilibrium pressure will quickly establish which can be monitored by the pressure gauge of the titanium block. Finally, VCELL and VTBBC can be closed and the transfer line can be evacuated again. As a result, the measurement cell and the buffer cell are filled with HP xenon with a known pressure. Due to the small volume of the transfer line, this process can be repeated for several times. For each cycle, the pressure reduces roughly by a factor of two. Due to the long T_1 relaxation time of 3.5 h for the buffer cell, several tests within the MSR can be performed polarizing the xenon only once.

In the next paragraph, the coil system within the MSR should be presented. Before starting with its description, it should be mentioned that the following setup was mainly designed and constructed by Fabian Allmendinger and Josef Tremmel. In Fig. (6.1.2), a sketch of all coils is shown. Their main task is to produce a very homogeneous magnetic guiding field B_0 for the xenon spins in the measurement cell which is located at the center (not shown in this figure). This is achieved by quadratic coils which are positioned in Helmholtz configuration. In each axis, such a coil pair was installed. By superposition, an arbitrary direction for the magnetic holding field can be produced. Furthermore, it

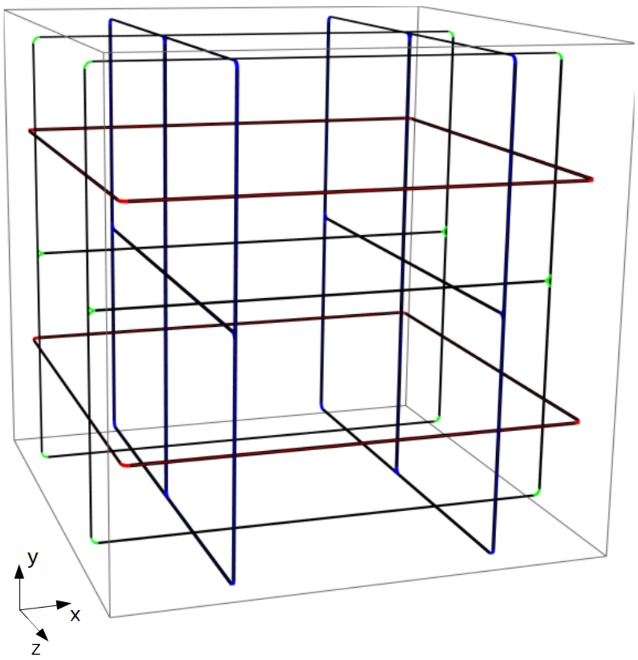

Figure 6.1.2: Coil system within the MSR to produce a homogeneous holding field B_0.

would be desirable to compensate magnetic field gradients to first order. Due to Maxwell's equations, the gradient matrix $\partial_i B_j$ has to be symmetric and traceless yielding to five independent parameters. For the diagonal elements in x and z direction, extra windings were added to the Helmholtz coils which have an antiparallel orientation. These windings can be controlled separately as independent channels. The three off-diagonal elements are a bit harder to realize. The idea was to use the Helmholtz coils as well by extending them by an additional path. As an example, the Helmholtz pair in z direction is regarded. Both coils have an additional horizontal line. The gradient coil consists of a single wire which is wound like an eight forming two loops for both coils. The current is applied such that the upper half produces a magnetic field in positive z direction whereas the field of the lower half shows in negative z direction. In the middle, both fields compensate and a sufficiently linear $\partial_y B_z$ gradient is generated. In this way, the two other off-diagonal components $\partial_y B_x$ and $\partial_z B_x$ are realized. In total, the coil system provides eight independent channels to be controlled. Three channels for the main fields in x, y and z direction plus the five gradients. Currently, the Helmholtz coils in x and z direction are connected to a 20-bit DAC (MAX5719, Analog Devices) which is sampled with a rate of 1 kHz allowing for an arbitrary movement of the magnetic holding field. The gradient coils are supplied by 16-bit DACs (LTC2686, Analog Devices). The DAC values are found by optimizing the gradients which is shown in a following section. During a measurement, their currents are kept at constant values. Further details regarding the setup and the electronics belonging to the coil system can be found in [81].

As initial step of a measurement, the MSR has to be degaussed and HP xenon has to be produced. During the degaussing, the magnetic guiding field in z direction is switched on. After shooting HP xenon into the MSR, closing the valve of the measurement cell VCELL and evacuating the transfer line, the spins can be flipped non-adiabatically as described in the theoretical introduction in chapter 2. The magnetic-field signal of the precessing spins is acquired by with the SQUID gradiometer. It provides an analog voltage

Figure 6.1.3: measurement cell under the SQUID system embedded into the coil system within the MSR. Source: [63].

proportional to the magnetic field gradient (see chapter 2 for further information) and is sampled with an ADC (ADS1299, Texas Instruments). Its resolution is 24 bit and the sampling rate was chosen to 250 Hz. To achieve a sufficiently low noise level, all read-out electronics will be located into a box of aluminum outside the MSR. The connection to the computer is realized by optical fiber links. It is planned to supply all circuits with car batteries with a capacity of roughly 50 Ah. As the setup is currently in an early stage, the aluminum box cannot be closed yet and instead of the batteries, a laboratory power supply is used.

6.2 Data evaluation

The following data-evaluation approach which is presented in the following was formally worked out in [47] and has been successfully applied in previous experiments performed by this working group. When shooting HP xenon into the measurement cell and flipping the spins by 90° as described above, the raw data recorded by the SQUID will look like in Fig. (6.2.1). At first glance, no clear signal can be observed. Zooming in by regarding a subcut of 4 s, a clear sine wave representing the spin precession of the xenon atoms can be resolved. Within the global plot, 700 of these subcuts are contained. It can be guessed that the amplitude decreases exponentially as expected for a transversal T_2 decay. In order to see this quantitatively, each subcut is fitted with a sine wave and an offset allowing for linear drifts:

$$f_i(t) = A_s \sin(2\pi f t) + A_c \cos(2\pi f t) + d \cdot t + c \quad . \tag{6.2.1}$$

When fitting the subcuts, the error of a single data point was estimated by the spectral noise density (see Fig. (6.2.2)). A rough estimate would yield an error of 110 fT assuming a baseline of 10 $\mathrm{fT}/\sqrt{\mathrm{Hz}}$ and a bandwidth of 125 Hz. Regarding the FFT, the noise can be assumed to be Gaussian at first order. The 1/f noise is accounted for by allowing linear drifts in the fit function. The most prominent peak represents the precession signal of the xenon spins. Smaller peaks at frequencies larger than 10 Hz are assumed to be caused by electric noise of the power supply or magnetic coupling of external signals. When the DAQ setup is completed such that it can be powered by a car battery within a closed aluminum box, a much lower noise level of 1 $\mathrm{fT}/\sqrt{\mathrm{Hz}}$ without peaks is expected.

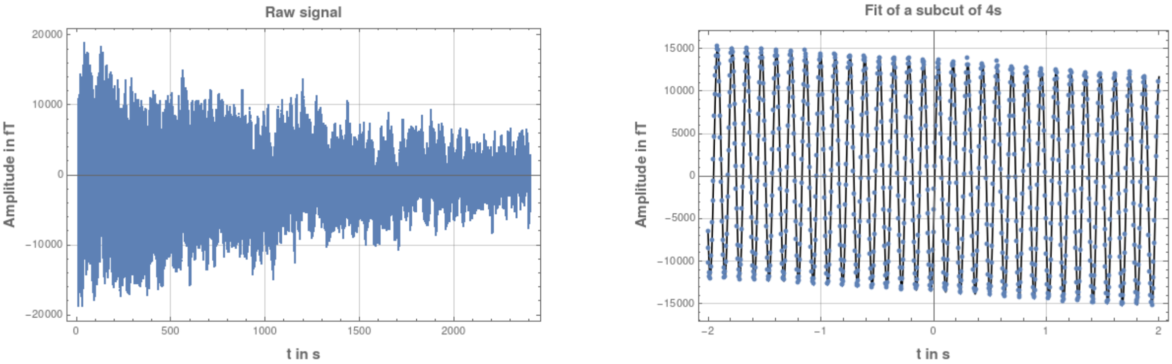

Figure 6.2.1: Left: raw data recorded during a T_2 measurement by the SQUID gradiometer, right: zoomed in subcut with fit.

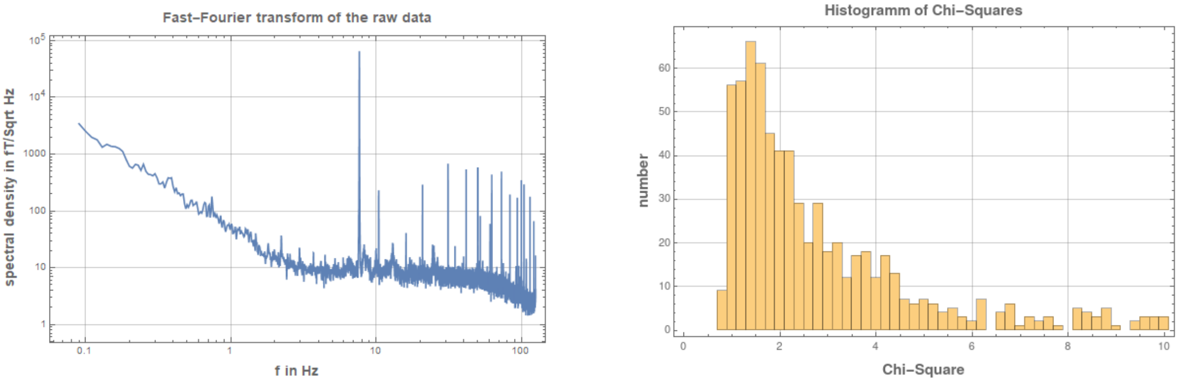

Figure 6.2.2: Left: Fast-Fourier transform of the raw data, right: distribution of χ^2_{red} for the 700 subcuts.

Regarding the χ^2_{red} values of the 700 subcuts, it can be deduced that the maximum in the histogram (see Fig. (6.2.2)) is approximately at 1. The long tail at the right hand side may be caused by higher order drifts which are not absorbed by the linear term in the fit function.

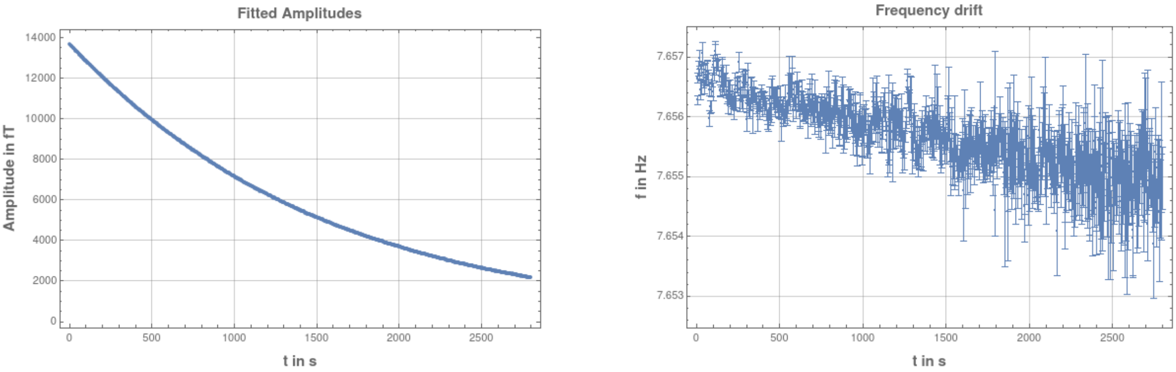

Figure 6.2.3: Fit results of the 700 subcuts: amplitude (left), frequencies (right).

Having fitted all subcuts, from the fit parameters the amplitude, frequency and the phase can be extracted. In Fig. (6.2.3), the amplitude and the frequency is shown. It has to be mentioned, that in all plots whenever fit parameters are shown, the correlated errors are given. In case of the amplitudes they are at the order of few fT which is much smaller than the point size. The amplitudes are showing a nice exponential decay describing the T_2 relaxation. The T_2 relaxation time of roughly 1500 s can be read off. Regarding the frequencies, a drift of order 10^{-4} is measured which is caused by a drift of the magnetic holding field. In this measurement, the door of the MSR was opened between the degaussing and the beginning of the measurement. As a result, the Mu-metal of the MSR is relaxing into a new equilibrium causing this drift. When the degaussing is performed a few hours before the measurement without opening the door, this drift of this magnitude is not observed. The error bars of the frequency are increasing over time, as the signal-to-noise ratio decreases with the amplitude. In the following measurements, the amplitudes are of great interest because from them the initial amplitude and the T_2 relaxation time can be extracted by an exponential fit:

$$A(t) = A_0 \exp(-t/T_2). \tag{6.2.2}$$

6.3 T_2^* Measurements

The procedure described in the section above was used when several measurements of T_2 were performed. This quantity is directly related to magnetic field gradients by

$$\frac{1}{T_{2,\mathrm{grad}}} = \frac{8R^4\gamma^2}{175D}\left(a(\lambda)\cdot(|\nabla B_x|^2 + |\nabla B_y|^2) + |\nabla B_z|^2\right) \tag{6.3.1}$$

(compare to equation (2.3.11)). To plug in realistic numbers the radius of the spherical measurement cell was estimated by filling it with deionized water and measuring the mass difference. With this method the radius was found to be R = (4.578 ± 0.007) cm. The diffusion coefficient can be calculated with equation (2.3.2) and $D_0 = (0.058 \pm 0.003)$ bar cm^2/s [35] which has to be divided by the actual gas pressure. The value of γ is given in (2.1.4). It has to be multiplied with 2π. The magnitude of the magnetic holding field B_0 was set to 650 nT throughout the measurements. With these values at hand, it can calculated that λ and $a(\lambda)$ are vanishing. Therefore, the equation above simplifies and T_2^* is given by

$$T_2^* = \frac{1}{\frac{1}{T_1} + \frac{8R^4\gamma^2 p}{175D_0}|\nabla B_z|^2} . \tag{6.3.2}$$

In the following measurements, three runs at different xenon pressures were performed. The parameters can be found in Tab. (6.3).

# Measurement	p in mbar	T_2 in s
1	54	2206.1 ± 0.3
2	20	3561 ± 15
3	9	4137 ± 17

Table 6.3.1: T_2 relaxation times for different pressures.

Plotting these points and fitting them using equation (6.3.2) gives only a rough estimate of T_1 and the overall gradient $|\nabla B_z|$. However, this three points are verifying at least qualitatively, that the gas sample becomes more sensitive to gradients yielding to shorter T_2 times when the pressure increases. From the fit, a T_1 of (1.4 ± 0.1) h and an overall B_z gradient of (50 ± 1) pT/cm can be extracted. In the following sections both quantities are measured directly and are compared to what was obtained with this estimate.

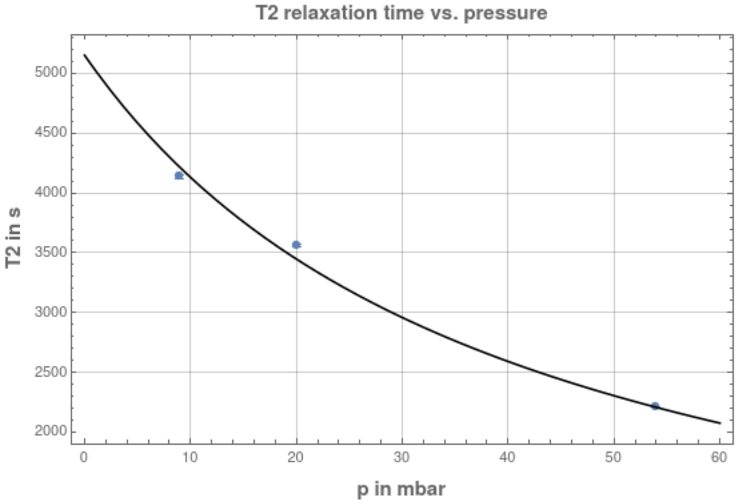

Figure 6.3.1: Fit of the Cates formula to the T_2 data.

6.4 T_1 Measurements

The basic idea of measuring T_1 is that the spins are flipped by a small angle of 15° for multiple times. In Fig. (6.4.1) the fitted amplitudes of a T_1 measurement are shown. Regarding the plot already reveals the experimental procedure. After flipping the spins by 15° the T_2 relaxation is measured. After some time, a spoiler gradient is turned on in order to accelerate the transverse relaxation. For the last flip an angle of 90° was used to measure the maximum signal which is available. It would be desirable to reach a vanishing remaining amplitude. Otherwise, it could add up with the signal of the next flip. This depends on the relative phase between both signals and is quite hard to control. For this reason, the remaining amplitudes (in this measurement roughly 300 fT) are added quadratically to the correlated error of the initial amplitude after each flip. As T_1 should be independent of magnetic field gradients (when plugging realistic numbers into equation (2.3.3) values up to 100 h will be obtained which is much larger than the expected wall relaxation time of several hours) the spoiler gradients could be turned on during the whole measurement yielding to a faster T_2 decay without changing the initial amplitude. This also simplifies the data evaluation since the exponential function describing the T_2 relaxation can be directly fitted to the amplitudes without pre-selecting the data points due to spoiler gradients.

In Fig. (6.4.2), another exponential function reflecting the T_1 relaxation was fitted to the initial amplitudes obtained from the T_2 fits of the amplitudes in Fig. (6.4.1). It has to be mentioned that the data points in Fig. (6.4.2) have to be corrected. When the spins are flipped by angle α the measured transverse component scales with $\sin(\alpha)$ and the longitudinal component decreases with $\cos(\alpha)$. After n flips the signal has to be divided by $\sin(\alpha)\cos^{n-1}(\alpha)$ to obtain the initial longitudinal magnetization. When the flips are

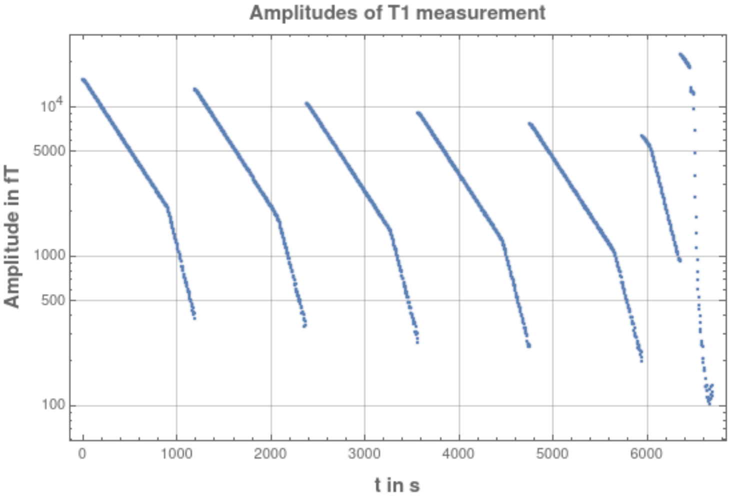

Figure 6.4.1: Fitted amplitudes of the T_1 measurement. The spins were flipped 6 times by 15° and finally by 90°.

performed in equidistant time steps, this correction is also exponential in time yielding to a shift of T_1. Accounting for this correction, the fit in Fig. (6.4.2) results in a T_1 relaxation time of (2.36 ± 0.07) h.

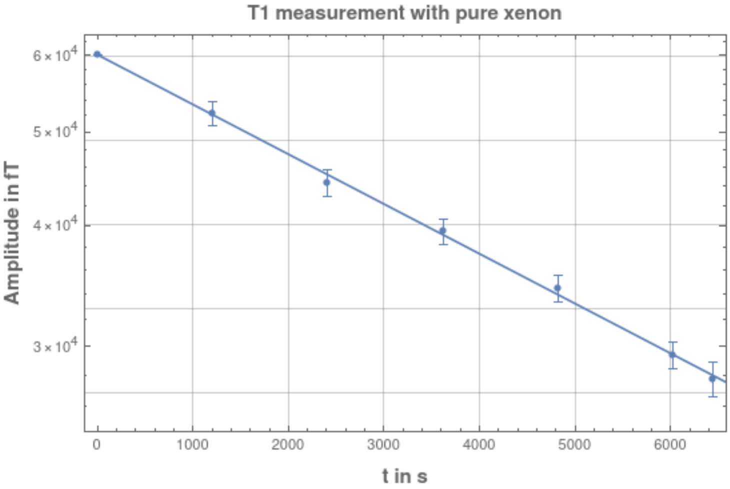

Figure 6.4.2: Exponential fit to obtain T_1.

Several measurements of this kind have been acquired. The results are listed in Tab. (6.4). Run 1 and 2 were performed by two shots into the MSR originating from the same polarization cycle. Run 3 was done on another day and differs by the addition of nitrogen as buffer gas. The different errors of T_1 are caused by different measuring routines. The main contribution comes from the remaining amplitude of the previous flip. By increasing the gradients, the decay will be faster yielding to a lower remaining amplitude and therefore to a lower error. Furthermore, the number of steps was varied as well. Regarding the results, some inconsistencies may be found. As explained in chapter 2, the main contributing mechanisms to the overall T_1 relaxation are wall relaxation, Van-der-Waals interaction and interaction with paramagnetic centers like O_2 molecules. All three mechanisms have in common that they are independent of the absolute pressure. For this reason, it is expected that run 1 and 2 should produce the same T_1. Statistically, the values obtained are not fully compatible with each other. Comparing these two values to T_1 which was obtained by the pressure dependent T_2 measurement in the previous section, the deviations are also significant. A second inconsistency arises from run 3 where buffer gas was used. The addition of a buffer gas should increase the maximum T_1 relaxation time which is limited by the formation of Van-der-Waals molecules. A buffer gas reduces the lifetime of such molecules and therefore the loss of polarization. According to equation(2.3.7), a gas mixture of ^{129}Xe and N_2 (1:1) should increase T_1 by roughly a factor two. The so-called break-up efficiency which depends on the buffer gas is given in [31] by $r_{\mathrm{N}_2} = (1.05 \pm 0.08)$. Regarding the buffer gas measurement in Tab. (6.4), such an increase is not observed.

# Measurement	T_1 in s	p_{Xe}/p_{N_2} in mbar
1	8521 ± 254	127.5 / 0.0
2	7723 ± 103	56.0 / 0.0
3	6902 ± 21	55.2 / 56.7

Table 6.4.1: T_1 relaxation times for different measurements.

Especially the measurement with the buffer gas suggests that T_1 is limited by the interaction with oxygen. Whenever the transfer line is not in use it should be connected to the turbo pump to keep it free from oxygen. In the Appendix, a vacuum test of the transfer line yielded to a leakage rate of $3 \cdot 10^{-5}$ mbar·l/s. Assuming a volume of one liter, a pressure of few millibars can be reached when the pump is not connected for one day. On the other hand, when the pump is connected again, it will take many hours until the transfer line is evacuated because of its small cross section. It was not monitored for every run, how long the transfer line was evacuated before. It is assumed therefore, that variations of T_1 can be explained by the (fluctuating) presence of oxygen between several measurement runs. For this reason, it is planned to rebuild the filling line exchanging all plastic tubes by copper bellows to achieve a much better leakage rate.

6.5 Measurements of magnetic field gradients

In the last and final measurement in context of this thesis, the magnetic field gradients were examined. As previously discussed, the setup used so far is only sensitive to gradients $\partial_x B_z$, $\partial_y B_z$ and $\partial_z B_z$. The procedure was to shoot HP xenon into the degaussed MSR. After flipping the spins by 90°, the gradients were varied linearly one after the other by changing the currents of the gradient coils. With the SQUID system, the different T_2 relaxation times were measured in the usual way. Each run consists of sweeps in x, y and z direction. In total, two runs were recorded with different pressures. To express the Cates formula (6.3.2) in terms of currents, the gradients are replaced by an initial gradient $G^0_{zx_i}$ and the gradient-coil factor G_{zx_i}:

$$T_2^* = \frac{1}{\frac{1}{T_1} + \frac{8R^4\gamma^2 p}{175 D_0}((G^0_{zx} + G_{zx} \cdot I_{zx})^2 + (G^0_{zy} + G_{zy} \cdot I_{zy})^2 + (G^0_{zz} + G_{zz} \cdot I_{zz})^2)} \quad . \tag{6.5.1}$$

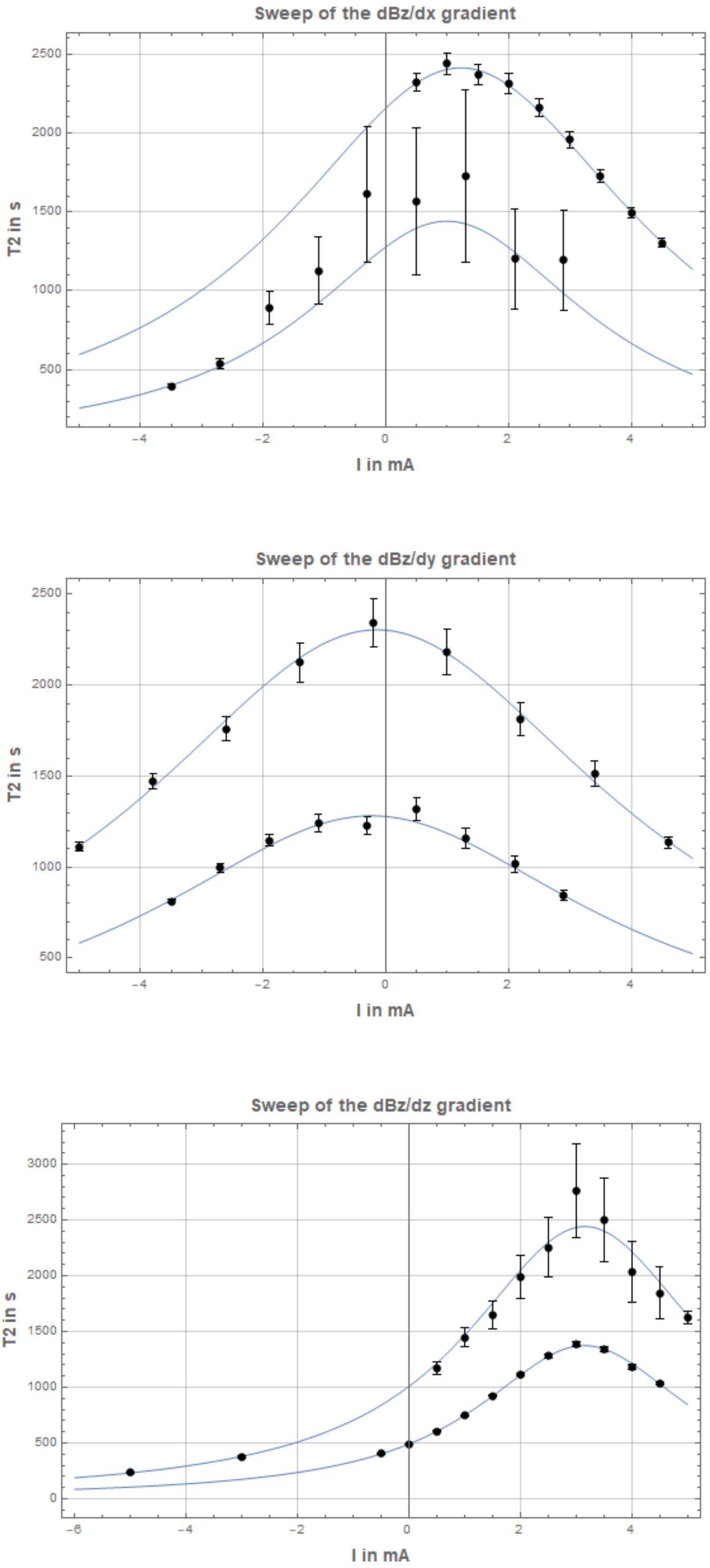

Figure 6.5.1: Gradient sweeps in x, y and z direction at two different pressures.

This equation was fitted in three dimensions (I_{zx}, I_{zy} and I_{zz}) to the obtained T_2^* values from a single run. This results into two independent fits per direction at two different pressures. In figures (6.5.1), these fits are shown in each plot. The sweep providing higher

# parameter	run 1 (p=129.0 mbar)	run 2 (p=56.5 mbar)
G^0_{zx}[pTcm^{-1}]	-19 ± 5	-21 ± 3
G^0_{zy}[pTcm^{-1}]	3.0 ± 0.9	2.0 ± 0.9
G^0_{zz}[pTcm^{-1}]	-73.1 ± 0.1	-74.0 ± 1.0
G_{zx}[pTcm^{-1}mA^{-1}]	19.1 ± 1.3	17.5 ± 0.7
G_{zy}[pTcm^{-1}mA^{-1}]	13.0 ± 0.3	13.6 ± 0.2
G_{zz}[pTcm^{-1}mA^{-1}]	23.3 ± 0.1	23.5 ± 0.2
T_1[s]	1569 ± 125	2570 ± 40

Table 6.5.1: Obtained fit parameters by the Cates formula.

T_2^* times was acquired with a lower pressure which is in accordance with the Cates formula. The different magnitude of the error bars is affected by two aspects. The first one is the signal strength of the spin sample which is left after performing a certain number of steps. When the amplitude becomes too small, the errors will increase. An other aspect is the measuring time which was kept constant for each current step. For large relaxation times, only a small fraction of T_2^* is sampled resulting into large errors. For lower T_2 times, the error becomes therefore smaller.

The parameters obtained by these fits are shown in Tab. (6.5). Comparing the values of the initial gradients and the gradient-coil factors between the two different runs, they are statistically compatible. The $\partial_z B_z$ gradient seems to be much larger than the other two gradients. Regarding the T_1 relaxation times, huge deviations are found. In the previous section, a maximum T_1 of more than 8500 s was measured. It was argued before that different T_1 values might be explained by the presence of oxygen. With equation (2.3.9), however, it can be estimated that the partial pressure of O_2 must be around 0.5 mbar to get from a T_1 of 8500 s down to 2570 s and around 1 mbar to get down to 1600 s by

$$1/T_1 = 1/T_1^0 + 1/T_{1,O_2} \quad . \tag{6.5.2}$$

The first partial pressure of 0.5 mbar is quite large, however, when the filling line was not connected to the pump before, it is very likely that this pressure can be reached, as discussed before. On the other hand, it is very unlikely that an additional amount of oxygen enters between the two measurement runs. It is therefore assumed that another mechanism is responsible for the different T_1 values observed. The T_1 time extracted by the fit corresponds to the maximum T_2^* when no gradients are present. It should be reminded that the Cates formula describes the T_2^* relaxation only for linear gradients. When higher order gradients were present, the fits above will only extract the linear components. The rest is absorbed into the T_1 parameter. For different pressures the sensitivity to gradients (also to the higher order ones) changes, and therefore the impact on the T_1 value obtained by the fit. One conclusion might be that there is a magnetic part contained in the setup generating local nonlinear field gradients. For this reason, the whole setup was disassembled and each part was examined with the SQUID system. The strategy was to move a part under the SQUID system while the signal was observed. If the part is magnetic a clear time dependence correlated to the movement will be observed. Doing these tests, it could be found out that two O-rings were very magnetic. To quantify their magnetic field the measurements were repeated with fluxgate magnetometers since the SQUID system is only sensitive to gradients. These measurements yielded to magnetic fields of more than 100 nT which is much too large (see Fig. (6.5.2))

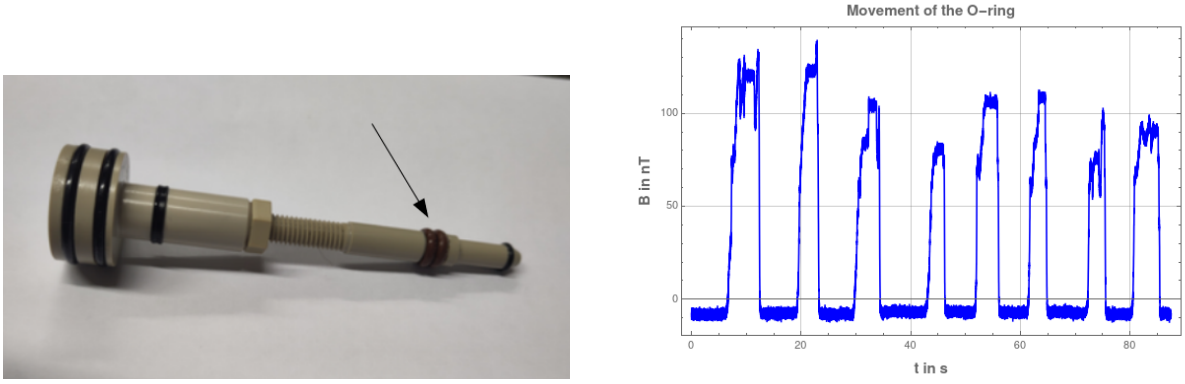

Figure 6.5.2: Left: Magnetic O-rings at the piston used in the cell valve VCELL (black arrow), right: magnetic field of a moving O-ring (removed from the piston) measured with a fluxgate.

This observation explains some inconsistencies which occurred throughout the measurements. The fact that the magnetic field of the O-rings (both O-rings caused roughly the same magnetic field magnitude) is so large makes it very clear that higher order gradients are the reason for different T_1 when fitting the Cates formula. That is also the reason why the maximum T_2 is much lower than the maximum T_1 time which was measured because a larger pressure would be more sensitive to (non-linear) gradients. In case the O-rings were removed and the gradients would become much better and long T_2^* relaxation times of up to several hours might be expected.

Chapter 7

Summary and outlook

This work has laid two important cornerstones for a new ^{129}Xe-EDM (electric dipole moment) experiment in Heidelberg: commissioning of a suitable MSR (magnetically shielded room) and production of HP (hyperpolarized) xenon. With the expertise of the last EDM experiment in Jülich [12], a next generation ^{129}Xe-EDM measurement is within reach.

Starting point of this thesis was the construction of a new MSR at the Physikalisches Institut Heidelberg. In the first part, the MSR was characterized by determining the residual magnetic field at its center and the shielding factors. For these measurements, a fluxgate magnetometer was used due to its simplicity concerning the operation. Furthermore, a new way of degaussing was introduced. It was verified by residual magnetic field measurements and could be theoretically motivated by solving Maxwell's equations numerically in one dimension for an infinite Mu-metal plate. By comparing measured and simulated hysteresis loops, the theoretical model could be validated. All in all, it could be shown that eddy currents are affecting the screening depth of an external oscillating magnetic field depending on its frequency. The consequence is that only the magnetic domains located at the outer part of the Mu-metal plate are saturated. To saturate also the inner domains, the frequency was reduced in order to minimize the effect of eddy currents. With this knowledge a suitable degaussing routine was found which yields to reproducibly low residual magnetic fields within the MSR.

In order to perform measurements of precessing spins within the MSR, a HP noble gas is needed in order to achieve a sufficient SNR (signal-to-noise ratio) which is crucial for precision comagnetometry. In the second part of this thesis, the production of HP xenon was achieved. An existing setup was commissioned by performing several vacuum tests and establishing a defined gas flow with a known composition of xenon and other buffer gases. In addition, the oven heating the optical pumping cell, and the magnetic holding field had to be tested. A more complex task was to characterize the diode laser which is used to polarize the valence electron of rubidium. To achieve a useful polarization of rubidium (and therefore of xenon), the circular polarization of the laser had to be verified. This was realized by a dedicated measurement of the Stokes parameters of the beam using a rotating $\lambda/4$ plate and a beam splitter cube as analyzer. The outcome of this analysis revealed a degree of polarization of 89% which can be fully converted into circular polarization. When the first tests of the polarizer were performed, the optimal settings for most parameters were not known. To have a feedback signal of the parameter settings, a sophisticated online NMR monitor was set up which contains a Q-switch suppressing ring-down effects originating from an LC tank with high Q-factor. In combination with an advanced fit routine, a high SNR of the xenon-NMR signal was obtained. As a final step, the accumulation of HP xenon was carried out reproducibly. Within a typical polarization cycle of one hour, an amount of 120 mbar·l HP xenon with a polarization of 15-20% can be reliably produced.

As a smaller chapter of this thesis, the calibration of the xenon-NMR signal was examined. The same NMR volume which is used for the detection of HP xenon was rebuilt and filled by distilled water with dissolved $CuSO_4$. Although its NMR signal was smaller by two orders of magnitude than the xenon signal, it was managed to detect it with the same frequency imposed by the LC tank. This allowed for a calibration of xenon-NMR signal providing absolute polarization values for the xenon gas.

Finally, the HP xenon produced by the polarizer was successfully transferred into the MSR. Together with a coil system presented in [81] and a SQUID system described in [53], first measurements of precessing spins could be performed. Systematic tests of the storage time T_1 and the coherence time T_2^* were conducted. It was demonstrated that magnetic field gradients can be determined with a resolution of 1 pT/cm and below.

The end of this thesis marks the beginning of various tests to optimize the experimental setup. It has been shown that magnetic parts are contained close to the measurement cell gives rise to higher order magnetic field gradients. Exchanging them will improve the gradients and higher T_2^* times are expected. Another effect which was not examined in the scope of this work is the loss in polarization when transferring HP noble gas into the MSR. Before shooting HP xenon into the MSR, its polarization can be measured with the developed NMR monitor. Inside the MSR, the polarization can be estimated by measuring the change of the magnetic field near the measurement cell before and after filling. To measure the permanent EDM of ^{129}Xe there are still a few steps to go. First of all, an equivalent setup to what was presented in this work is needed to hyperpolarize ^{3}He. Such a setup exists and was used in the EDM measurement in Jülich. Due to limited manpower, it was not possible to commission the helium polarizer in parallel to the xenon polarizer so far. Furthermore, the measurement cell needs to be redesigned since large electric fields ($\approx$ 800 V/cm) have to be applied when measuring the EDM. This requires electrodes near the measurement cell without changing the magnetic field and introducing additional noise such as Johnson noise.

Chapter 8

Appendix

8.1 Construction of the MSR in Heidelberg

Figure 8.1.1: Internal structure of the MSR with Mu-metal plates to be attached.

8.2 How does degaussing look like?

In the following picture, a hysteresis loop is shown which was recorded at 1Hz. The maximum amplitude started around 10 A/m and was ramped down exponentially. It can be nicely seen how the magnetization is reduced and approached the origin.

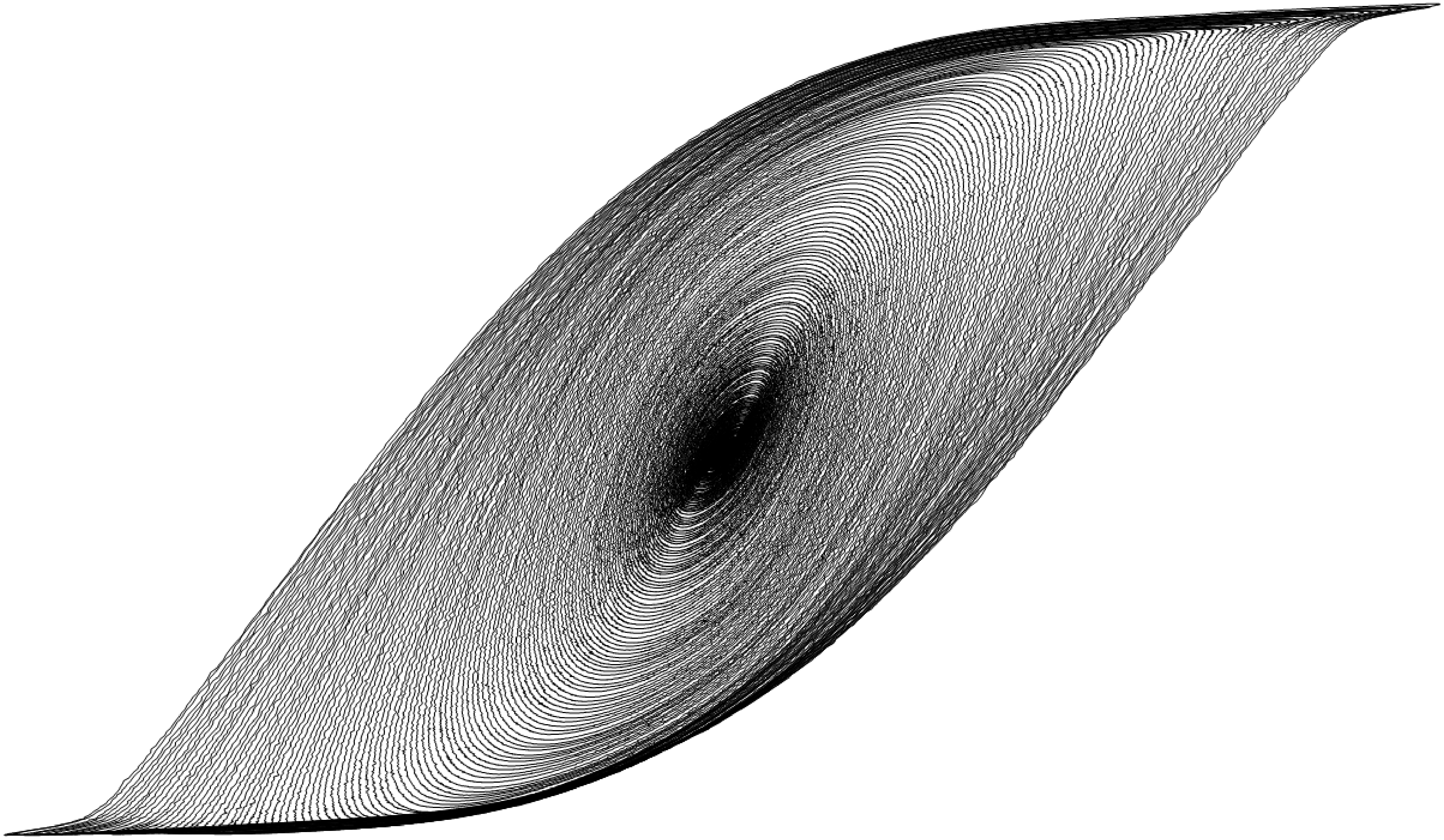

Figure 8.2.1: Measured hysteresis loop while degaussing the MSR.

8.3 Using the power meter for characterizing the laser

In this section, a few remarks are provided how the power meter used in this thesis should be operated. It is important to mention again, that the power sensor measures temperature changes of the bulk material when a laser beam hits it. Therefore, additional systematic temperature drifts must be controlled extremely well. For this reason, the sensor head is connected to a cooling-water circuit reducing the temperature of the sensor to 18°C. When the sensor is turned on, the water cooling should also be activated. After one hour the system is in thermal equilibrium and the measurements can be started.

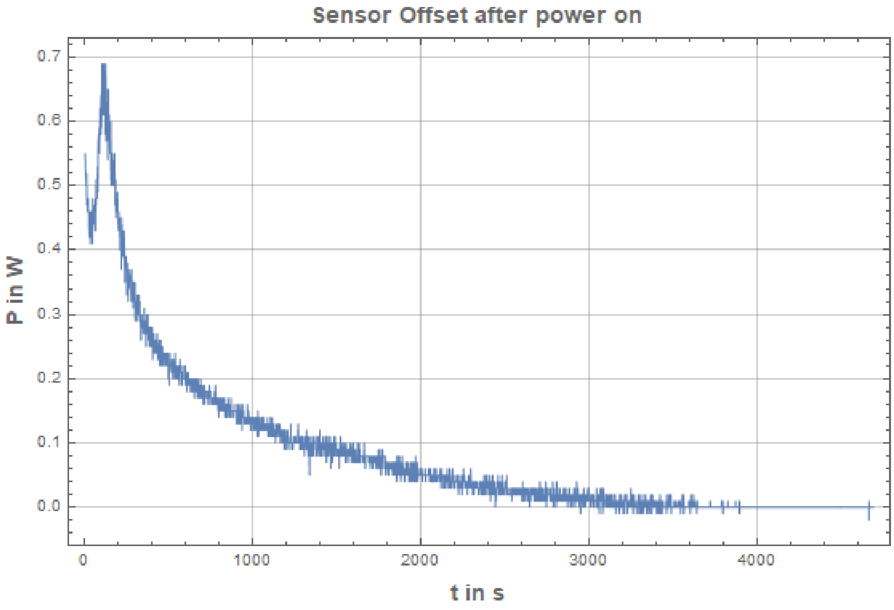

Figure 8.3.1: Offset of the power meter after turning on. Stable values are obtained after waiting for one hour.

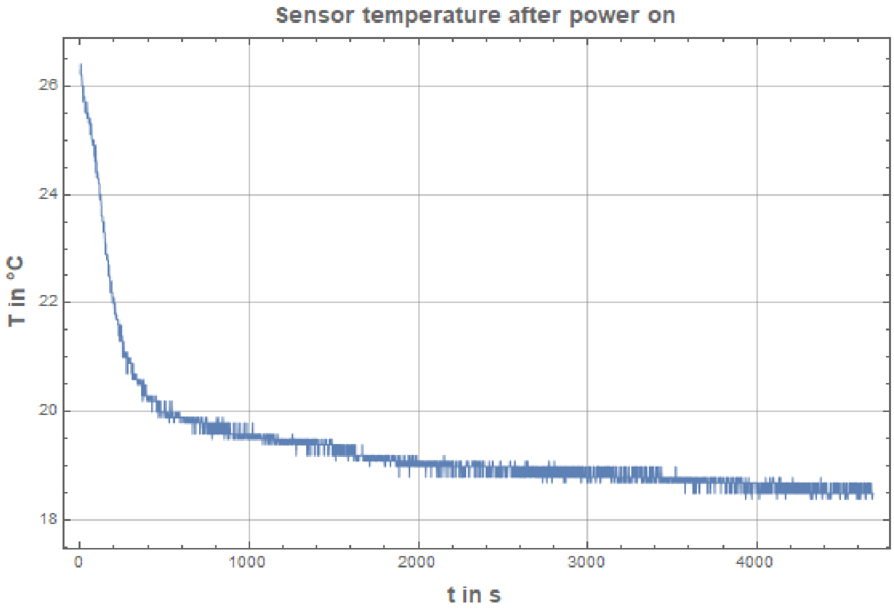

Figure 8.3.2: Temperature of the power meter after turning on.

When measuring, it should be remembered, that the power meter reacts very slowly to abrupt changes. This is tested by measuring the step response when a laser beam is blocked. In Fig. (8.3.3) the laser beam with power of 14 W was blocked. The measured power immediately drops, but a small slowly relaxing component remains for approx. 30 s. When averaging over these data points, systematic errors are introduced. This was taken into account for the measurements presented in chapter 4. The measured power changed very slowly such that the relaxation was negligible. In general, however, this relaxation can occur and it has to be checked how it affects the result.

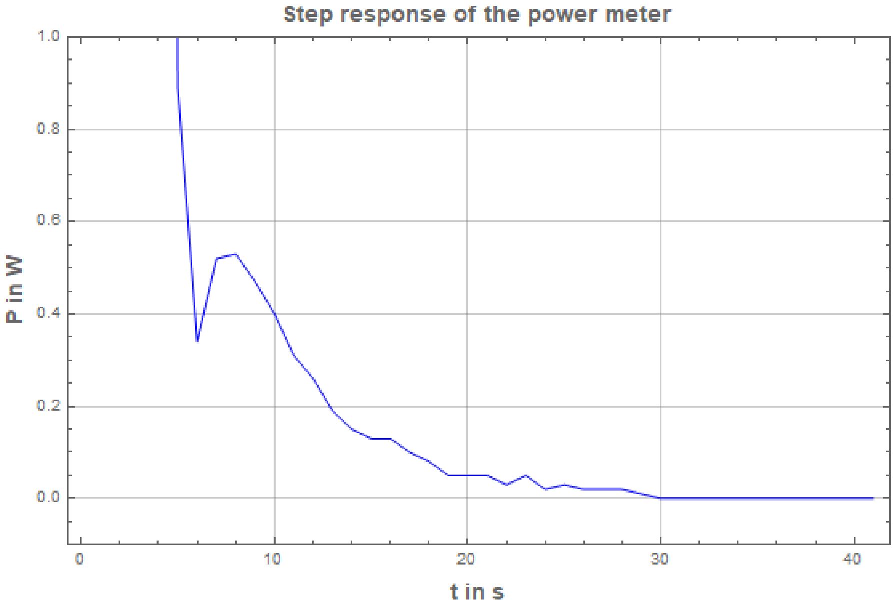

Figure 8.3.3: Laser beam is blocked at t=5 s.

8.4 Performing vacuum tests with the Xenon polarizer used in Heidelberg

In order to have a measure whether the quality of the vacuum of the xenon polarizer is sufficient or not, several tests were performed to quantitatively estimate leak rates of the system. The whole setup was divided into three sub volumes: the volume before and including the optical pumping cell (V_1), the volume behind (V_2) and the titanium block. Referring to the sketch of the vacuum system in Fig. (4.1.1), V_1 is restricted by the following closed valves: VOPOUT, VBACKF, VVAC1, VVAC4, VBYPHE, VBYPN2, VBYPXE. All other valves in between are opened. V_2 is defined by the closed valves VKTB, VKVAC, VOPOUT, VBYPASS, VVAC4. The titanium block is examined with VKTB closed.

The strategy of the following measurements was to evacuate the volumes in the beginning. Having reached a minimal pressure, the volume of interest is disconnected from the pump and the increase of pressure is observed. The pressure was measured by a pressure gauge (VSP63DL, Thyracont) which can be read out via the RS485 serial interface.

In order to quantify the leak rate of a corresponding volume, the two processes of outgassing and leaks have to be considered. Therefore, a fit function with an exponential and a linear term was chosen and fitted to the measured pressure increases (see Fig. (8.4.1)). Only the pressure values of V_2 which are larger than 2 mbar were fitted because the calibration of the pressure gauge changed leading to systematic errors when fitting all data.

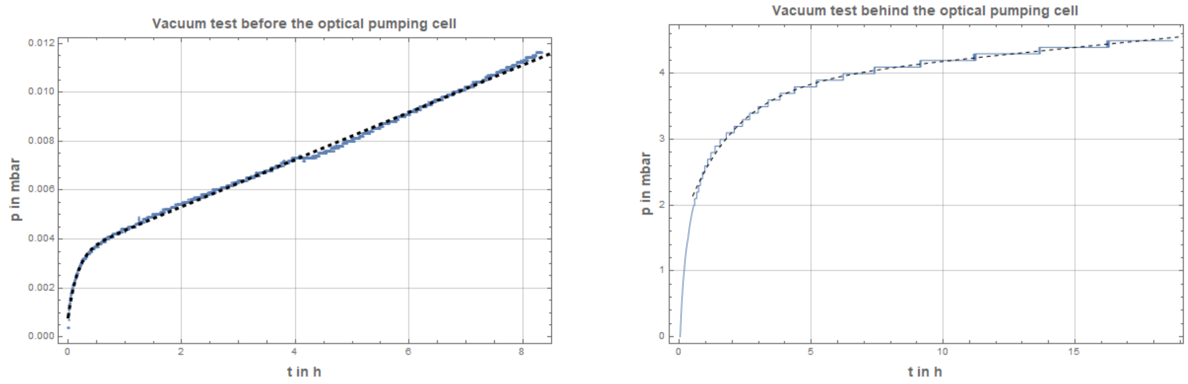

Figure 8.4.1: Pressure increase in V_1 (left) and V_2 (right)

From the coefficient of the linear term, the leak rates can be extracted. To give a final value, the size of the volumes has to be known. These were determined by expanding gas from a known volume V_0 with known pressure p_0 into the unknown volume $V_0 + V_x$. With the ideal gas equation V_x can be calculated. With this procedure, the following leak rates can be measured:

$$\mathrm{L}(V_1) = (5.4 \pm 0.3) \times 10^{-7}\ \text{mbar·l/s} \tag{8.4.1}$$

$$\mathrm{L}(V_2) = (6.2 \pm 0.2) \times 10^{-6}\ \text{mbar·l/s} \quad . \tag{8.4.2}$$

Comparing both measurements, V_1 shows a much better behavior than V_2. This can be explained by the fact that V_1 consists of many parts of stainless steel whereas V_2 includes many plastic tubes and valves and flanges of glass. Therefore, outgassing in V_2 is much larger than in V_1.

The third sub volume, which is the titanium block, is tested with the same procedure used above. As pressure gauge, an absolute pressure ceramic sensor (ME770, Amsys) was used. It is located in the inner volume of the titanium block which is attached to six valves (see Fig. (4.1.21)). For all measurements, the titanium block is disconnected from the system by closing the valve VKTB. In a first run, the inner volume and all attached volumes are evacuated by the turbo pump with VTBVAC opened (see Fig. (4.1.21)). Having reached a minimal pressure, all six valves were closed and the increase of pressure was measured. In a second run, the same measurement was repeated with all volumes attached (i.e. all valves opened except for VTBVAC). The transfer line was disconnected from the titanium block and the inlet of VTBTL was closed with a blind flange.

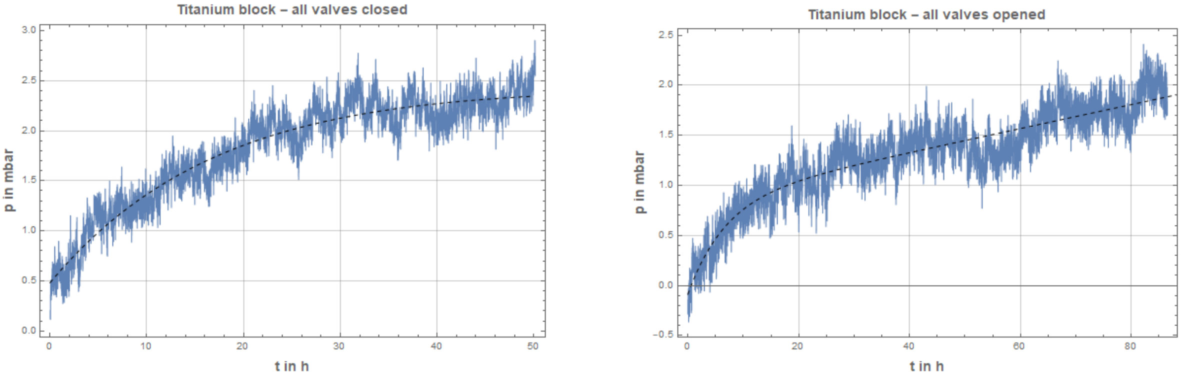

Figure 8.4.2: Pressure increase in the inner volume of the titanium block with all valves closed (left) and all volumes attached to (right).

In Fig. (8.4.2) the measured pressures are shown. In both cases, the process of outgassing can be observed. The fact that both measurements start at different pressures shows that the offset of the sensor is not stable and drifts probably with temperature. Therefore, the leak rates obtained from the fits are only rough estimates:

$$\mathrm{L}(\mathrm{TB}_{\mathrm{closed}}) = (-1.4 \pm 1.3) \times 10^{-8}\ \mathrm{mbar}\cdot\ \mathrm{l/s} \tag{8.4.3}$$
$$\mathrm{L}(\mathrm{TB}_{\mathrm{opened}}) = (1.7 \pm 0.2) \times 10^{-6}\ \mathrm{mbar}\cdot\ \mathrm{l/s}\quad . \tag{8.4.4}$$

The negative sign of the leak rate for the opened titanium block may suggest that gas may exit the inner volume and is pumped out by the turbo pump. But the large error of the leak rate shows that the fit parameters are strongly correlated. In order to reduce the correlations, this measurement should have been taken for a longer time. From the magnitude of the error, however, it can be deduced that the leak rate should be better than 10^{-8} mbar·l/s when all valves are closed.

Another important test of the titanium block is its switching behavior. The valves consist of pneumatic cylinders which are sealed with two quad rings. The volume between these rings is called middle volume and is connected to the turbo pump. This prevents any contamination from the atmosphere from reaching the inner volume. In the following test, the pressure of the middle volume is monitored during switching. It is connected to the turbo pump and therefore, the Thyracont pressure gauge can be used. All valves are closed in the beginning and a pressure of 10^{-3} mbar was measured. When a valve was switched, a small increase of maximum 10^{-2} mbar is observed for a few seconds (see Fig. (8.4.3), left). When the system was not used for a long time, it might be helpful to switch the valves for a few times before use in order to evacuate all dead volumes. Conversely, the inner volume can be tested performing the same test. Here, the ceramic sensor was used again to monitor the pressure of the inner volume. Also in this case, the inner volume and the connected outer volumes are evacuated through valve VTBVAC. After that, all valves were closed and switched except for valve VTBVAC. Before and after switching all valves 10 times each, no significant difference in pressure is observed (see Fig. (8.4.3), right). For this reason, it is assumed, that the inner volume remains safe from external contaminants.

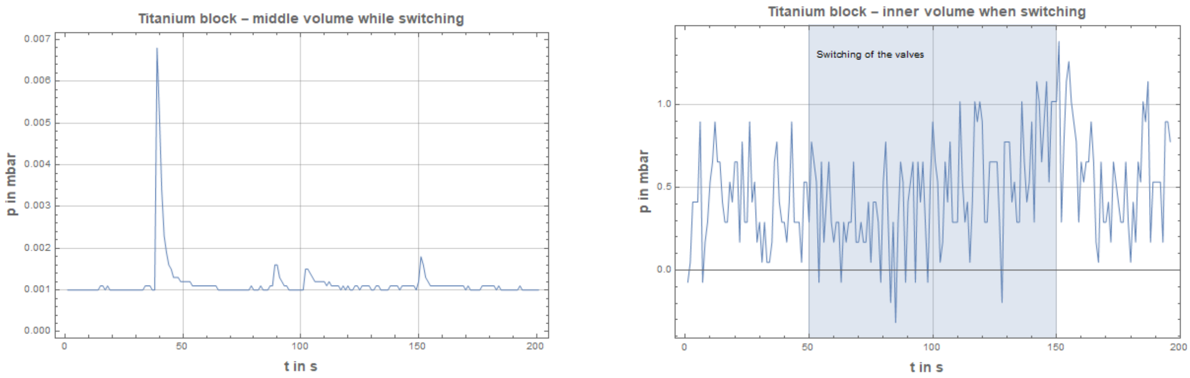

Figure 8.4.3: Switching behavior of the titanium block for the middle volume (left) and the inner volume(right).

A final vacuum test which has to be performed is the test of the filling line connecting the titanium block to the sample cell within the MSR. The same strategy was applied as before: the sample cell, the filling line and the titanium block are evacuated and disconnected from the pump (see Fig. (6.1.1)). The pressure increase was monitored again by the pressure gauge within the titanium block. All valves except for VTBTL were closed during that time.

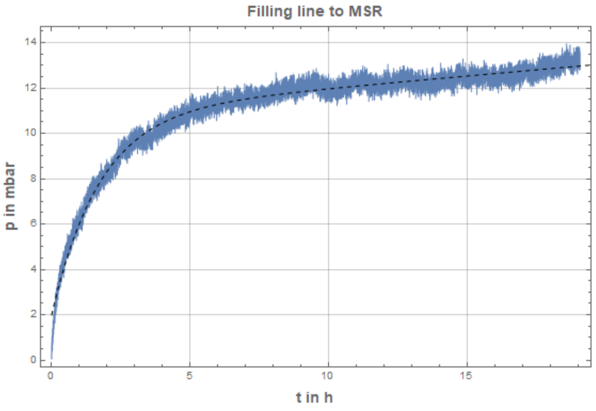

Figure 8.4.4: Pressure increase for opened sample cell, filling line and titanium block.

Assuming a total volume of one liter, the linear slope gives a leakage of

$$\text{L(TB, filling line, sample cell)} = (3.0 \pm 0.1) \times 10^{-5} \text{ mbar} \cdot \text{l/s} \quad . \tag{8.4.5}$$

Regarding Fig. (8.4.4) the outgassing of up to 10 mbar is much larger than in the other tests before. This volume also contains flexible tubes consisting of polyurethane which releases its plasticizer into the vacuum system. In addition, the leakage is also significantly larger than before. This is not very surprising due to the way the filling line is constructed (see chapter 6).

8.5 Operation of the polarizer

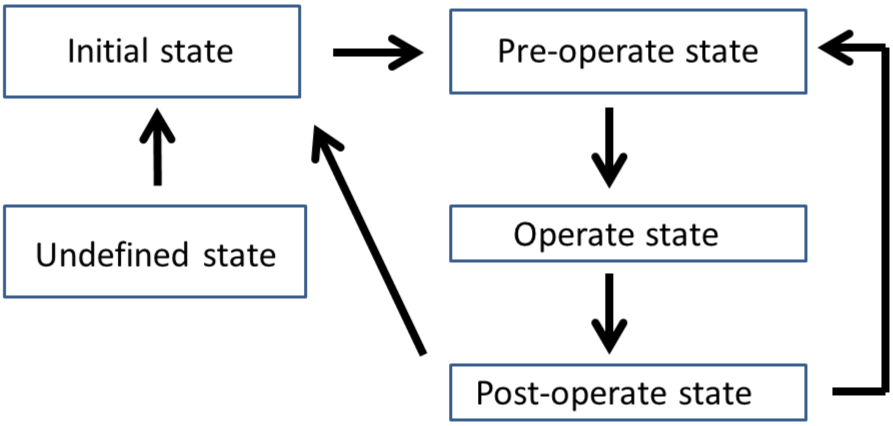

Figure 8.5.1: Different states of the polarizer.

In Fig. (8.5.1), different states of the polarizer are depicted. In the operate state, the polarizer is producing and accumulating HP xenon. In the post-operate state the whole polarization cycle is finished. The next state depends on the time when the next polarization cycle will start. When the polarizer is used in the next few days, it should enter the pre-operate state. For long stand-by times of more than one week, the initial state should be chosen. All other states are not defined and may be occurring for specific tests and measurements.

For the following instruction, please refer to figures (4.1.1) and (4.1.21).

8.5.1 Starting from an undefined state

When the state of the polarizer is not known, it should be put in the initial state. In this state, almost all valves are opened and the system is connected to the turbo pump to be evacuated. To get to this state, the following steps have to be carried out:

- Disconnect the polarizer from the turbo pump.
- Close the valves VOPIN and VOPOUT. They should be always closed except in the operate state. The transfer line should be also disconnected from the titanium block by closing VTBTL.
- Close the main valves of the gas tanks (not depicted in Fig. (4.1.1)).
- Close VMIX and open VVAC1, VBYPHE, VBYPN2, VBYPXE, VHE, VN2 and VXENAT. VVAC1 is connected to the mechanical pump which evacuates the whole gas mixing unit.
- Now, all other valves can be slowly opened with the exception of VOPIN and VOPOUT.
- When the pressure is below 1 mbar, the turbo pump can be connected. The mechanical pump should be disconnected by closing VVAC1 and VVAC4.

Now the polarizer is in the initial state.

8.5.2 Getting into the pre-operate state

In the pre-operate state, the lines of the polarizer are filled with the He/Xe/N_2 gas mixture from a former run (coming from the post-operate state). When this is not the case (coming from the initial state) the polarizer has to be filled with gas. Before, do the following steps:

- Close the bypass valves VBYPHE, VBYPN2, VBYPXE.
- Close the valves to the turbo pump VKVAC, VVAC3, VVAC5 and VVAC2
- Open the main valves of the gas tanks (not depicted in Fig. (4.1.1)).
- Start the gas flow. The pressure measured in the titanium block should increase linearly with time.
- When a pressure of 1900 mbar is reached, stop the gas flow.

Now the polarizer is in the pre-operate state. When coming from the post-operate state, the valves are in correct position, only VBYPASS has to be opened. When the pressure in the titanium block is too low, start the gas flow again, to reach 1900 mbar.

8.5.3 The operate state

In the operate state, the optical-pumping process is running producing and accumulating HP xenon gas. In this paragraph, only the start of the gas flow through the optical-pumping cell is described. Before the valves VOPIN and VOPOUT can be opened, all pressures have to be equalized. This is done with the following steps:

- If closed, open VBYPASS. This equalizes the pressures before and after the pumping cell.
- If closed, open VKIN.
- Close the needle valve VNOP.
- Open VOPIN.
- Slowly open the VNOP. Via the pressure in the titanium block, the equilibration of the pressures can be observed. When the pressure does not change,
- Open VOPOUT, VVAC4 and close VBYPASS.
- Start the gas flow. It should run through VMIX, VFLOW, VGETTER, VNOP, VOPIN, VOPOUT, VKIN, VCIN, VCOUT, VBACKF (all opened).
- Watch the pressure increase. When a pressure of 1990 mbar is measured, slowly open VNFLOW such that the pressure stays at a constant value of 2000 mbar. After a few minutes the pressure value may drift. In this case, the position of VNFLOW has to be adapted.

Now, the operate state is reached and the xenon polarization can start.

8.5.4 The post-operate state

After the polarization/accumulation cycle (operate state), the gas flow is stopped and HP xenon can be frozen out. After that, the post-operation state is reached. To get there, the following steps are performed:

- Close VKIN and open VNFLOW. The cold trap with the xenon ice will be evacuated via the mechanical pump.
- Stop the gas flow.
- Close VNVAC, open VVAC3.
- When the pressure in the titanium block is below 10 mbar, slowly open VNVAC. Now, the turbo pump evacuates the volume containing the cold trap. The mechanical pump can be disconnected by closing VVAC4.
- When the pressure in the titanium block is at minimum value, close VCOUT.
- The valves of the titanium block should be closed except VTBGL and VTBBC.

At this stage, the thawing process of the frozen xenon can start. When the thawing is completed (no pressure change in the titanium block), the pure xenon gas can be processed for further use. When the polarizer is not needed anymore, do the following steps:

- Close VVAC3 and open VVAC4 and VCOUT to evacuate the cold trap and the titanium block with mechanical pump.
- Close VNVAC, open VVAC3.
- When the pressure in the titanium block is below 10 mbar, slowly open VNVAC. Now, the turbo pump evacuates the volume containing the cold trap. The mechanical pump can be disconnected by closing VVAC4.
- Important: When the laser is shut down, close VOPIN and VOPOUT!

Now, the polarizer is in post-operate state.

8.5.5 Starting a polarization cycle

Having defined all states, the procedure of a polarization cycle is sketched in the following:

- Turn on the water cooling of power meter.
- Turn on the water cooling of the laser.
- Turn the temperature for oven (160°C) and Rb saturator (180°C).
- Turn on the magnetic holding field ($I = 2.185$ A).
- Fill the dewar with liquid nitrogen (LN2).
- Go into the operate state. The gas composition should be He: 182 ml/min, Xe: 2 ml/min and N_2: 16 ml/min.

- Turn on the laser and ramp to a current I=20 A. The wavelength is chosen to 794.82 nm.
- Wait until all temperatures stabilized. During this time, NMR shots can be taken to check the polarization.
- Increase the laser current to I=45 A. The NMR signal should be stable.
- Now, the accumulation can start by moving the LN2 dewar upwards.
- After the desired amount of HP xenon was accumulated, go into the post-operate state.
- Shut down the laser.
- Turn off the temperature for oven and Rb saturator.
- After ten minutes, stop the water cooling of the laser and the power meter.

8.5.6 Using the laser

In this paragraph a few more guidelines concerning the operation of the laser will be given. To turn the laser on,

- Close all doors and windows.
- Turn on the water cooling of the laser. Wait ten minutes.
- Put on the laser safety goggles.
- Start the TEC temperature controller with the key.
- Start the software ”Shark LS.exe”. Observe the temperatures which are displayed. When communication fails do not start the laser.
- Press the ON/OFF button. It should be green.
- Switch on the power supply. It should be in constant-current mode and the set current should be 0 A.
- Activate the output and increase the current very slowly (approx. 0.1 A/s). At currents larger than 10 A, the laser starts to emit.

To shut down the laser, the following steps are needed:

- Decrease the current very slowly to 0 A (approx. 0.1 A/s).
- Switch off the TEC temperature controller with the ON/OFF button in the software.
- Switch off the TEC temperature controller with the key.
- Wait ten minutes before stopping the water cooling

8.6 The NMR setup

In Fig. (8.6.1), the schematic of the amplifier is shown. It is needed to apply excitation pulses of up to 30 mA. After the pulse, an analog switch disconnects the amplifier from the NMR coil to avoid large noise contributions. In Fig. (8.6.2), the overall setup is shown. The microcontroller receives the TTL-trigger signal and produces the gating voltages for switches 1 and 2 with timing according to Fig. (4.1.17).

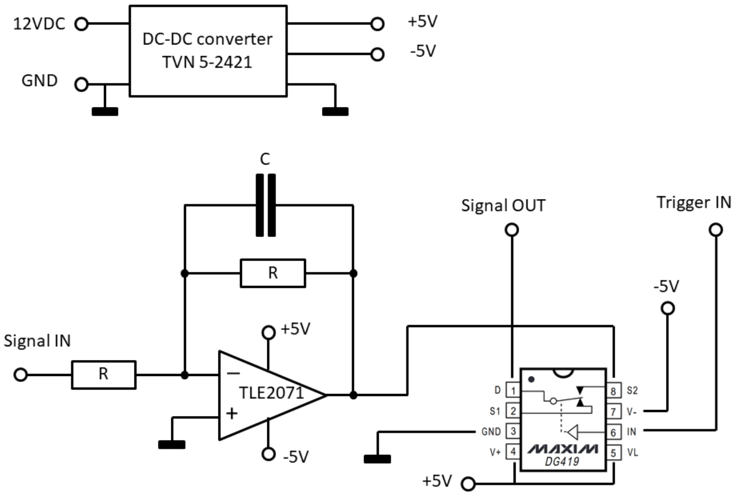

Figure 8.6.1: Sketch of the amplifier circuit. Decoupling capacitors of 100 nF between ±5 V and GND are not shown (image contains a part of [84]).

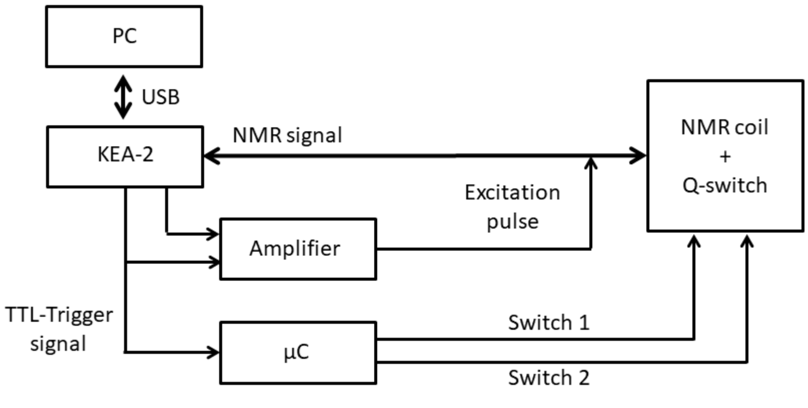

Figure 8.6.2: All components contained within the NMR setup.

Bibliography

[1] N. Mavromatos, “Matter-antimatter asymmetry in the universe via string-inspired CPT violation at early eras,” *Journal of Physics: Conference Series*, vol. 952, p. 012006, 01 2018.

[2] A. Sakharov, “Violation of CP invariance, C asymmetry, and baryon asymmetry of the universe,” *Soviet Physics Uspekhi*, vol. 34, p. 392, 05 1991.

[3] R. Jora, “Baryon asymmetry in the standard model revisited,” 2018. arXiv eprint 1806.00597.

[4] B. Brauneis, “Vorbereitungen für das Helium-Xenon-Experiment in Heidelberg,” master’s thesis, Heidelberg University, Heidelberg, Germany, 2021.

[5] M. Pospelov and A. Ritz, “CKM benchmarks for electron electric dipole moment experiments,” *Phys. Rev. D*, vol. 89, p. 056006, 03 2014.

[6] V. Baluni, “CP-nonconserving effects in quantum chromodynamics,” *Phys. Rev. D*, vol. 19, pp. 2227–2230, 04 1979.

[7] J. Smith, E. Purcell, and N. Ramsey, “Experimental Limit to the Electric Dipole Moment of the Neutron,” *Phys. Rev.*, vol. 108, pp. 120–122, 10 1957.

[8] C. Abel *et al.*, “Measurement of the Permanent Electric Dipole Moment of the Neutron,” *Phys. Rev. Lett.*, vol. 124, p. 081803, 02 2020.

[9] R. Peccei and H. Quinn, “CP Conservation in the Presence of Pseudoparticles,” *Phys. Rev. Lett.*, vol. 38, pp. 1440–1443, 06 1977.

[10] J. Engel *et al.*, “Electric dipole moments of nucleons, nuclei, and atoms: The Standard Model and beyond,” *Progress in Particle and Nuclear Physics*, vol. 71, pp. 21–74, 2013. Fundamental Symmetries in the Era of the LHC.

[11] S. Degenkolb *et al.*, “A Global View of the EDM Landscape,” 2024. arXiv.

[12] F. Allmendinger *et al.*, “Measurement of the permanent electric dipole moment of the ^{129}Xe atom,” *Phys. Rev. A*, vol. 100, p. 022505, 08 2019.

[13] N. Sachdeva *et al.*, “New Limit on the Permanent Electric Dipole Moment of ^{129}Xe Using ^{3}He Comagnetometry and SQUID Detection,” *Phys. Rev. Lett.*, vol. 123, p. 143003, 10 2019.

[14] L. Schiff, “Measurability of Nuclear Electric Dipole Moments,” *Phys. Rev.*, vol. 132, pp. 2194–2200, 12 1963.

[15] V. Flambaum, I. Khriplovich, and O. Sushkov, “On the Possibility to Study P Odd and T Odd Nuclear Forces in Atomic and Molecular Experiments,” *Sov. Phys. JETP*, vol. 60, p. 873, 1984.

[16] C. Gemmel *et al.*, “Ultra-sensitive magnetometry based on free precession of nuclear spins,” *The European Physical Journal D*, vol. 57, pp. 303–320, 04 2010.

[17] S. Zimmer, *Search for a Permanent Electric Dipole Moment of* ^{129}*Xe with a He/Xe Clock-Comparison Experiment.* PhD thesis, Johannes Gutenberg Universität Mainz, 2018.

[18] “The NIST Reference on Constants, Units, and Uncertainty.” `https://physics.nist.gov/cgi-bin/cuu/Value?gammahpbar`. Accessed: 2024-10-28.

[19] W. Makulski, “Explorations of Magnetic Properties of Noble Gases: The Past, Present, and Future,” *Magnetochemistry*, vol. 6, no. 4, 2020.

[20] “The NIST Reference on Constants, Units, and Uncertainty.” `https://physics.nist.gov/cgi-bin/cuu/Value?gammappbar`. Accessed: 2024-10-28.

[21] F. Bloch, “Nuclear Induction,” *Phys. Rev.*, vol. 70, pp. 460–474, 10 1946.

[22] U. Schmidt, *Experimente mit polarisierten Neutronen zu Fragen der höchstauflösenden Spektrometrie und Quantenoptik.* PhD thesis, Technische Universität München, 1994.

[23] G. Cates, S. Schaefer, and W. Happer, “Relaxation of spins due to field inhomogeneities in gaseous samples at low magnetic fields and low pressures,” *Phys. Rev. A*, vol. 37, pp. 2877–2885, 04 1988.

[24] J. Schmiedeskamp *et al.*, “Paramagnetic relaxation of spin polarized He-3 at bare glass surfaces Part I,” *European Physical Journal D*, vol. 38, pp. 427–438, 06 2006.

[25] M. Repetto *et al.*, “Systematic T1 improvement for hyperpolarized ^{129}Xenon,” *Journal of Magnetic Resonance*, vol. 252, pp. 163–169, 2015.

[26] X. Zeng *et al.*, “Wall relaxation of spin polarized ^{129}Xe nuclei,” *Physics Letters A*, vol. 96, no. 4, pp. 191–194, 1983.

[27] A. Nicol, “Effect of several surface treatments on xenon nuclear polarization and relaxation in optically pumped Rb-Xe systems,” *Phys. Rev. B*, vol. 29, pp. 2397–2403, 03 1984.

[28] B. Driehuys, G. Cates, and W. Happer, “Surface Relaxation Mechanisms of Laser-Polarized ^{129}Xe,” *Phys. Rev. Lett.*, vol. 74, pp. 4943–4946, 06 1995.

[29] N. Newbury *et al.*, “Gaseous ^{3}He-^{3}He magnetic dipolar spin relaxation,” *Phys. Rev. A*, vol. 48, pp. 4411–4420, 12 1993.

[30] E. Hunt and H. Carr, “Nuclear Magnetic Resonance of Xe^{129} in Natural Xenon,” *Phys. Rev.*, vol. 130, pp. 2302–2305, 06 1963.

[31] B. Chann *et al.*, “^{129}Xe $-$ Xe Molecular Spin Relaxation,” *Phys. Rev. Lett.*, vol. 88, p. 113201, 02 2002.

[32] B. Anger *et al.*, “Gas-phase spin relaxation of ^{129}Xe,” *Phys. Rev. A*, vol. 78, p. 043406, 10 2008.

[33] B. Saam, W. Happer, and H. Middleton, “Nuclear relaxation of ^{3}He in the presence of O_2,” *Phys. Rev. A*, vol. 52, pp. 862–865, 07 1995.

[34] C. Jameson *et al.*, “Nuclear spin relaxation by intermolecular magnetic dipole coupling in the gas phase. ^{129}Xe in oxygen,” *The Journal of Chemical Physics*, vol. 89, pp. 4074–4081, 10 1988.

[35] R. Acosta *et al.*, “Diffusion in binary gas mixtures studied by NMR of hyperpolarized gases and molecular dynamic simulations,” *Physical Chemistry Chemical Physics*, vol. 8, pp. 4182–4188, 09 2006.

[36] M. Batz *et al.*, “Fundamentals of metastability exchange optical pumping in helium,” *Journal of Physics: Conference Series*, vol. 294, p. 012002, 06 2011.

[37] S. Appelt *et al.*, “Theory of spin-exchange optical pumping of ^{3}He and ^{129}Xe,” *Phys. Rev. A*, vol. 58, pp. 1412–1439, 08 1998.

[38] I. Ruset, *Hyperpolarized ^{129}Xe Production and Applications.* PhD thesis, University of New Hampshire, 2005.

[39] M. Wagshul and T. Chupp, “Laser optical pumping of high-density Rb in polarized ^{3}He targets,” *Phys. Rev. A*, vol. 49, pp. 3854–3869, 05 1994.

[40] M. Romalis, E. Miron, and G. Cates, “Pressure broadening of Rb D_1 and D_2 lines by ^{3}He, ^{4}He, N_2, and Xe: Line cores and near wings,” *Phys. Rev. A*, vol. 56, pp. 4569–4578, 12 1997.

[41] A. Burant, *Characterizing Hyperpolarized ^{129}Xe Depolarization Mechanisms during Continuous-Flow Spin Exchange Optical Pumping and as a Source of Image Contrast.* PhD thesis, University of North Carolina at Chapel Hill, 2018.

[42] T. Walker and W. Happer, “Spin-exchange optical pumping of noble-gas nuclei,” *Rev. Mod. Phys.*, vol. 69, pp. 629–642, 04 1997.

[43] I. Nelson and T. Walker, “Rb-Xe spin relaxation in dilute Xe mixtures,” *Phys. Rev. A*, vol. 65, p. 012712, 12 2001.

[44] G. Norquay *et al.*, “Optimized production of hyperpolarized ^{129}Xe at 2 bars for in vivo lung magnetic resonance imaging,” *Journal of Applied Physics*, vol. 113, p. 044908, 01 2013.

[45] M. Bouchiat, T. Carver, and C. Varnum, “Nuclear Polarization in He^{3} Gas Induced by Optical Pumping and Dipolar Exchange,” *Phys. Rev. Lett.*, vol. 5, pp. 373–375, 10 1960.

[46] E. Babcock *et al.*, “Limits to the Polarization for Spin-Exchange Optical Pumping of ^{3}He,” *Phys. Rev. Lett.*, vol. 96, p. 083003, 03 2006.

[47] C. Gemmel, *Test of Lorentz Symmetry with a ^{3}He/^{129}Xe Clock-Comparison Experiment.* PhD thesis, Johannes Gutenberg Universität Mainz, 2010.

[48] M. Wolf, *Erzeugung höchster ^{3}He-Kernspinpolarisation durch metastabiles optisches Pumpen.* PhD thesis, Johannes Gutenberg Universität Mainz, 2004.

[49] J. Jackson, *Classical Electrodynamics.* Wiley, New York, 1999.

[50] B. Josephson, "Possible new effects in superconductive tunnelling," *Physics Letters*, vol. 1, no. 7, pp. 251–253, 1962.

[51] J. Clarke and A. Braginski, *The SQUID Handbook: Fundamentals and Technology of SQUIDs and SQUID Systems.* Wiley, 2006.

[52] J. Clarke and A. Braginski, *The SQUID Handbook: Applications of SQUIDs and SQUID Systems.* Wiley, 2006.

[53] F. Allmendinger, *Precise Tests of Fundamental Symmetries at Low Energies using a ^{3}He-^{129}Xe Comagnetometer.* PhD thesis, Heidelberg University, 2015.

[54] F. Grüner, "Commissioning and calibration of a SQUID-System for the ^{3}He-^{129}Xe-Comagnetometer in Heidelberg," bachelor's thesis, Heidelberg University, 2023.

[55] F. Allmendinger *et al.*, "Degaussing Procedure and Performance Enhancement by Low-Frequency Shaking of a 3-Layer Magnetically Shielded Room," 07 2023.

[56] P. Le, "Measurement of the properties of Mu-metal in the magnetically shielded room at the Physikalisches Institut Heidelberg," bachelor's thesis, Heidelberg University, 2023.

[57] N. Holmes *et al.*, "A lightweight magnetically shielded room with active shielding," *Scientific Reports*, vol. 12, 08 2022.

[58] S. Celozzi *et al.*, *Electromagnetic Shielding: Theory and Applications.* Wiley, 2022.

[59] M. Caruso *et al.*, "A New Perspective on Magnetic Field Sensing," *Sensors (Peterborough, NH)*, vol. 15, 12 1998.

[60] F. Allmendinger. Private Communication.

[61] F. Thiel *et al.*, "Demagnetization of magnetically shielded rooms," *The Review of scientific instruments*, vol. 78, p. 035106, 04 2007.

[62] M. Repetto, *Improvements in production and storage of HP-^{129}Xe.* PhD thesis, University of Mainz, 2015.

[63] T. Hölzel. Private Communication.

[64] H. Müller, "The foundations of optics," *J. Opt. Soc. Amer. 38*, p. 661, 1948.

[65] S. Arnoldt, "Rotating Quarter-Wave Plate Stokes Polarimeter," bachelor's thesis, Bonn University, 2011.

[66] J. Zhen *et al.*, "A resistive Q-switch for low-field NMR systems," *Journal of Magnetic Resonance*, vol. 287, pp. 33–40, 2018.

[67] E. Baudin *et al.*, "An active feedback scheme for low field NMR experiments," *Journal of Physics: Conference Series*, vol. 294, p. 012009, 06 2011.

[68] P. Horowitz and W. Hill, *The Art of Electronics.* Cambridge University Press, 1999.

[69] C. LLC, "FAST DMOS FET Switches N-Channel Enhancement-Mode." `http://calogic.net/wp-content/uploads/2019/03/SST211_Datasheet_Rev_A.pdf`. Accessed: 2024-10-31.

[70] H. Raich and P. Blümler, "Design and construction of a dipolar Halbach array with a homogeneous field from identical bar magnets: NMR Mandhalas," *Concepts in Magnetic Resonance Part B: Magnetic Resonance Engineering*, vol. 23B, no. 1, pp. 16–25, 2004.

[71] A. Cherubinik and A. Bifone, "Hyperpolarised xenon in biology," *Progress in Nuclear Magnetic Resonance Spectroscopy*, vol. 42, no. 1, pp. 1–30, 2003.

[72] N. Kuzma *et al.*, "Fast Nuclear Spin Relaxation in Hyperpolarized Solid ^{129}Xe," *Phys. Rev. Lett.*, vol. 88, p. 147602, 03 2002.

[73] R. Fitzgerald *et al.*, "^{129}Xe spin relaxation in frozen xenon," *Phys. Rev. B*, vol. 59, pp. 8795–8811, 04 1999.

[74] W. Yen and R. Norberg, "Nuclear Magnetic Resonance of Xe^{129} in Solid and Liquid Xenon," *Phys. Rev.*, vol. 131, pp. 269–275, 07 1963.

[75] P. Granfors, A. Macrander, and R. Simmons, "Crystalline xenon: Lattice parameters, thermal expansion, thermal vacancies, and equation of state," *Phys. Rev. B*, vol. 24, pp. 4753–4763, 10 1981.

[76] M. Freeman, *The Efficiency Limits of Spin Exchange Optical Pumping Methods of ^{129}Xe Hyperpolarization: Implications for in vivo MRI Applications.* PhD thesis, Duke University, 2015. Retrieved from `https://hdl.handle.net/10161/9907` [Accessed: 9/24/2024].

[77] P. Blümler. Private Communication.

[78] J. Birchall *et al.*, "XeUS: A second-generation automated open-source batch-mode clinical-scale hyperpolarizer," *Journal of Magnetic Resonance*, vol. 319, p. 106813, 2020.

[79] A. Wojna-Pelczar and T. Pałasz, "A high volume, batch mode ^{129}Xe polarizer," *Nuclear Instruments and Methods in Physics Research Section A: Accelerators, Spectrometers, Detectors and Associated Equipment*, vol. 856, pp. 65–71, 2017.

[80] R. Brown *et al.*, *Magnetic Resonance Imaging: Physical Principles and Sequence Design: Second Edition.* 04 2014.

[81] J. Tremmel, "Commissioning of the magnetic coil system aiming towards long spin coherence times for a ^{3}He-^{129}Xe comagnetometer," master's thesis, Heidelberg University, Heidelberg, Germany, 2024.

[82] M. Repetto *et al.*, "HP-Xe to go: Storage and transportation of hyperpolarized ^{129}Xenon," *Journal of Magnetic Resonance*, vol. 265, pp. 197–199, 2016.

[83] F. Allmendinger *et al.*, “New Limit on Lorentz-Invariance- and CPT-Violating Neutron Spin Interactions Using a Free-Spin-Precession ^{3}He-^{129}Xe Comagnetometer,” *Phys. Rev. Lett.*, vol. 112, p. 110801, 03 2014.

[84] M. I. Products, “Improved, SPST/SPDT Analog Switches.” `https://www.analog.com/media/en/technical-documentation/data-sheets/DG417-DG419.pdf`. Accessed: 2024-10-31.

Acknowledgements

First of all, I want to express my deepest gratitude to **Prof. Dr. Ulrich Schmidt** who gave me this great opportunity to be part of this fantastic working group. Since my bachelor thesis, I have had the privilege of developing myself over the last five years, both academically and personally. His motivating way of tackling theoretical problems and his enthusiasm facing practical (especially electronics-related) challenges were an important prerequisite for the success of this work.

A special thank you goes to **Prof. Dr. Werner Heil** who gave me helpful advice in commissioning the xenon polarizer. I want to thank him for his patience with me while getting familiar with the basics of optical pumping and working with lasers.

I am also very grateful for the support of

- **Dr. Peter Blümler** for his tips on using and understanding the NMR spectrometer,

- **Dr. Fabian Allmendinger** for being my roommate who I could always turn to,

- our **bachelor and master students** who contributed to this thesis, especially **Toni Hölzel**, **Thang Le Pham Huy**, **Felix Grüner** and last but not least **Josef Tremmel**,

- the **mechanical workshop** who fulfilled all my wishes at the highest level.

- and the colleagues from the **secretary** who kept all the paperwork away from me.

Finally, I would like to thank **my parents, my brother and my sisters** for their love and constant support during the time of my studies.